ScuDo
Scuola di Dottorato ~ Doctoral School
WHAT YOU ARE, TAKES YOU FAR

Doctoral Dissertation
Doctoral Program in Electrical, Electronics and Communication Engineering
(33.rd cycle)

Robust Low-Cost Navigation Solutions for Service Robotics

Neil Gogoi

* * * * *

Supervisor
Prof. Fabio Dovis

Doctoral Examination Committee:
Dr. Marco Pini,*Referee*, LINKS Foundation
Dr. Calogero Cristodaro, *Referee*, Thales Alenia Space
Prof. Paolo Giaccone, *Committee President*, Politecnico di Torino
Prof. Marcello Chiaberge, Politecnico di Torino
Prof. Mauro Leonardi, University of Rome Tor Vergata

Politecnico di Torino
2022

I hereby declare that, the contents and organisation of this dissertation constitute my own original work and does not compromise in any way the rights of third parties, including those relating to the security of personal data.

. . . .

Neil Gogoi
Turin, 2022

Summary

Service robotics is becoming a reality in many aspects of daily life due to the successful merger of several enabling technologies from the fields of Information and Communication Technologies. The growing availability of mass market products is also driving innovation towards automation in several civil and scientific areas. The faster growth of the professional service robotics market the past half decade over industrial robotics is testament to the tremendous potential and impact envisioned of it in the upcoming years. To support such a new generation of service robots and vehicles, navigation capabilities play a fundamental role, whether be it in mission planning or on-field activities. Global Navigation Satellite Systems (GNSS) forms the navigational core in most outdoor applications and advancement in GNSS receivers in terms of complexity, processing capacity and cost adds to the capabilities of service robotics. However, development of GNSS algorithms in the context of Service Robotics specifically has been lacking, often solving problems through other sensors and technologies. GNSS positioning in harsh environments remain a challenge and the threat of RF GNSS interference has not been addressed in this field.

In this context, this thesis aims to maximise the input of GNSS technology in Service Robotics, developing robust and low cost GNSS receiver based solutions through available technological paradigms. Recent developments of ultra-low cost embedded GNSS smartphones provides this impetus to research into low cost navigation solutions. Modern smartphones also come with an advantage of having an ubiquitous network infrastructure with ease of developing interconnected applications and integrated proprioceptive and exteroceptive sensors, making it simpler to replicate automated unmanned ground vehicle and/or unmanned aerial vehicular networks of service robotics. Further, with the release of GNSS raw measurements in Android smartphones since Android 7, the opportunity of implementing collaborative solutions based on raw pseudorange processing for positioning and navigation is attractive in ready-to-network devices like smart-phones also considering the computational power of the current hardware setups.

The availability of GNSS raw measurements in Android smartphones allows in principle to improve the quality of GNSS-based positioning, by applying customized and advanced positioning algorithms. However, the quality of such measurements

is poor, mainly because of the low quality of smartphones hardware components and the non-ideal environment in which phones are typically used. To overcome this problem and to separate the contribution of the hardware components and signals quality, dedicated test campaigns were carried out in a real environment and in a controlled environment anechoic chamber using different Android models. In addition, signal processing techniques aimed at increasing accuracy and precision of the solution were employed.

Cooperation between GNSS receivers is first explored through relative positioning via an iterative Least Squares approach, in order to detect fast changes in position and velocity of a GNSS receiver. Displacements and deformation phenomena are analyzed considering a single difference approach also differenced in time. Exchange of raw GNSS measurements are also applied on Android smartphones to retrieve the relative range between two such phones based on a collaborative technique. Additionally, a framework for the exchange of data between smartphones is provided, allowing the application of such a computationally-efficient ranging methodology in a network of low cost GNSS mobile devices. This work is further extended into a low-cost navigation strategy for a UGV-UAV paradigm by including the relative range in position computation.

Any interference threat to a GNSS receiver could have cascading effects at application levels and for interconnected systems. As a vulnerability assessment, experimental interference tests are performed on the navigational units of commercial UAVs and Android smartphones. Comparisons are seen between the two different GNSS receiver grade based units and possible metrics are identified to build a defense to such interferences. Finally, the potential aid to such a defense through Cooperative Positioning (CP) techniques in connected GNSS receiver networks is discussed.

Acknowledgements

I would like to express my heartfelt gratitude to my supervisor and advisor, Prof. Fabio Dovis for his endless support during my PhD tenure. His passion towards scientific knowledge and research is truly inspiring, but his kindness and understanding are what pushed me through to finish this thesis. Thank you for believing in me, giving me the opportunities to succeed both professionally and personally. I thank PIC4SeR for giving me the opportunity to do this PhD and supporting my work throughout. Prof. Marcello Chiaberge has been always the guiding presence at all my activities at PIC4SeR and Gianluca Dara has been available for help any time I needed support. I would like to thank Caner and Wenjian for being the best possible peers I could hope for and we have shared many struggles and achievements together. Thank you Caner for also being one of the kindest person I have ever known. I would like to thank Alex Minetto for his utmost passion and dedication, not only in research but also in helping the people around him. I have gained massively through his guidance and advice. Nicola Linty was an inspiration to work with during my early years and seeing his endless knowledge and passion helped shaped my journey forward. I would also like the thank all the people at LINKS foundation for their knowledge and support any time I needed it during my PhD. I would like to thank my father, Pabitra for being an inspiration throughout my life and being the best father a son could hope for. I can never live up to your achievements as a person but I will try my best and I hope this work makes you proud. I thank my mother, Runumi for being the guiding hand throughout my life and making me laugh even through tough times. I thank my sister, Sukanya for being a wonderful human being. You've been my sparring partner in my life, helping me grow and always supported me no matter what. I thank my cousin, Shiladitya for being the big brother to me through my life. Last but not the least, I thank my friends for being the absolute positioning system in my life. Shaalivahan, Hiren, Shashwat and Ankit, you have helped me at a time where I thought I was beyond help.

Contents

List of Tables IX

List of Figures X

1 Introduction 1
- 1.1 Background 1
- 1.2 Objectives and contributions of the thesis 2
- 1.3 Outline of the thesis 4

2 Navigation in Service Robotics 7
- 2.1 Service Robotics Background 7
  - 2.1.1 Modern day Service Robotics 8
  - 2.1.2 Service Robots in Precision Agriculture 10
- 2.2 Navigation and in Service Robotics 11
  - 2.2.1 GNSS Based Localization 12
  - 2.2.2 Vision Based Localization 13
  - 2.2.3 Sensor Fused Localization 13
- 2.3 Towards Low Cost Navigation Solutions in Service Robotics 14

3 Global Navigation Satellite Systems 17
- 3.1 Introduction 17
- 3.2 GNSS Signals 19
- 3.3 GNSS Receiver Architecture 20
- 3.4 User Position Computation 22
- 3.5 Error Sources in GNSS Positioning 23
  - 3.5.1 Systemic Errors 23
  - 3.5.2 Atmospheric Errors 24
  - 3.5.3 Receiver Level Errors 24

4 Android Smartphones Based GNSS 25
- 4.1 Evolution of Positioning in Android Smartphones 25
- 4.2 Performance Analysis of Android GNSS Raw Data 27
  - 4.2.1 Real Environment Tests 27

4.2.2 Anechoic Chamber Environment Tests 33

5 Collaborative GNSS Methodology and Application 43
5.1 Fast Deformation Monitoring 43
5.2 GNSS Collaborative Ranging 44
5.2.1 Methodology 44
5.2.2 Experimental Setup and Results 48
5.3 Proof of Concept - Cooperative DGNSS 52
5.3.1 Proposed framework 52
5.3.2 Experimental setup and performance metrics 54
5.3.3 Results 57

6 Interference Threats to GNSS in Service Robotics 61
6.1 Overview and Assessment of Vulnerability 61
6.1.1 Experimental Setup 62
6.1.2 Analysis of the RFI Effects on the Navigation Performance . 65
6.2 Spoofing Effects on Raw GNSS measurements 70
6.2.1 Test Devices 70
6.2.2 Spoofing Scenario 71
6.2.3 Results and Analysis 74
6.3 Cooperative Positioning as an Interference Defence 77
6.3.1 Background and Scenarios 77
6.3.2 Experimental Tests 79
6.3.3 Results and Analysis 81
6.3.4 Analysis of Android Raw GNSS Measurements of the two devices 83

7 Conclusions 93
7.1 Scope of Future Activities 94

Bibliography 97

List of Tables

4.1 Statistics of the positioning solutions obtained from smartphones in a real environment. 31
4.2 Statistics of the positioning solutions obtained from smartphones inside the anechoic chamber. 38
4.3 Statistics of the smoothed positioning solutions obtained from smartphones inside the anechoic chamber, before and after the event. . . 40
5.1 Comparison of the quality of GNSS-based ranges 51
6.1 Devices under test. 71
6.2 Satellite Subsets 73

List of Figures

2.1 The technological stack of a modern service robot 9
2.2 Types of sensors in agricultural robots 10
2.3 A basic control diagram of an autonomous vehicle 12
3.1 GNSS segments. 18
3.2 Signal Generated from a GNSS Satellite. 20
3.3 Block diagram of a standard GNSS receiver 21
4.1 Set-up of the data campaign carried out using smartphones. The screw indicates the geo-referenced known point. 28
4.2 Comparison of the C/N_0 of three different satellites (low, medium and high-elevated PRNs), as estimated by the three different devices. 29
4.3 Comparison of the PVT (WLS), as estimated by the three different devices, in a real environment. The true reference position is shown on top, along with the average, the 1-σ and the 2-σ ellipses for all the three smartphones are shown on top. 30
4.4 Errors with respect to the reference position for all the three smartphones under test, in a real environment. 30
4.5 Example of 2nd order derivative of the raw and carrier-smoothed pseudorange measurements for a single GPS satellite and related positioning solutions. 32
4.6 Anechoic chamber setup: on the left side the receivers are shown, in face-up orientation; on the right side, the transmitting GNSS antenna is shown. 33
4.7 Record and Replay equipment and configuration for controlled experiments. 34
4.8 Simulated satellite constellations and related HDOP for record and replay experimental scenarios. 35
4.9 C/N_0 comparison between Android devices in a controlled environment. 36
4.10 Effect of cycle slips in a controlled environment (PRN 23). 37
4.11 Position comparison between devices, in a controlled environment. . 38
4.12 Position comparison between devices in a controlled environment. . 39

4.13 PRN 23 (closest) measurements in the controlled environment, highlighting the change around $t^* = 210$ s. 39
4.14 Clustering effect due to the presence of a low quality signal (PRN 15), in a controlled environment. 41
4.15 Comparison of the positioning results in the presence and in the absence of bad quality measurements. 42
5.1 Scheme of GNSS-based smartphone inter-agent ranging. 45
5.2 High-level packet format for the exchange of raw measurements for cooperative positioning applications. 45
5.3 Range bias compensation in DDR between two static receivers by means of raw Doppler measurements with simulated GNSS signals (no multipath, 6 GPS satellites). 49
5.4 20 m baseline test with DDR and PVT-R comparison. 50
5.5 20 m baseline test with DDR, DDR-W and PVT-R comparison. . . 50
5.6 DDR and DDR-W applied on smoothed pseudorange measurements, compared to PVT-R. 52
5.7 Range-based CP concept and pictorial scheme representing its implementation through Double Differences applied to GNSS pseudorange measurements to determine the inter-receiver distance and support DGNSS cooperative positioning and navigation. 53
5.8 High-level block scheme of the experimental setup. 53
5.9 GNSS fixes of UAV and UGV in follow-me configuration shown in Google Earth (5.9a) and in real scenario (5.9b). 55
5.10 Hardware setup for UAV and UGV during on-field experiments. . . 55
5.11 Barplots showing the reduction in the positioning error of the UGV provided by profitable Cooperative Positioning (CP) for each class of experiments, Follow-me mode (left), Independent hovering (center) and Partially-obstructed LoS(right). 58
5.12 Example of comparison of the CDFs computed through the post-processing of GNSS-only positioning solutions for UGV (5.12a) and UAV (5.12b) for the Follow-me mode. 59
6.1 Generic block diagram of interference test setup 63
6.2 Experimental setup in the anechoic chamber. 63
6.3 Parameters of the commercial receiver under jamming activities. . . 64
6.4 Estimated position of the commercial receiver as benchmark. 65
6.5 Estimated position by GPS unit from UAV 1 under jamming 66
6.6 Estimated position by IMU unit from UAV 1 under jamming 67
6.7 Estimated position by GPS unit from UAV 2, no data are avilable after 8th minute. 68
6.8 Estimated position by GPS unit from UAV 1 under spoofing 69
6.9 Estimated position by GPS unit from UAV 2 under spoofing. 69

6.10 Experimental setup consisting of a HackRF One, (1) equipped with an L1 stick antenna, (2), a Raspberry PI 4B, (3) a u-blox™ Neo-M8N GNSS, (4) with an active GNSS antenna, (5) and a set of smartphones, (6) listed in Table 6.1. 72
6.11 Sky-plot showing real and spoofed satellite signals. 73
6.12 Effect on real satellites (SV ID 24 and 25) during the test duration. 75
6.13 Effect of Spoofing on AGC. 75
6.14 Comparison of Fake (SV ID 16) and Real (SV ID 24) satellite's C/N_0 . 76
6.15 Common Satellite (SV ID 10) analysis. 76
6.16 Effect on Smartphone GNSS Position. 77
6.17 Schemes of possible attacks performed through a GNSS-based CP framework. Filled squares represent fake measurements provided by S while white squares are nominal measurements provided by A. . . 79
6.18 Effect of spoofing interference on u-blox™ Neo-M8N receiver. 82
6.19 Effect of spoofing on: a) Earth-Centered Earth-Fixed (ECEF) Z coordinate (left) and b) GNSS L1 satellite availability in Android smartphones (right). 83
6.20 Effect spoofing on Signal-to-noise ratios with (left) and without (right) spoofing during the test duration. 85
6.21 Effect spoofing on AGC with (left) and without (right) spoofing during the test duration. 85
6.22 AGC to C/N_0 ratio values with (left) and without (right) spoofing during the test. 86
6.23 Effect of different RFIs: a) jamming effect (left) and b) multipath (right) in Android smartphones. 87
6.24 Nominal cooperative PVT estimation 6.24a and the distortion effect of a *promiscuous cyber-attack* performed by inducing the overwriting the measurements of a generic aiding agent A, 6.24b 88
6.25 Meaconing detection By raw measurements 89
6.26 Time-limited meaconing attack to a cooperative network: effects of measurements inconsistency on the differential ranging. The upper plots show the behaviour expected in nominal conditions. 91

List of Acronyms

ADC	Analog-to-Digital Converter
ADR	Accumulated Delta Range
AGC	Automatic Gain Control
AI	Artificial Intelligence
AltBOC	Alternative Binary Offset Carrier
AWGN	Additive White Gaussian Noise
BOC	Binary Offset Carrier
BPSK	Binary Phase Shift Keying
C/A	Coarse/Acquisition
CAF	Cross Ambiguity Function
CAPS-Loc	Cooperative Android Positioning System for Localisation
CBOC	Composite Binary Offset Carrier
CDF	Cumulative Density Function
CDMA	Code Division Multiple Access
COTS	Commercial off-the-shelf
CP	Cooperative Positioning
C/N_0	Signal Carrier-to-Noise Density Power Ratio
DCM	Direction Cosine Matrix
DGNSS	Differential GNSS
EC	European Commission

ECEF	Earth Centered Earth Fixed
EKF	Extended Kalman Filter
ELE	Early-minus-Late Envelope
ELP	Early-minus-Late Power
ENU	East-North-Up
ESA	European Space Agency
FDMA	Frequency Division Multiple Access
FLL	Frequency Lock Loop
GEO	Geostationary Earth Orbit
GISM	Global Ionospheric Scintillation Model
GLONASS	GLObal NAvigation Satellite System
GNSS	Global Navigation Satellite System
GPP	General Purpose Processor
GPS	Global Positioning System
GSA	European GNSS Agency
H-WLS	Hybrid Weighted Least Square
HPF	High Pass Filter
ICD	Interface Control Document
IF	Intermediate Frequency
IGSO	Inclined Geo-Synchronous Orbits
IMU	Inertial Measurement Unit
IRI	International Reference Ionosphere
KF	Kalman Filter
LBS	Location Based Services
LLA	Latitude, Longitude, Altitude

LOS	Line-Of-Sight
LNA	Low Noise Amplifier
LO	Local Oscillator
LSSVM	Least Squares Support Vector Machines
MEO	Medium Earth Orbits
MLE	Maximum Likelihood Estimation
MMT	Multipath Mitigation Technology
MPS	Multiple Phase Screen
NCO	Numerically Controlled Oscillator
NED	North-East-Down
NIC	Network Interface Card
NLOS	Non-Line-Of-Sight
OS	Open Service
PCA	Principal Component Analysis
PDF	Probability Density Function
PE	Parabolic Equation
PLL	Phase Lock Loop
PoC	Proof Of Concept
PPP	Precise Point Positioning
PRN	Pseudo-Random Noise
PSD	Power Spectral Density
PSK	Phase Shift Keying
PVT	Position, Velocity and Time
QMBOC	Quadrature Multiplexed Binary Offset Carrier
QPSK	Quadrature Phase Shift Keying

RAIM	Receiver Autonomous Integrity Monitoring
RF	Radio Frequency
RFE	Radio Front-End
RFI	Radio-Frequency Interference
RMS	Root Mean Square
ROC	Receiver Operating Characteristics
RSS	Root Sum Squared
RTK	Real Time Kinematic
SBAS	Space Based Augmentation System
SDR	Software Defined Radio
SNR	Signal-to-Noise Ratio
SV	Satellite Vehicle
ToA	Time of Arrival
TOW	Time of Week
TTF	Time-to-First-Fix
UAV	Unmanned Aerial Vehicle
UGV	Unmanned Ground Vehicle
UERE	User Equivalent Range Error
USRP	Universal Software Radio Peripheral
UHF	Ultra High Frequency
UTC	Universal Time Coordinated
UTM	Universal Transverse Mercator
VHF	Very High Frequency
WLS	Weighted Least Squares

Chapter 1

Introduction

This Chapter provides a general background of the role of Global Navigation Satellite System (GNSS) in service robotics, its implementations and challenges. The objectives and contributions of the thesis is presented next and at the end, the outline of the thesis is presented.

1.1 Background

It is fair to say service robotics is a booming industry and it was predicted that in 2020 over half of the expected 1 million+ net robot sales will be from the service robotics industry. The market of service robots is also growing faster than that for industrial robots [1] and was expected to generate more than 16 billion US dollars in revenue in 2020. Next-generation robots, including collaborative and service robots, are projected to account for two-thirds of unit robot sales by 2025, up from 22 percent in 2015 [2]. The expected impact of robots on our future economies is staggering and experts at McKinsey Global Institute estimate that around half of today's work activities could be automated by 2055 [3]. Amongst it, the global precision farming market is expected to grow at a compound annual growth rate of 13.1 percent from 2021 to 2028 to reach USD 16.35 billion by 2028 [4], where robotics and automation play a vital role [5].

GNSS, being the modern absolute positioning system is a crucial component of agricultural service robots and nearly all robots designed for outdoor operations, except planetary rovers incorporate some sort of global navigation, and the trend has been moving upward since the cancelation of selective availability in 2000 [6]. The growing importance and interest in GNSS for agricultural applications has motivated the development of an ISO standard (ISO 12188-1:2010) provides a procedure for evaluating and reporting the accuracy of navigation data determined using positioning devices that are based on GPS, GLONASS, Galileo or similar global navigation satellite systems (GNSS) [7]. GNSS information although easy to access, however has limitations in agricultural environments with difficulties in guaranteeing long term robust and reliable measurements, especially for crucial dynamic states such as heading and speed. Therefore farm robots are endowed with multiple sensors and complicated architectures in such a way that the navigation algorithms embedded in the robot always make an optimized use of available data in real time.

1.2 Objectives and contributions of the thesis

The role of unmanned vehicles in precision agriculture has expanded manifold and is an active general field of research today [9, 10, 8]. Unmanned Ground Vehicles (UGVs) typically deal with cultivation tasks such as seeding, spraying, fertilizing, etc. [11], and Unmanned Aerial Vehicles (UAVs) take roles such as aerial mapping and crop monitoring [12]. Navigation and localization capabilities of such vehicles are vital to their operations and GNSS form the core of many navigation systems in outdoor agricultural activities. GNSS-based navigation in UGVs could be affected by bad satellites visibility [14, 13] and impaired signal reception, especially when they operate in harsh environments (i.e. foliage, ditches, etc.). These issues are generally mitigated exploiting multiple sensors integration strategies [15], robust GNSS receivers and external aiding [17, 16] at the price of steeper costs and complicated set-ups. In limiting conditions (urban canyons, foliage covers, forests) with low-cost devices, integrating Inertial Navigation Sensors (INS) with GNSS can be challenging due to incorrect modelling of the dynamics of the object itself [18, 19].

Hence targeting a low-cost navigation solution is challenging, yet vital to bringing down costs of UGV implementations in precision agriculture. The overbearing objective of the thesis has been to contribute towards this challenge utilizing recent technological advances in GNSS and communications. This has led the direction of the research towards Android™ smartphones since Android™ natively support both on-board ultra-low cost GNSS units and communication interfaces through specific Application Program Interfaces (APIs).

A blue print was provided in [20] for developing an Android™ smartphone based Auto-pilot and the differences between a traditional and smartphone based sensors at that time were laid out. In later research [21], an experimental Android™ smartphone based autopilot platform has been implemented by using smartphone sensors while achieving performances comparable to off-the-shelf autopilots. Some conclusions from their flight tests were landing positional errors being in tens of meters and the potential of using cellular communication to modernize the UAV landscape. The latter aspect is demonstrated in [22, 23, 24] showing efficient performance of modern cellular networks in UAV communication and control. Better positional performances are achieved in [25], however with GNSS-IMU integration.

In the last decades Collaborative Positioning (CP) has constituted a relevant topic in robotics, starting from a set of pioneering research works [27, 26] up to recent paradigms including GNSS, proprioceptive and exteroceptive sensors. The availability of a GNSS receiver, and of a communication subsystem makes smartphones suitable for research on the topic and consolidated methods based on exchange of GNSS measurements can be implemented. Further, newer devices allows to obtain higher quality measurements thanks to improving GNSS chipsets with support to dual frequency and multi-constellation GNSS signals, thus reducing the generic performance gap between high-grade commercial and mass-market receivers.

In the general scheme of a positioning unit which is typically interfaced to an application layer, the position information is exchanged to other services or stored in remote databases. Such an architecture is prone to a wide range of RF interference attacks, especially if it is based on products which are low cost, commercially available and off-the-shelf (COTS). Current GNSS signals used for mass-market applications (e.g. GPS L1 C/A, E1 Galileo and GLONASS) do not provide any means to ensure the authenticity of the transmitting source or to protect the receiver against possible spoofing attacks [29, 30, 28], using standard unencrypted communication services. In the near future, GPS Chips-Message Robust Authentication (Chimera) [31] and Galileo Open Service Navigation Message Authentication (OSNMA) [32] services will allows receivers to be resilient against counterfeit signals with both proposed to be fully operational by the end of 2022 [33, 32]. Chimera is a combination of Navigation Message Authentication (NMA) and spreading code encryption in the L1C GPS signal while the Galileo open service OSNMA consists only of the NMA digital signature of the navigation data. However it is still vital to examine the potential effects of intentional interference on the low-cost GNSS units embedded in mass market receivers as well as assessing the resilience of the receiver itself.

The main contributions of the thesis are summarized as follows:

- It provides the results of the first documented analysis of Android GNSS raw measurements under a completely controlled environment to separate the contribution of the hardware components and signals reception quality in Android smartphones.

- It presents a novel approach of use of GNSS receivers' master-rover relationship constraints to improve position and velocity solutions, through their baseline length and relative velocities computed directly through carrier phase measurements.

- It validates the use of raw GNSS measurements for collaborative relative ranging between GNSS receivers when compared to stand alone positioning based solutions. Successful data exchange of raw GNSS measurements is carried out through the IEEE802.11b Wi-Fi connection in Android smartphones. This paradigm is exploited to collaboratively improve the accuracy in the position estimation of a UGV in a UAV-UGV outdoor setup.

- The effects of anthropogenic disturbances on the GNSS units integrated in different grade drones and Android smartphones is analysed, specifically on positioning and raw measurements.

Some of the works presented in the thesis were published in peer-reviewed journal papers [36, 34, 35] and in different international conferences [38, 37, 39, 40]. Furthermore, the work done in Section 5.2 and Section 5.3 represents some of the fundamentals of the CAPS-Loc idea which won the Italy regional first prize in the 2019 GSA Galileo Masters Competition and was in the top 10 of global finalists.

1.3 Outline of the thesis

Chapter 2 introduces service robotics and outlines its importance to the modern world. With focus on outdoor unmanned vehicles, the navigational technologies widely used are explained. The current challenges to robust and low cost GNSS based navigation in UAVs and UGVs are explained thereafter. The approach taken in the thesis towards collaborative positioning solutions and the use of Android smartphones to represent COTS GNSS receivers is discussed.

Chapter 3 provides an overview of the fundamentals of GNSS with GNSS signals, GNSS receivers and the standard GNSS positioning algorithm explained in some detail. A brief overview of GNSS errors is provided at the end.

Chapter 4 provides the analysis of Android GNSS raw measurements through tests carried out in a real environment and in a controlled environment anechoic chamber using different Android models. In addition, signal processing techniques employed aiming at increasing accuracy and precision of positioning solutions are presented.

Chapter 5 details the different collaborative GNSS approaches explored to be applicable to a service robotics scenario with low cost GNSS receivers and the results are seen. Firstly, a fast deformation monitoring analysis through single differenced, time differenced GNSS raw measurements with low cost mass market receivers is presented. Secondly, the experimental validation of a collaborative relaitve ranging technique based on the exchange of raw GNSS measurements between Android smartphones is presented. The investigation of utilizing the relative ranging to the positioning solution of an UGV in a UAV-UGV cooperative paradigm is presented at the end.

Chapter 6 looks at the interference threats to GNSS in service robotics. The effects of anthropogenic disturbances, RF jamming and spoofing on the GNSS units integrated in different grade drones and smartphones is seen. Further, possible security threats to the proposed cooperative framework presented in this thesis is discussed along with an analysis on how cooperative positioning could help in the defense against RF attacks.

Chapter 7 provides the summary of the research work presented within this thesis and discusses some future works.

Chapter 2

Navigation in Service Robotics

This chapter first introduces the background and principles of service robotics, classifying the modern day service robots based on application and introduces the technologies in use. With regards to the work of this thesis, the role of service robotics in precision agriculture is explained. This leads to defining the navigation and localization technologies in precision agriculture service robotics. At the end, the approach taken in the thesis towards collaborative positioning solutions and the use of Android smartphones to represent COTS GNSS receivers is discussed.

2.1 Service Robotics Background

In the early days of robotics, the basic principle of automation was strictly applied to its use., i.e., the work processes were divided into individual action sequences in order to examine which of these sequences could be automated [41]. Mechanical repeatable tasks were performed by machines while non-automatable tasks were handled by humans, all towards reducing labour costs to increase industrial efficiency. Nowadays robots are widely seen as machines capable of carrying out a complex series of actions [42]. Due to technological advances in engineering and integration of robotics with the fields of artificial intelligence, cloud computing, big data, etc., a wide range of innovation in robotics implementation and application is being seen with the potential to change service industries being immense. As a consequence of machine intelligence and coherent interaction also between machines only, the possible application fields for robots continuously expand and increasingly leave well-defined and protected environments like factories [41]. New technologies and services, such as the Internet of Robotic Things [43] emerge as opportunities of complex merger of robots and autonomous systems with ubiquitous sensors. It can be foretold that in the future virtually all service robots will be connected and embedded into a bigger system (e.g. via knowledge bases and cloud-based systems)[44]. From a paradigm of cooperation between humans and machines, today robots take up of substitution, cooperation and also expansion of human skills. The role of robotics has moved even beyond the important economic cost–benefit analysis, for example with the comparison of skill of a robot to human while performing tasks such as deep sea ocean exploration, landing on Mars or reacting to disaster situations in complicated environments.

2.1.1 Modern day Service Robotics

With a basic examination based on the development activities across applications and industries, four broad categories can be assigned to modern service robots [45].

Professional Non-Social Service Robots

The services of these robots do not necessarily involve social interaction with employees and customers and their work could be in both indoor and outdoor environments. The specific environment and application defines their development and research direction. Examples can include from agricultural robots [46] and outdoor hazardous terrain climbing robots [47] to hospital service robots [48] and autonomous sewer robots [49].

Professional Social Service Robots

These service robots provide employees and customers with interactive situation-specific services and their roles are seen in use in business organisations or in public services. Social service robots require versatile and robust perception systems and solid interaction strategies [50]. Examples can include from a hotel bellboy service robot to a mobile guidance robot at an airport [51].

Domestic/Personal Non-Social Service Robots

Domestic/personal non-service robots are typically used for non-commercial services and are built to be highly autonomous in their predefined task area. Examples include outdoor lawn mowing robots[52] and indoor vacuum robots [53].

Domestic/Personal Social Service Robots

Interaction with humans is the key role of these robots and with the innovations in machine learning, deep learning, and artificial intelligence, service robots have become more social, intelligent, and adaptive. Examples include an elderly care and wellness robot [54] to a social companion robot [55].

As detailed in [56] and shown in Figure 2.1, service robotics today are a merger of various technologies. The technological stack of a modern service robot must

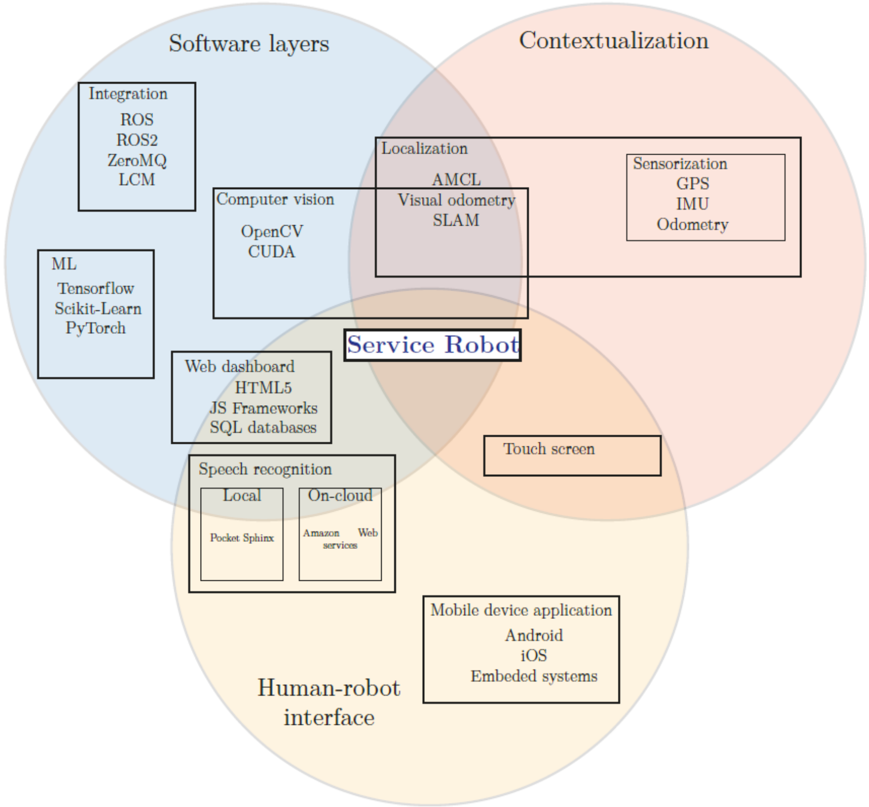

Figure 2.1: The technological stack of a modern service robot

address an uncontrolled environment and the complex integration of varied sensors should efficiently perform the expected robotic task. The three main technical groups to enable a service robot are software layers, contextualization and human-robot interfaces [56].

The software layers enable the connection, integration and synchronisation of the sensors within the robot while establishing a standard communication system for the components. Robot task planning and predefined and/or real time path planning is also a vital role of the software layer. Artifitial intelligence has always been important in service robotics dealing with specific aspects of their applications, such as analyzing images collected in agricultural settings, filtering operational data in manufacturing environments, or coordinating swarms of mobile robots in logistics. Contextualization includes the vital functions of localization and sensorization which allow the service robot to be aware of the spatial context of its environment and provide the tools to carry out its roles. Human-robot interfaces impelement the integration of the service robot to the human workflow. Web dashboards, touch screens, mobile device applications and speech recognition are the broad enablers of this.

Further reading on modern day service robots can be found at [57, 58, 59].

2.1.2 Service Robots in Precision Agriculture

The work of this thesis is funded by the PoliTO Interdepartmental Center for Service Robotics (PIC4SER) who aims to coordinate the activities of several research groups on the enabling technologies necessary for the development of the highly innovative and multi-disciplinary area of service robots. As detailed in Section 1.2 focus of the work was put on precision agriculture service robotics, targetting low cost and robust navigation solutions. Precision agriculture, emerging in the 1980s, is a kind of management system that combines multiple technologies, including sensors, computer information technology, mechanical technique, etc [60]. Its development has been driven by the desire to better handle the spatial and temporal variability, e.g. in soil water-content or crop varieties, from farm-scale, down to field-scale, through to sub-field scale [61].

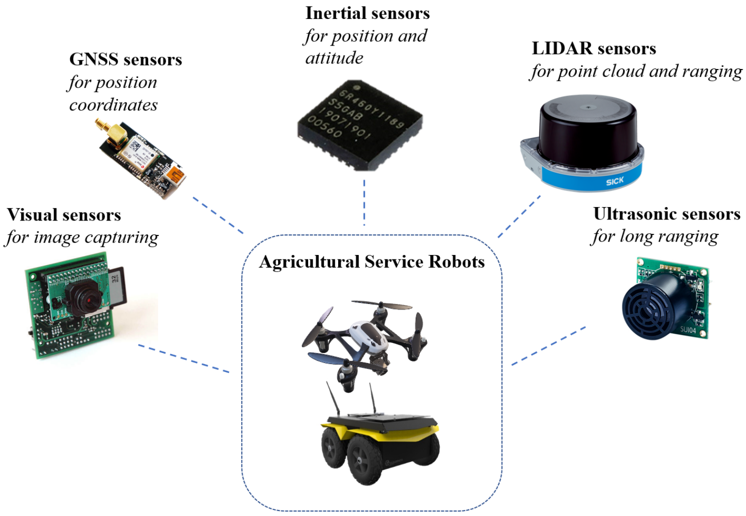

Figure 2.2: Types of sensors in agricultural robots

The introduction of agricultural robots gave a significant boost to the process of precision agriculture through automation. Robotic technologies potentially can also increase the window of opportunity for intervention, for example, being able to travel on wet soils, work at night, etc. Sensory data collected by robotic platforms in the field can further provide a wealth of information about soil, seeds, livestock, crops, costs, farm equipment and the use of water and fertiliser whereas Low-cost Internet of Things (IoT) technologies and advanced analytics are already beginning to help farmers analyze data on weather, temperature, moisture, prices, etc [62]. These service robots include both UAV and UGVs can carry out a variety of tasks such as seeding, spraying, fertilizing, etc., to help producers manage the farmland better and improve the yield. The sensors deployed on these agricultural robots are the essential components for them to implement their functions and the constellation of sensors can be broadly listed as in Figure 2.2 and detailed in [63].

With the development and integration of these multiple sensors, these service robots can accomplish greater outputs and efficiency through precision, cooperation and enhancement of human capabilities in the agricultural sector. A lot of these robots are however still not intelligent enough and remain prototypes without much commercialization [63] due to reasons such as deficiencies in integration algorithms and processors, adaptation to complex environments and operating power capabilities. Therefore research into development of better sensors and streamlined algorithms is essential to realise the potential of agricultural robots in complex agricultural environments.

[64] reviews most of the recent research and development in agricultural field robotics.

2.2 Navigation and in Service Robotics

The concept of fully autonomous agricultural vehicles is far from new and examples of early 'driverless tractor' prototypes using leader cable guidance systems date back to the 1950s and 1960s [63, 65]. However autonomous navigation in an agricultural environment is a difficult task due to the inherent uncertainty in the environment where shapes, sizes and colors of plants, light intensity and overall surroundings vary [66]. Hence different auto navigation systems for agricultural machinery have been invented and evaluated in the past decades and [67] provides a brief overview of research efforts over the past 50 years directed toward the development of guidance systems for agricultural vehicles. A modern day autonomous agricultural robot utilizes sensors to collect its ambient information as well as the state of the vehicle. This helps the robot inticipate its next variable state and steering angle which is controlled by dedicated algorithms. The process is detailed in [68] and can be summarized in a basic control diagram of autonomous vehicle as shown in Figure 2.3. The list is not exhaustive and only the most popular sensors, algorithms and steering controllers are mentioned. Detailed descriptions and pros and cons of all of them the are beyond the scope of this thesis and can be found in [68, 67, 69].

For any modern outdoor navigation system, localization is essential. Mission and path planning along with navigation control and guidance of a service robot follows a localized system of a service robot and its environment. The modern localization methodologies can be categorized into GNSS based localization, Vision based localization and Sensor fused localization.

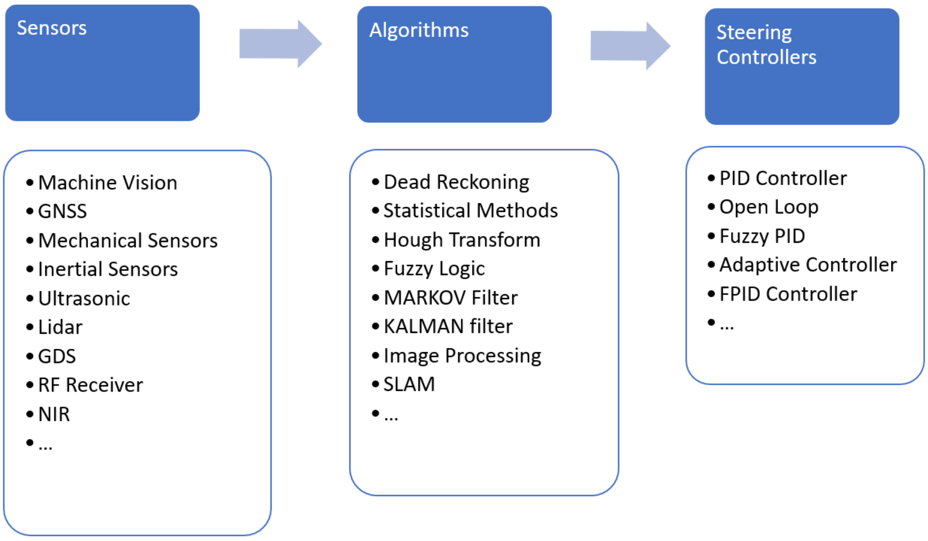

Figure 2.3: A basic control diagram of an autonomous vehicle

2.2.1 GNSS Based Localization

GNSS receivers have been used as global localization and guidance sensors since the early 1990s due to them providing an absolute position based guidance system compared to relative guidance of other sensors. The desired application accuracy of localization in agriculture ranges from 12-40 cm for tillage to 2-4 cm for planting [70]. For path guidance within agricultural fields, the required accuracies could range from 10-20 cm to a meter depending on the agricultural environment. A standard stand-alone GNSS receiver is of course not capable of providing such accuracies and instead many different correction services are available such as free differential satellite corrections, commercial satellite differential corrections forming Precise Point Positioning (PPP) services and Real Time Kinematic (RTK) corrections, either virtually or with a base GNSS station within 10 kms. Multiple studies and analysis conclude that Real Time Kinematics (RTK) clearly provides the best accuracy performance in agricultural environments, if cost constraints of devices are not considered [71, 6]. With an experimental testbed and methodology for assessing RTK GNSS receivers in precision agricultre environments, [72] concluded that RTK GNSS can match target performance requirements and, in turn, be used for machinery guidance and automatic field operations, only with reliable wireless channels and mobile network coverage. Further GNSS modernization has been targeted during the last decade with the addition of new navigation signals (L2C, L5 and L1C) to respective GNSS satellite constellations. Further oher GNSS systems have borne fruition with China's BEIDOU being operational and Europe's GALILEO almost reaching full operational capability. This will enable faster signal acquisition, enhanced reliability, greater operating range, and better signal reception in challenging environments.With such improved accuracy and enhanced reliability, GNSS will be the first choice of localization sensor for agricultural vehicle navigation in the future as well [70].

Chapter 3 is dedicated to describe GNSS technology in further detail.

2.2.2 Vision Based Localization

GNSS alone is insufficient in agricultural applications where a robotic vehicle has to follow crop lines or rows with accuracy of centimeters. For this robotic vehicles have vision based systems, either or both of monocular and stereo based, to enable it to find relative positions between the vehicle and the rows. Localization with a monocular vision systems involves the steps of image acquisiton, image calibration, image segmentation, row detection and finally calculation of navigational errors [70]. With the advancement of computing and processing technology, vehicle localization and guidance using stereo vision systems have become possible with affordable hardware and its main advantage over monocular vision remains in its capability of range detection in addition to the color/feature detection [70]. Stereo vision based vehicle guidance has been an active topic of research and [73] reported a stereo vision-based crop row detection system to automatically navigate a tractor in a soybean field with a lateral deviation of less than 5 cm at the speeds up to 3.0 m/s. The vision system can provide very rich information, including color, shape, and depth of objects (rows), which can be easily integrated onto a vehicle due to the small footprint. [74] aimed to verify the closeness of agreement between manual and stereo-image measurements, and thus to provide helpful information regarding safety and working purposes. With the addition of advanced vision systems, including depth perception, scanning sensors such as LiDAR and artificial intelligence for decision making and classification, the concept of precision can be potentially taken to another level [62]. A vision based system could also be an alternative localization sensor for agricultural vehicle guidance when GNSS signals are unavailable.

2.2.3 Sensor Fused Localization

As listed in Figure 2.2, there are generally multiple sensors playing a role in the overall navigation guidance system of agricultural robots. Each type of sensor has limitations in agricultural environments. GNSS receivers are most susceptible to harsh environment conditions such as tree canopy, buildings, etc. A vision based guidance system suffers when there is illumination variance or a cluttered background in agricultural fields. Most tactile and laser sensors work in only predefined limited operations and inertial sensors have time accumulated error problems. Therefore a multi-modal systems on a robot based on a combination of GPS, INS, LiDAR, vision, etc has the best potential to provide robust and accurate solutions with requiring external in-field infrastructure. A simple sensor fusion strategy would be to select only the best sensor at a time based on the ambient conditions of the robot. However most research based and commercial modern day navigation system designs fuse the output of each sensor to achieve robustness, reliability and higher positioning velocity and accelaration update rates. However developing fusing algorithms are challenging due to sensors being in different coordinate systems, time synchronizations and weight estimates of each sensor output. Traditionally this is tackled using the Kalman filter algorithm [75] and its derivatives such as the extended Kalman filter and unscented Kalman filter. Adaptive and optimization-based approaches are used to overcome problems of fine tuning the Kalman filter parameters and it is still an active field of research.

2.3 Towards Low Cost Navigation Solutions in Service Robotics

GNSS, being an absolute positioning method form the core of most navigation systems in outdoor agricultural activities and is one of two positioning methods along with dead reckoning sensors based relative positioning. As mentioned before, the focus of the work on this thesis has been to achieve low cost and robust navigation solutions for precision agriculture. Multiple navigation sensors integration strategies [15] and robust GNSS receivers and external aidings [17] of course come at the price of steeper costs and high-complexity set-ups. Lowering costs and higher performance of COTS GNSS receivers along with the constant modernization of GNSS signals leads the work to exploiting already existing set-ups in agricultural robotics to improve GNSS positioning solutions. For example, agricultural UAVs are assumed to self-locate with a decimeter-level precision to guarantee reliable in-flight operational capabilities. Thanks to the in-flight stability they can also provide reliable relative positioning of objects included within the field of view of the on-board vision system (i.e. digital camera) thus turning in a promising external positioning sensor for ground vehicles [16].

Heading towards low cost navigation solutions lead to exploring a GNSS Collaborative Positioning (CP) approach in this thesis work exploiting standard UAV-UGV paradigms in agricultural robotics with active communication networks. Advances in communication networks will allow the integration of relative measurements among connected GNSS receivers which can enable the receivers to either improve on or even determine their own location through this collaboration. In fact, most of the early contributions addressed CP to provide positioning and navigation in GNSS-denied environment and they were mostly focused on sensor networks [76]. [77, 78] were some of the first contributions to CP strategies in the field or robotics and later CP methodologies to solve for localization of multiple robotic vehicles were introduced [80, 79]. A novel approach to range only localization has been also proposed in [81] where terrestrial range measurements retrieved from occasional anchors allow to approximate the position estimate. The arguement of superiority of collaborative methodologies over differential GPS techniques have been presented in literature [83, 82] and thus the fusion of differential GNSS measurements and collaborative navigation techniques could be explored for future generation of GNSS receivers.

In parallel, the availability of ultra-low cost embedded Global Navigation Satellite System (GNSS) has enabled several affordable Location Based Services (LBS). New chipsets supporting dual frequency and multi-constellation GNSS signals are reducing the gap between high grade and mass market GNSS device performances. Among these devices, Android smartphones represent valuable and affordable tools for many LBS in the early advent of Intelligent Transportation Systems and smart vehicular navigation. Mobile networks natively provide a multiplicity of connected devices, thus enabling a family of applications demanding for a communication channel among GNSS receivers and in the case of this thesis, CP based approaches. A remarkable amount of works in literature is present about range-based collaborative methods for positioning and navigation in robotics [26] and more recently such interesting approaches have been considered within a GNSS-only framework suitable for low-cost hardware [84]. Successful implementation of such with the ultra-low cost GNSS chipsets of Android smartphones are going to open a plethora of applications. For example, the impact of relative positioning on pedestrian navigation or the use of raw measurements for basic proximity indication of users among LBS. The shift in improvement of quality and features (multi-frequency, multi-constellation) of smartphone modules could extend similar applications to drones and service robotics as well.

The performance of GNSS receivers on Android smartphones is provided in Section 4 and the CP approaches applicable to agricultural service robotics carried out in this work is detailed in Section 5.

Chapter 3

Global Navigation Satellite Systems

This chapter provides an overview of the fundamentals of GNSS with GNSS signals, GNSS receivers and the standard GNSS positioning algorithm explained in some detail. A brief overview of GNSS errors is provided at the end.

3.1 Introduction

The Global Navigation satellite system (GNSS) was born out of the growing need to determine accurate positions for military applications during the Cold War between the United States of America (USA) and the former Soviet Union (USSR). They had already basic forms of regional satellite navigation systems in the form of 'TRANSIT' and 'Cicada' for the USA and USSR respectively, both following the concept of Doppler based positioning. Along with evolving technology and need for a positioning system with a global coverage, both nations started conceptualizing and developing the Global Positioning System (GPS) (USA) and the Globalnaya Navigatsionnaya Sputnikovaya Sistema (GLONASS) (USSR) simultaneously during the 1970s, achieving full operational capability by the mid-nineties. Although the main application was to be towards the military, it soon found application in the civilian domain with separate civilian use signals being added to the systems eventually. The range of civilian application of the satellite navigation signals increased manifold and there are many different domains dependent on them today ranging from atmospheric monitoring to banking and finance.

Other navigation systems existing today include Satellite Laser Ranging (SLR), Lunar Laser Ranging (LLR), Precise Range and Range Rate Equipment (PRARE), Doppler Orbitography and Radio Positioning Integrated by Satellite (DORIS) and different Space Based Augmentation systems (SBAS). Among the many advantages of using GNSS are it being an accurate, all-weather, all time (continuous), multi-purpose real time system with its 3-dimensional coordinates being consistent throughout the globe. This allows GNSS to transcend all other positioning sensors with most systems like Radars, Radar Becons, AIS (marine), Inertial systems, Barometers, Gyroscopes, etc., being used to augment or supplement GNSS positioning today.

Any GNSS system generally consists of three basic segments: Space Segment, User Segment and Control Segment as shown in Figure 3.1.

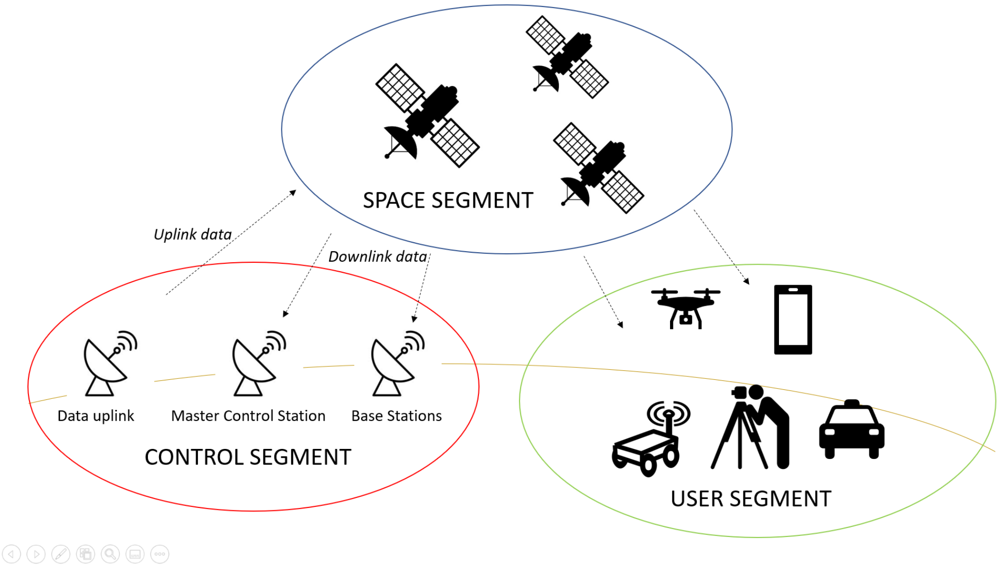

Figure 3.1: GNSS segments.

The Space segment consists of basically the satellite constellation. A nominal constellation is made of 24 satellites which can provide global coverage with 4-10 satellites visible at any given point on the earth. The orbits are typically circular at altitudes between 19,000-23,600 km from the earth. A constellation could consist of 3-6 planes typically with 55-65 degrees of orbital inclination. The satellites have radio transmitters, atomic clocks, computers and other additional equipment on board.

The Control segment consist of the ground control centre, monitoring stations and uplink stations. Its main objectives are to maintain each satellite in its orbit, make corrections and adjustments to the satellite clocks and track the satellites to generate the navigation data for each satellite. The control centre basically controls the system collecting tracking data from the monitoring stations, calculating the satellite orbital and clock parameters and passing on this data to the uplink stations to be uplinked to the satellites.

The User Segment basically consists of military and civilian users with a various range of receivers including standard code pseudorange receivers, code/carrier receivers, precise code receivers, multi-frequency receivers and multi-constellation multi-frequency receivers.

GPS, GLONASS, Galileo and BEIDOU (COMPASS) are the global GNSS constellations. The Japanese QZSS and Indian IRNSS (NAVIC) are the regional constellations with special orbits different from global constellations. The former is expected to be fully operational by 2023 while IRNSS completed its satellite constellation on April 12th, 2018. They provide full positioning coverage in specific regions while also acting as a supplement to the global constellations. The Space Based Augmentation Systems (SBAS) - WAAS, MSAS, EGNOS, GAGAN, SDCM, BDSBAS and KASS act only to augment the performance of the global and regional constellations providing updated corrections, integrity and higher performance to its users.

The following sections give a brief overview on the workings architecture of GNSS signals, receivers and processeses towards position computation. Further detailed explanation into the fundamentals of GNSS is covered in several books such as [88, 86, 85, 87, 89].

3.2 GNSS Signals

The propagation of GNSS signals through space relies on electromagnetic waves and their transmission from GNSS satellites towards the earth occurs in the L frequency band. A standard GNSS signal is a Right-Hand Circularly Polarized (RHCP) wave which will contain a carrier frequency, a ranging code to determine the time of flight from the satellite to the receiver and the navigation data which provides information on the satellite ephemeris, satellite clock parameters, almanac (coarse information of satellites in the constellation) and other complementary information such as satellite health status. The basic block diagram of signal generation in a GNSS satellite is shown in Figure 3.2.

Atomic clocks on board the GNSS satellites provide a consistent time reference for the RF carrier and codes genarated. An unique PRN ranging code sequence is generated in each satellite which acts as the spreading code for the binary-coded (0 and 1) navigation data modulated according to a defined digital modulation scheme. For example, a Binary Phase Shift Keying (BPSK) modulation [88] scheme is applied in most of the existing GNSS signals to combine the code and navigation data. A BPSK modulated signal can be written as:

$$s_{\mathrm{BPSK}}(t) = \sqrt{2P}\, s(t)\, \cos\left(2\pi f_0 t + \phi\right) \tag{3.1}$$

where P is the transmitted signal power, f_0 is the carrier frequency, ϕ is the carrier phase, and $s(t)$ is the bipolar (i.e. $+1$, -1) representation of modulo-2 addition of the spreading code and navigation data [90]. The carrier phase (ϕ) is either 0° or

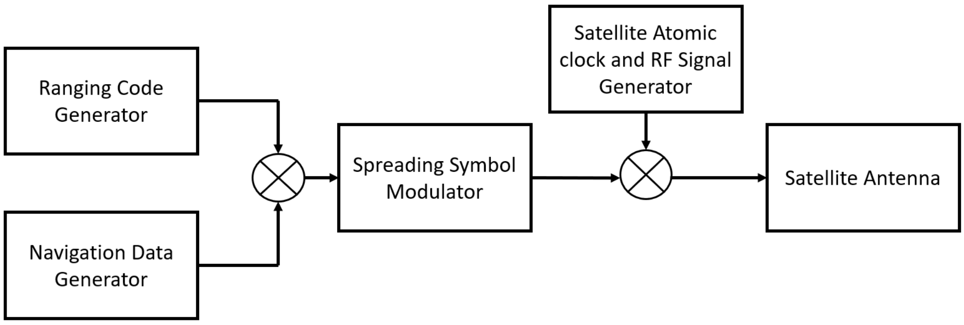
Ranging Code Generator
Navigation Data Generator
Spreading Symbol Modulator
Satellite Atomic clock and RF Signal Generator
Satellite Antenna

Figure 3.2: Signal Generated from a GNSS Satellite.

180° depending on transmitted digital 0 and 1 over successive bit intervals of the navigation message.

With modern day multiple multi-frequency constellations, different GNSS signals employ different Direct Sequence Spread Spectrum (DSSS) modulation [86]. It should be noted that the use of unique satellite PRN ranging codes by constellations with the same carrier frequency is known as Code Division Multiple Access (CDMA). Only GLONASS differs from CDMA by using the same ranging codes, but transmitting in multiple frequencies within the L1 and L2 bands and this is known as Frequency Division Multiple Access (FDMA). Towards modernization of GLONASS, some CDMA signals have been added as well recently.

3.3 GNSS Receiver Architecture

The GNSS receiver process the satellite signals and provides the user with an estimated PVT solution. There are various processing blocks in a GNSS receiver, the front of which is generally hardware based and then software signal processing based to compute the PVT solution. Figure 3.3 is a generic block diagram of a GNSS receiver showing the processes the satellite signal passes through to procure the final PVT solution.

The front end block receives the signal from the GNSS antenna and the signal goes through amplifiers, filters, down conversion to an intermediate or baseband frequency and sampling. In a GNSS receiver, the RF front end stage determines the cost, size and power consumption of the receiver and its design has the primary importance [91]. The Low Noise Amplifier (LNA) along with bandpass filters play a key role in supressing strong spectral noise and amplifying the weak GNSS signals. A local oscillator is present at the front end and used for the down-conversion of

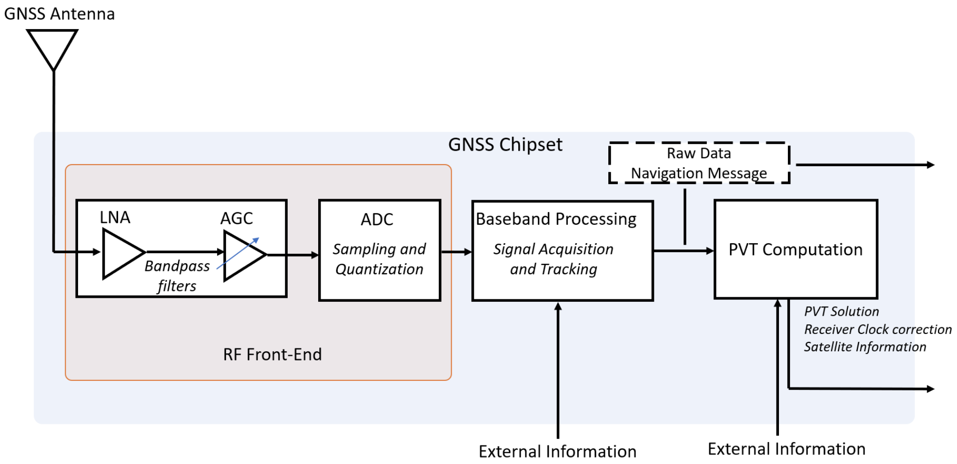

Figure 3.3: Block diagram of a standard GNSS receiver

the signals. The Analog to Digital Converter (ADC) sits at the end of the front end to procure IF digital samples. The Automatic Gain Control (AGC) stage is closely related to the down-conversion and quantization steps, and is responsible for adjusting the gain of the front end section in order to take benefit from the full dynamic range [92].

The role of the acquisition stage is to find out all the visible satellites in the incoming digitized signal samples from the front end. A rough estimate of the doppler frequency and code phase values are also fed from the acquisition to the tracking stage. This is achieved by rough synchronization of locally generated replica signals with the incoming signal by the use of correllators and the Cross Ambiguity Function (CAF) analysis technique [93]. After the coarse estimate of initial code delay and carrier Doppler by the acquisition block, the signal tracking is performed to obtain fine estimates of signalparameters of interest. A number of traditional signal tracking loop architectures such as phase-locked-loop (PLL) for carrier-phase tracking, frequency-lockedloop (FLL) for carrier Doppler frequency shift tracking, and delay-locked-loop (DLL) for code delay tracking are widely used as engineering standards in modern digital GNSS receivers [93]. In deeply coupled GNSS-sensor(like INS) integrations, information from the sensors are fed into this stage to help in achieving faster tracking times.

Outputs of the Baseband Processing stage include the demodulated navigation message of the incoming signal(s) and raw data such as carrier phase measurements, code pseudoranges and doppler values. This is fed into PVT computation algorithms and are also transmitted or stored for other applications. The PVT computation benefits from augmentation data (e.g. EGNOS, PPP) or INSs, improving the accuracy and availability in harsh environments [94].

3.4 User Position Computation

Ignoring systematic errors, GNSS pseudorange 3.2 and carrier phase 3.3 equations for a generic user u and a generic satellite j at time t are as follows:

$$P_u^j = \rho_u^j - c\delta t^j + c\delta t_u + T_u^j + I_u^j + E_u^j \tag{3.2}$$

$$\lambda\varphi_u^j = \rho_u^j + \lambda N_u^j - c\delta t^j + c\delta t_u + T_u^j - I_u^j + E_u^j \tag{3.3}$$

Where,

$$\rho^j{}_u = \sqrt{(x^j - x_u)^2 + (y^j - y_u)^2 + (z^j - z_u)^2} \tag{3.4}$$

represents the geometric range between receiver-satellite considering Earth-Centered Earth-Fixed (ECEF) positions (m) and (c) is the speed of light (m/s); (δt^j) is the satellite clock error (s); (δt_u) is the receiver clock error (s); (T_u^j, I_u^j, E_u^j) are the tropospheric and ionospheric error and ephemeris biases respectively; λ is the wavelength of the incoming signal; and (N) is the number of full wave cycles received at receiver, commonly defined as integer phase ambiguity.

Typically, a single difference approach consists of two different receivers (installed in two different points) that see one common satellite: in this case, differencing their code or carrier phase observations it is possible to remove the satellite clock bias (Blewitt, 1997). The atmospheric and ephemeris biases are also reduced or eliminated for short baselines less than around 20km (Blewitt, 1997). In such case, the single-difference pseudorange (3.5) and carrier phase (3.6) equations for two receivers m and r and a satellite j neglecting systematic errors would be:

$$P_{mr}^j(t) = \rho_m^j(t) - \rho_r^j(t) - c\Delta t_{mr} \tag{3.5}$$

$$\lambda\varphi_{mr}^j(t) = \rho_{mr}^j(t) + \lambda N_{mr}^j - c\Delta t_{mr}(t) \tag{3.6}$$

where $N^j{}_{mr}$ is the integer ambiguity difference between receiver m and r from satellite j. $\Delta t_{mr} = \delta t_m - \delta t_r$ is the relative clock bias between the two receivers.

The most widely used algorithm for position computation is non-linear least squares (LS) method. The non-linear system of equations requires an iterative procedure in order to provide a feasible solution. 3.2 is the basic observation equation for the pseudorange P_u^j, and the non-linear term represents the geometric range between satellite j and user u. From the linearization of 3.4 it is possible to derive the generic linear system for least squares or Kalman approach:

$$y = Ax + b \tag{3.7}$$

Where y represents the observables vector, A is the design matrix, x the vector of unknowns and b the known vector.

Considering a generic number n of satellites, the design matrix $A1$ and the known vector $B1$ can be expressed as follows:

$$A1 = \begin{bmatrix} \frac{x^1 - x_r}{\rho_r^1} & \frac{y^1 - y_r}{\rho_r^1} & \frac{z^1 - z_r}{\rho_r^1} & 1 \\ \frac{x^2 - x_r}{\rho_r^2} & \frac{y^2 - y_r}{\rho_r^2} & \frac{z^2 - z_r}{\rho_r^2} & 1 \\ \dots & \vdots & \vdots & \vdots \\ \frac{x^n - x_r}{\rho_r^n} & \frac{y^n - y_r}{\rho_r^n} & \frac{z^n - z_r}{\rho_r^n} & 1 \end{bmatrix} \tag{3.8}$$

$$B1 = \begin{bmatrix} b^1 & b^2 & \cdots & b^n \end{bmatrix}^T \tag{3.9}$$

Where, for differential pseudorange positioning

$$b^j = P_m^j - P_r^j + \rho_m^j - \rho_r^j - c\delta t_m \tag{3.10}$$

P_m^j and ρ_m^j are the pseudorange and geometric range from satellite j to the master m respectively. P_r^j and ρ_r^j are the pseudorange and geometric range from satellite j to the linearization point of the rover receiver r.

The receiver coordinates are updated at every iteration till the threshold of normally either 1 mm difference or 30 iterations. A converging solution requires less than 10 iterations to attain such precision [95].

3.5 Error Sources in GNSS Positioning

Errors in GNSS position estimation could arrive from a multitude of sources. They can be generally categorized into three categories.

3.5.1 Systemic Errors

These are the errors arrising from system or at the space control level. Some common systemic error sources are.

Dilution of Precision Errors(DOP)

DOP or Geometric DOP is the general term to describe the geometry of total satellites visible to a GNSS receiver on earth. Hence DOP errors arrise from 'poor' relative positions in the three-dimensional space of satellites with respect to the GNSS receiver. If the satellites are cluttered in a narrow angle of vision to the receiver, the uncertainty regions of range of each satellite will coincide with each other much more than if the satellites are spread across the sky in a broader azimuth and elevation sense. Therefore the quality of precision of measurements is greatly affected by poor values.

Satellite Ephemeris and Clock Errors

Small (upto 1-2 meters) errors may arrise occasionally due to older satellite ephemeris data but for satellite ephemeris and clock errors to affect a GNSS receiver greatly, there has to be a systematic failure in one or multiple satellites of a constellation. This phenomenon may be rare but there had been an incident as recent as 2019 to the Galileo constellation due to ephemeris update problems.

3.5.2 Atmospheric Errors

Although there are sufficient models to compensate for Ionospheric and Tropospheric models, the Ionosphere could constitute one of the biggest sources of errors to single frequency receivers during Ionospheric Scintillation events which cannot be predicted. In general errors caused by the troposphere is smaller than the ionospheric error, but cannot completely be eliminated by calculation.

3.5.3 Receiver Level Errors

This category forms the most prevalent source of errors in modern day GNSS receivers, as it could either be both intentional or unintentional. The various hardware components and circuits in a GNSS receiver contribute to receiver noise and though generally they are standardized, it could be a significant error source in low quality low cost COTS GNSS receivers, as seen in smartphones in [36]. GNSS signal power quality also contributes to loss of accuracy and precision in GNSS solutions and it is categorized by low Signal to Noise Ratio (SNR) and/or Carrier to Noise Ratio (C/N_0). The most prevalent sources of receiver level errors are however due to harsh or unsuitable environments which enable high multipath conditions of loss of satellite visibility. One of the most dangerous receiver level errors however is interference to GNSS signals which if intentional could lead to dire consiquences in critical applications. Section 6 provides a broader overview on the threat of GNSS interference.

Chapter 4

Android Smartphones Based GNSS

In this chapter a detailed analysis of the performance of GNSS receivers on Android smartphones is provided. The evolution of positioning in smartphones is described and the performances of different smartphones are seen, both in a real environment and in an anechoic chamber environment. Analysis of the results of Android GNSS raw measurements under a completely controlled environment as carried out within the anechoic chamber, had not documented before. Comparisons of position measurements between the anechoic chamber and a real environment reveal the nuances behind the large errors seen in GNSS-only Android positioning solutions. Understanding and mitigating them is vital toward the push to achieve higher performance through such devices. Through the work towards the analysis of android raw measurements several value additions have been made to the open source Google Matlab toolbox [96] including multi-constellation, multi-frequency implementation, navigation data demodulation, smoothing and filtering algorithms.

4.1 Evolution of Positioning in Android Smartphones

To support and encourage the rapid innovation trend in GNSS, in 2016 Google made available raw GNSS measurements retrieved from the enabled GNSS chipset for mobile devices. The measurements can be retrieved from the on-board GNSS chipset through Android Application Programming Interface (API) 24 on devices running Android 7+ equipped with enabled chips, thus boosting the improvement of their positioning and navigation performance. Starting from the availability of raw code pseudoranges and Doppler measurements, developers implemented a bunch of precise positioning algorithms based on such consumer grade GNSS receivers [97, 98]. Among these implementations, for instance, Doppler filtering and augmentation have been investigated in [99] to reach sub-meter accuracy. By exploiting carrier-phase observations on the enabled models, it is also possible to smooth code-based pseudorange measurements and reach decimeter-level accuracy without phase ambiguity resolution, as successfully proposed in [100]. The recent push to achieve precise positioning from Android smartphones thanks to the availability of their raw measurements has been also boosted by the release of a white paper from the European GNSS Agency (GSA) [94]. This allows for a clearer reference of the hardware performances of the devices helping in a more effective integration with other sensors and analysis of multiple GNSS constellations among many other applications. The aforementioned effective examples of improved positioning and navigation capabilities suggest valuable implementations of affordable smartphones GNSS hardware in different contexts.

Signal impairments such as multipath, have been seen as the major deterrent in achieving accurate positioning affecting the Carrier to Noise Power Density Ratio (C/N_0) up to 10 dB in certain Android devices, largely extending ambiguity resolution time periods and causing cycle slips [101]. The problem of cycle slips however, is mostly attributed to the presence of a power saving function known as *duty cycling*, a mode in which the GNSS chip is active only for a fraction of each second [102]. While code measurements are unaffected by interrupted signal tracking, the continuity of phase measurements is not achieved, resulting in cycle slips, which make any carrier-phase based processing unusable [103]. Duty cycle implementation is different in each Android phone and not explicitly declared by the manufacturer, which makes it difficult to distinguish from bad measurements. The option of switching duty cycle off has been implemented in latest Android releases (P), but wasn't available at the time of conducting this work.

To quantify the effects caused by signal impairments in a real environment, it is important to first determine the results of an ideal condition. In this work, differently from previous performance assessments [104], the performances of positioning algorithms based on raw GNSS measurements is investigated in a controlled environment: an anechoic chamber. The study allowed to determine the quality of the measurements without the presence of multipath and external spurious signals. The test were performed by means of record and replay technique [105] applied to simulated GNSS signals by means of an IFEN™NavX hardware signal generator and constellation simulator. Positioning solutions were evaluated with different carrier-smoothing algorithms to reach high precision and verify the performance of the navigation solutions obtained.

4.2 Performance Analysis of Android GNSS Raw Data

Following the release of raw GNSS measurements in Android smartphones, it became possible to directly compute pseudoranges and in turn to solve the trilateration problem employing advanced and customized techniques [94]. Raw GNSS data can be obtained from any supported phone through the GnssLogger App released by Google, or similar apps available. Subsequently, raw data can be post-processed by implementing a custom software or through the official Google tool. In this work, the GnssLogger App and the Google 'gps-measurement-tools-master' MATLAB open source Toolbox, both available from Android Developers website [106] have been used. The post-processing tool has been forked and upgraded to account for ionospheric and tropospheric delay corrections and to compute carrier smoothed solutions.

4.2.1 Real Environment Tests

The raw GNSS data used in this section were collected during a dedicated campaign at Politecnico di Torino premises, on October 19, 2018. 10 minutes of raw GNSS data were stored using the GnssLogger App. L1 C/A signals from GPS constellation were considered. Three different devices have been used:

- Xiaomi MI 8 (single frequency mode) running Android 8, later on denoted **MI 8**
- Samsung Galaxy S8 (Exynos 8895) running Android 8, later on denoted **S8**
- Huawei P10 running Android 8, later on denoted **P10**

The position of the phones and of the geo-referenced point are shown in the picture of Figure 4.1. The geo-referenced point is used as reference position for the computation of the error. It has to be noted that although being a roof-top location, an incomplete open-sky view is available, due to some higher buildings in the near surrounding. Some known sky obstructions, as well as some multipath reflections are expected to affect the quality of the data collected.

The GNSS signal strength is commonly evaluated through the C/N_0, defined as the ratio between the carrier power (C) and the noise power density (N_0) [85]. The C/N_0 is a good indicator of the quality of the signal and of the hardware components of the receiver, such as the antenna [107]. The C/N_0 of three GPS satellites, common to all the three devices, was observed: Pseudo Random Noise (PRN) number 18 with the highest elevation (67°), PRN number 20 with the lowest elevation (4°) and PRN number 14 at a medium elevation (31°). Figure 4.2 displays the comparison between the C/N_0 as measured from the three different devices.

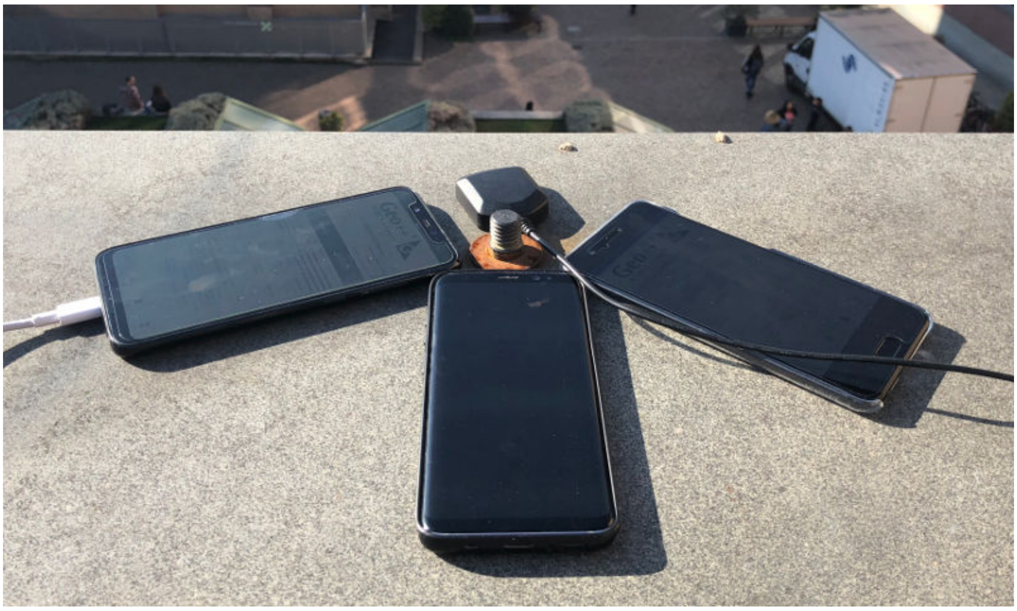

Figure 4.1: Set-up of the data campaign carried out using smartphones. The screw indicates the geo-referenced known point.

The quality of S8 and MI 8 devices is comparable, at least for the closer satellites, while the P10 device performs worse in all cases. In the case of PRN 18, the three measurements differ by almost 5 dB. Furthermore, the S8 shows a more stable C/N_0 estimate. The MI 8 on the contrary has the highest sensitivity, being able to gather measurements from a weaker signal, i.e. the farthest satellite, with more continuity and stability.

The comparison can be made also in terms of positioning solution errors. The position solutions obtained running the Google Toolbox [96] are considered after the addition of atmospheric corrections to the toolbox by the authors. For this the Klobuchar ionospheric model using broadcast ephemeris and the Hopfield troposphere model have been implemented. For a fair comparison, a common subset of satellites has been selected for all the smartphones, including GPS signals with PRN 1, 10, 11, 14, 18, 22, 27, 32. Even though the data collection was performed simultaneously and at the same location, it is not possible to ensure that all satellites are always in tracking state for all the smartphones and thus to guarantee perfectly equal conditions. However, the appearance and disappearance of some of them is something to be expected considering the different hardware and is indeed very representative of a realistic situation. For the sake of fairness, all signals which are in tracking state for at least one epoch in all smartphones are considered. Furthermore, PRN 20 was excluded from the analysis given its very low quality, also shown in Figure 4.2. Excluding a few outliers, the Horizontal Dilution Of Precision

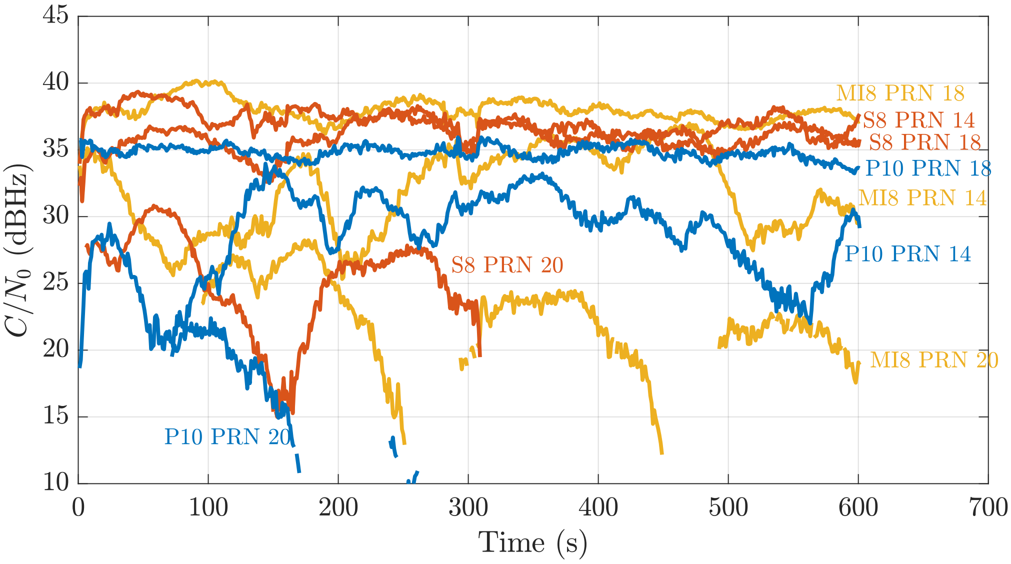

Figure 4.2: Comparison of the C/N_0 of three different satellites (low, medium and high-elevated PRNs), as estimated by the three different devices.

(HDOP) always ranges between the excellent values of 1.1 and 1.3 for all smartphones, with a common slight increasing trend. The impact of the HDOP can then be considered negligible.

Figure 4.3 compares the horizontal positioning solutions of the three devices and of the reference control point obtained by means of iterative Weighted Least Squares (WLS) approach. The triangle indicates the average position of the three different models, while the colored points represent all the position solutions along the 10-minutes test. The covariance ellipses are also depicted by considering the 1-σ and 2-σ confidence interval of the horizontal joint distribution of the positioning solutions. It can be clearly seen that the Xiaomi MI 8 device outperforms the others, both in terms of accuracy and precision, by almost one order of magnitude. This is clearer in Figure 4.4, which shows the differences of the North and East coordinates of the devices from the true coordinates. Mi 8 measurements are at the same time more stable and more accurate, while P10 and S8 measurements lead to errors up to tens of meters. A significant bias in the North direction is clearly visible on P10 and S8 devices.

Table 4.1 reports summary data which show the Huawei P10 having the worst performance while the Samsung S8 seems to be slightly better. The MI8 outperforms all the others devices, confirming that the quality of recent GNSS chipsets is higher and in general improving with time. The vertical positioning performance is poorer compared to the horizontal performance in all the devices. Indeed, the algorithms used to remove the atmospheric biases are based on empirical models, able to remove in average the 50% of the delay and thus a residual uncompensated

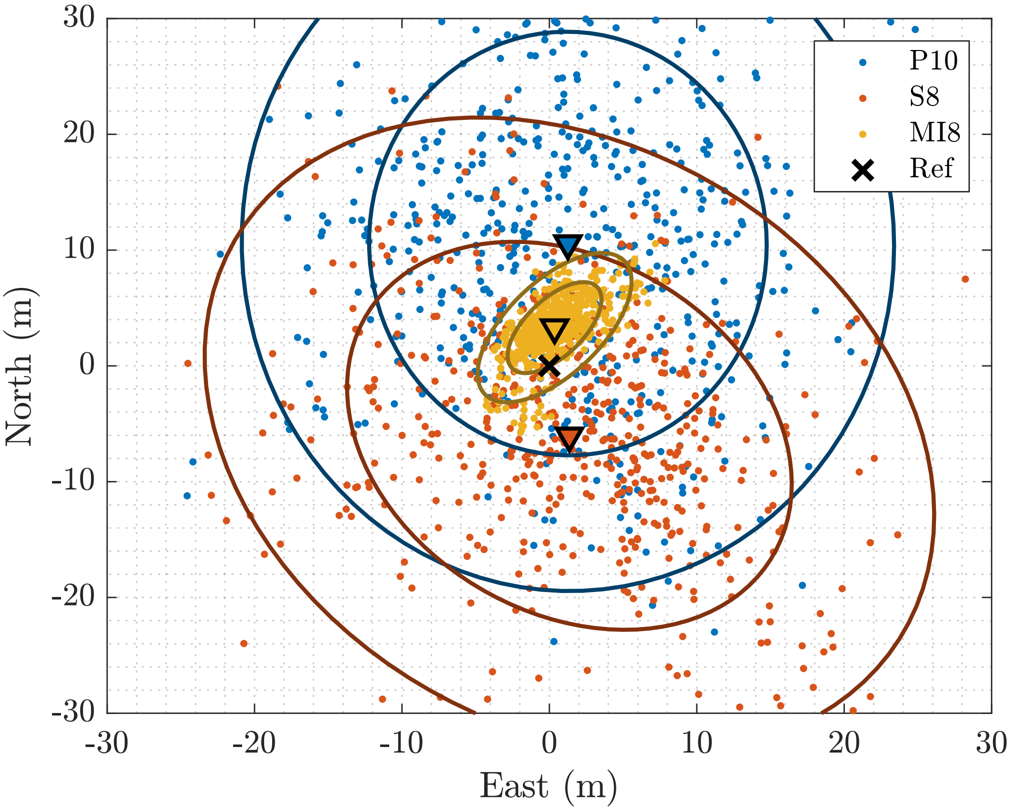

Figure 4.3: Comparison of the PVT (WLS), as estimated by the three different devices, in a real environment. The true reference position is shown on top, along with the average, the 1-σ and the 2-σ ellipses for all the three smartphones are shown on top.

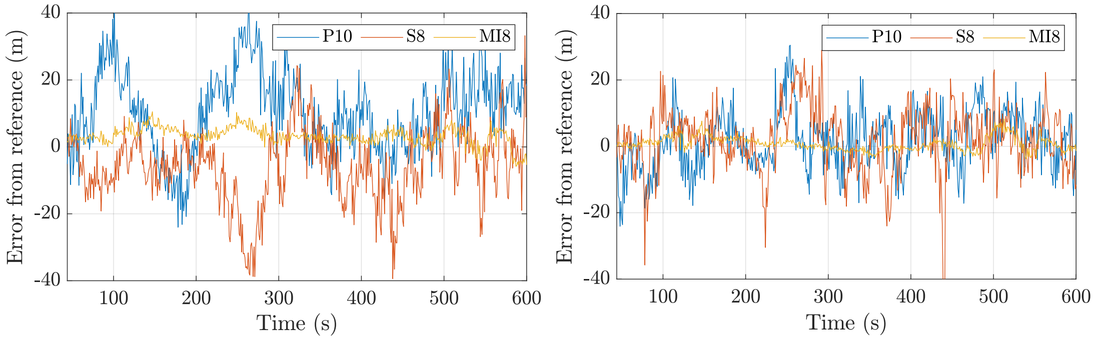

(a) North direction

(b) East direction

Figure 4.4: Errors with respect to the reference position for all the three smartphones under test, in a real environment.

delay might affect the results.

Table 4.1: Statistics of the positioning solutions obtained from smartphones in a real environment.

Device	CEP (m)	Horizontal RMSE (m)	North (m) $\mu \pm \sigma$	East (m) $\mu \pm \sigma$	Height (m) $\mu \pm \sigma$
Huawei P10	15.1	10.6	10.4 ± 12.1	1.7 ± 8.9	-10.0 ± 37.1
Samsung S8	11.4	6.2	-6.0 ± 11.1	1.8 ± 9.6	-8.1 ± 33.1
Xiaomi MI 8	3.8	3.3	3.2 ± 2.6	0.8 ± 2.1	0.0 ± 7.5

The limitations of GNSS code pseudoranges are evident in the results. To draw interesting conclusions it is then necessary to improve the quality of code measurements. On one side, the large noise of code measurements is a limit to high accuracy LBSs in smartphones, in some cases also preventing the possibility to benchmark the real capabilities of smartphones chipsets. A possible solution is given by signal processing techniques based on measurements smoothing, as described in Section 4.2.1.

Furthermore, for professional receivers, open-sky environment is a good scenario, while for mass-market devices, typically equipped with low quality antennas and oscillators, it might still represent a challenging environment. This motivates the need to perform measurements in a controlled environment such as an anechoic chamber.

Smoothing of Code Pseudoranges

Code measurements are unambiguous but noisy; on the contrary, carrier phase measurements are much more precise, but inherently ambiguous and the process to solve for the integer ambiguity is non affordable by mass-market receivers [85]. An intermediate solution is based on the combination of code and carrier phase measurements through a process denoted carrier smoothing filtering [109, 108]. The basic code and carrier phase pseudoranges have already been defined in equations 3.2 and carrier phase 3.3. For the purposes of this section, let $\rho(t)$ and $\Theta(t)$ be the code and carrier pseudorange respectively. The smoothed pseudorange, at epoch t_n can then be defined by the following finite difference equation:

$$\bar{\rho}(t_n) = \frac{1}{L}\rho(t_n) + \frac{L-1}{L}\left[\bar{\rho}(t_{n-1}) + \Theta(t_n) - \Theta(t_{n-1})\right] \tag{4.1}$$

where L is a weight coefficient and $\Theta(t_n) - \Theta(t_{n-1})$, called the *delta pseudorange* added, is obtained by differencing subsequent epochs. As long as no carrier cycle slips occur, the integer ambiguity term is constant and disappears thanks to the difference operation.

While the noise term of the code measurement $\rho(t_n)$ is at meter-level, the noise term of the carrier phase measurement $\Theta(t_n)$ is at centimeter-level. Furthermore, if the two measurement epochs are close enough to each other, in the order of a few seconds, the ionospheric delay term can be considered constant and thus disappears in the delta pseudorange. The parameter L controls the weight of the code and carrier contributions. A higher L assures a lower noise variance, but introduces a bias in the smoothed code pseudorange due to the different sign of the ionospheric delay in code and phase measurements, known as code-carrier divergence. Carrier smoothing is indeed a valuable technique to improve the accuracy of the positioning solution in smartphones, which cannot employ pure carrier phase measurements.

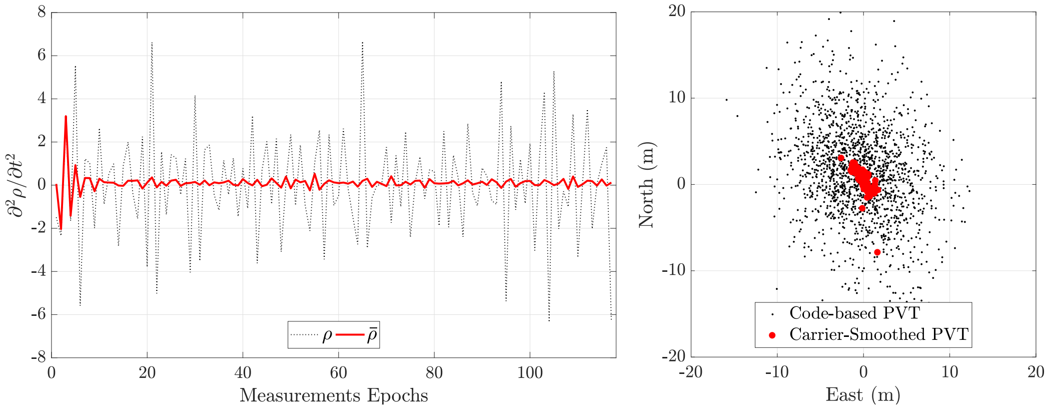

Figure 4.5: Example of 2nd order derivative of the raw and carrier-smoothed pseudorange measurements for a single GPS satellite and related positioning solutions.

Figure 4.5 reports a comparison of raw pseudorange measurements and the correspondent smoothed version. The related positioning solution is obtained over 30 min of data. The error with respect to the true position, in East-North coordinates, is plotted on the right. The positioning obtained by exploiting code-based measurements is compared to the solution obtained exploiting carrier smoothing. The smoothing weight L was set to 100. The accuracy of the results improves by about one order of magnitude when smoothing is enabled. However, the carrier-smoothing measurements are valid as long as the phase measurements are stable and not affected by carrier cycle slips. Impairments on the signal carrier phase can cause cycle slips, errors of one full cycle made by the receiver tracking loop in estimating the phase of the signal. Cycle slip, although being irrelevant for code-based measurements and for the purpose of estimating the carrier Doppler frequency, lead to errors in phase-based and carrier smoothed measurements, and consequently to a degraded positioning performance.

4.2.2 Anechoic Chamber Environment Tests

An anechoic chamber is a testing facility designed to completely absorb Radio Frequency (RF) waves, thanks to the particular shape and material of the walls. Therefore, it can be used to simulate ideal propagation condition. Being isolated from the surroundings, the chamber also reduces the impact of external RF impairments. In addition, the signals transmitted inside are not propagated through the walls, thus avoiding any jamming or spoofing situation while re-playing a GNSS signal. The anechoic chamber of the Department of Electronics and Telecommunications (DET) of Politecnico di Torino has been used for the test. Different Android devices and the GNSS antenna transmitting simulated GNSS signals are clearly visible in the left pictures reported in Figure 4.6.

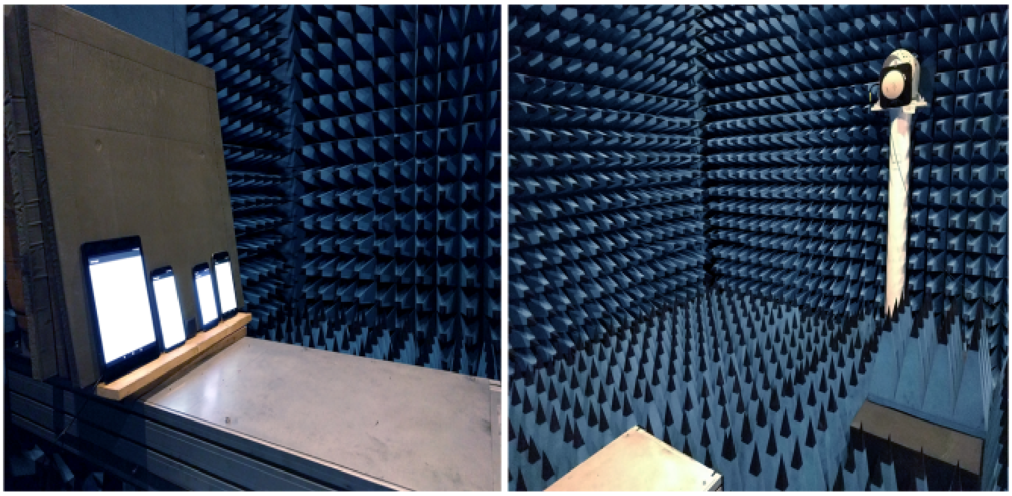

Figure 4.6: Anechoic chamber setup: on the left side the receivers are shown, in face-up orientation; on the right side, the transmitting GNSS antenna is shown.

The transmission and reception of GNSS signals was pursued according to the *Record and Replay* paradigm [105]. A block scheme of the set-up is shown in Figure 4.7. The original transmitted GNSS signals was obtained in a controlled setup as well, exploiting an IFEN™NavX professional constellation and hardware signal generator, simulating a static position according to a set of given coordinates. L1 C/A signals from all the visible satellites belonging to GPS constellation were simulated at RF and then digitized by means of a front-end, connected to the simulator through a wired link. No receiving antenna was used for the record step, thus avoiding multipath effects due to RF propagation. Signals were recorded as digitalized raw samples by means of Ettus Research™Universal Software Radio Peripheral (USRP) N210 front-end, equipped with a RFX OS364-13 Oven Controlled Crystal Oscillator (OCXO). The signal acquisition was performed at 5 Msps, at Intermediate Frequency (IF), and at 8 bit/sample for In-phase and Quadrature components to guarantee an adequate replication of the stream. Binary files were hence stored on an external memory, and then replayed through a second USRP used in transmitting mode, directly in the anechoic chamber. The system was equipped with a Rubidium atomic clock, to provide a precise timing for the digital to analog conversion of the samples. Analog signals emitted by the USRP were amplified by a Low Noise Amplifier (LNA) to feed a passive Novatel hemispherical antenna, installed in the anechoic chamber for the transmitting test. The devices were located on a support aligned to the main axis of the nominal pattern of the transmitting antenna inside the anechoic chamber. The patch was connected to a u-Blox EVK-M8QCAM benchmark receiver, used to verify the adequacy of power calibration of the transmitting front-end and the actual visibility of the simulated signals (Figure 4.8).

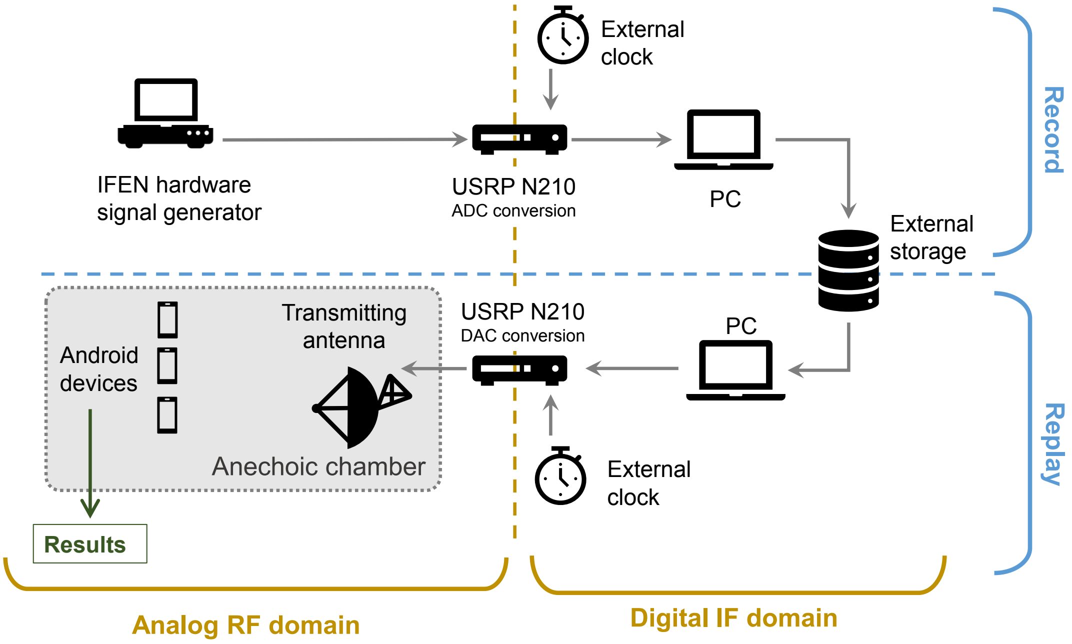

Figure 4.7: Record and Replay equipment and configuration for controlled experiments.

Controlled tests of 10 minute intervals were carried out in the anechoic chamber using the following devices:

- Huawei P10 smartphone
- Huawei P10 Plus smartphone
- HTC Nexus 9 tablet

Raw GNSS data were collected by means of the Google GnssLogger App and post-processed using the Google Toolbox.

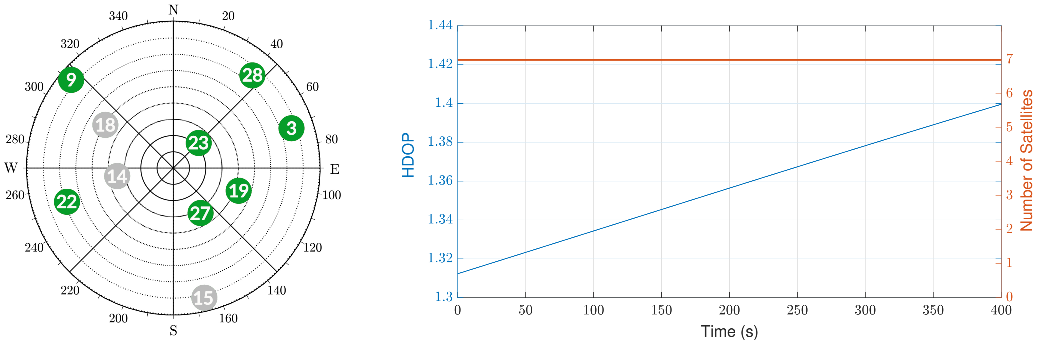

(a) Skyplot of simulated satellites

(b) Number of visible satellites and HDOP

Figure 4.8: Simulated satellite constellations and related HDOP for record and replay experimental scenarios.

Analysis of raw measurements

The satellites visibility in all the devices was comparable and raw measurements of 7 GPS L1 signals which were visible throughout the observation period were processed. As an example Figure 4.9 plots the C/N_0 values of GPS PRN 3 for all the Android devices under test. A similar trend is seen that for all the other visible PRNs. The C/N_0 of both Huawei models is more stable, with standard deviations (STDs) of around 0.08 dB, with respect to the Nexus 9, with around 0.14 dB STD. Nevertheless, the values are 3 dB lower than the latter. Interestingly, the Nexus 9 C/N_0 values are also a close match to the reference benchmark receiver. The cause of slight spike in C/N_0 value around 320 seconds in the Huawei devices could not be determined and could be due to a manufacturer setting.

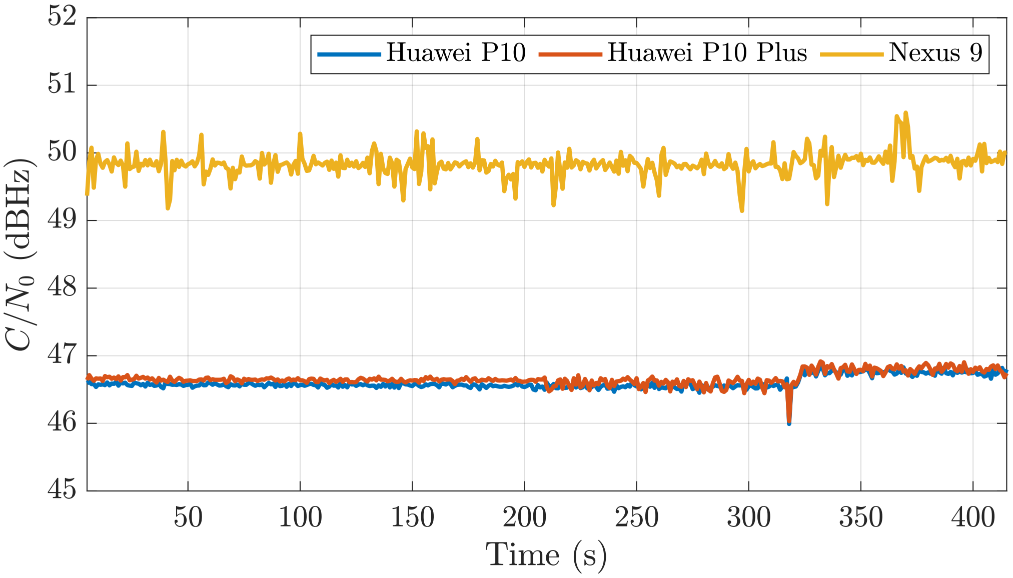

Figure 4.9: C/N_0 comparison between Android devices in a controlled environment.

It was seen that on the Huawei models, after $t^* = 210$ seconds of the start of logging, the raw measurements deteriorates considerably. The STDs of the C/N_0 before and after this were around 0.04 dB and 0.09 dB respectively. This deterioration causes a significant difference in measurements. On observing no change in the `HardwareClockDiscontinuityCount` parameter (which gives the count of the receiver clock discontinuities [94]) of the Google Toolbox output during the entire observation period, it can be assumed that even though the primary TCXO clock is running, the GNSS tracking chipset is turned off.

Figure 4.10 plots the detrended code pseudorange deviation (lower panel) compared with the `AccumulatedDeltaRangeState` parameter for GPS PRN 23 (upper panel). Such a flag indicates whether the range measurements is reset or there is a cycle slip due to a loss of lock [94]. The quality between the code and carrier pseudoranges is compared by calculating their de-trended STDs. For short time spans, de-trended pseudorange measurements can be considered as an ergodic process and are obtained through second order differentiation [101]. From the figure, it is seen that there is a failure to achieve ambiguity fix in the Huawei models after t^*, but there are no cycle slips before this mark. The pseudorange noise remains within 2 meters for all the PRNs before duty cycle occurs. In the Nexus 9, there are no cycle slips during the 10 minute interval tested and the noise remains within 4 meters. This was observed in all the other available PRNs. The continuity of high variability detrended pseudorange is due to the switching of clocks when duty cycle occurs [94]. The de-trended code and carrier phase pseudorange STDs of the Huawei devices before the power saving function are within 3 meters and 12 millimeters respectively whereas for the Nexus 9 it is within 6 meters and 13 millimeters. In comparison, the de-trended benchmark receiver code pseudorange STDs are within 1.5 meters.

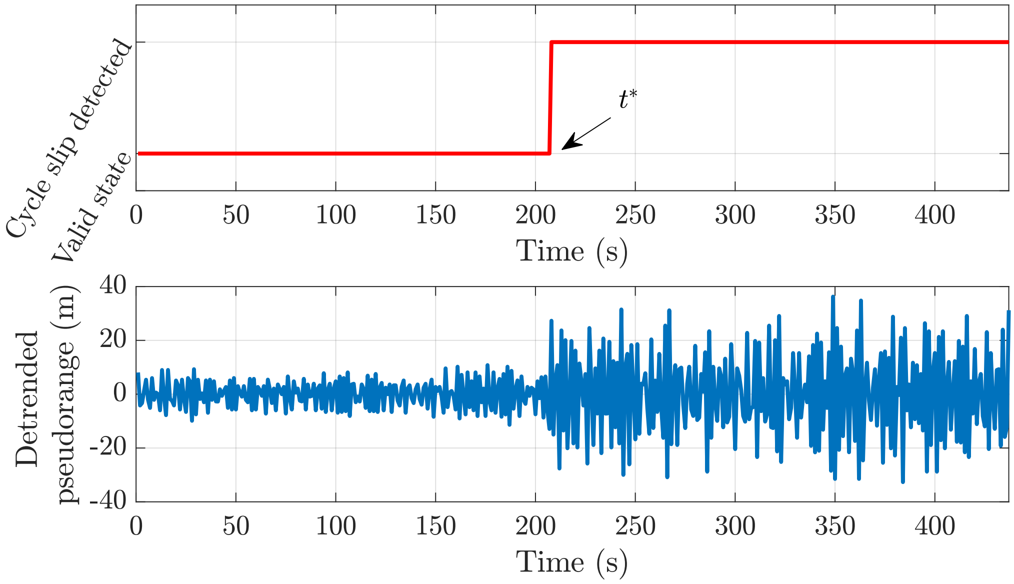

Figure 4.10: Effect of cycle slips in a controlled environment (PRN 23).

Positioning Solutions

The positioning solutions were first obtained by directly post-processing the raw measurements through the WLS algorithm in the GNSS Toolbox without implementing atmospheric corrections. Figure 4.11 displays the horizontal 2-dimensional position solutions of the devices with the true position at the origin in the absence (panel **(a)**) and in the presence of carrier smoothing (panel **(b)**, while panel **(c)** is an enlargement of **(b)**). Looking at the left sided unsmoothed scatter, there appears to be a bias. This is clearer on the smoothed solution on the right side. Precision improves for the solution with smoothing as expected, however with a slight decrease in the accuracy as seen from the figure and from Table 4.2. There is also a deviation visible in the smoothed solution of the Huawei devices which was not clear before.

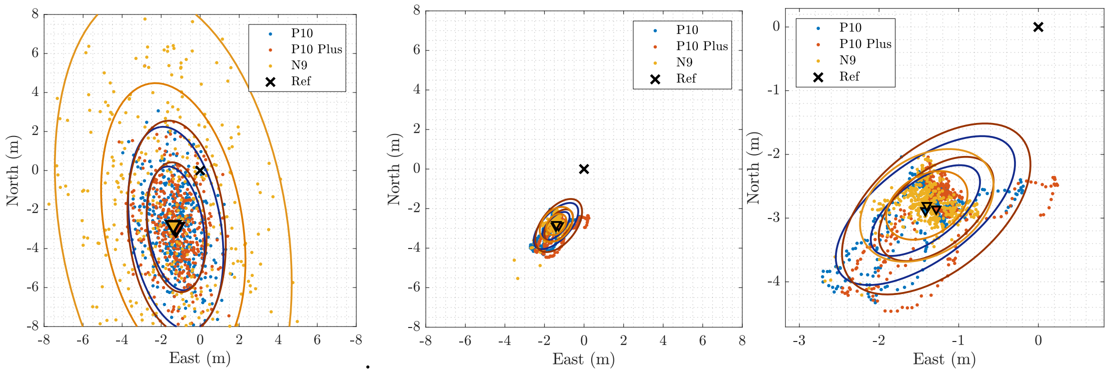

(a) Smoothing OFF.

(b) Smoothing ON with weight $L = 50$.

(c) Smoothing ON (enlargment).

Figure 4.11: Position comparison between devices, in a controlled environment.

Table 4.2: Statistics of the positioning solutions obtained from smartphones inside the anechoic chamber.

	Smoothing OFF			**Smoothing ON**		
Device	**North (m)** $\mu \pm \sigma$	**East (m)** $\mu \pm \sigma$	**Height (m)** $\mu \pm \sigma$	**North (m)** $\mu \pm \sigma$	**East (m)** $\mu \pm \sigma$	**Height (m)** $\mu \pm \sigma$
Huawei P10	-3.0 ± 2.1	-1.3 ± 1.0	-20.1 ± 3.4	-2.9 ± 0.5	-1.4 ± 0.5	-20.2 ± 0.6
Huawei P10 Plus	-2.9 ± 2.2	-1.2 ± 1.0	-20.1 ± 3.2	-2.9 ± 0.5	-1.3 ± 0.5	-19.9 ± 0.7
Nexus 9	-2.8 ± 4.8	-1.4 ± 2.4	-20.2 ± 7.5	-2.8 ± 0.4	-1.4 ± 0.3	-20.2 ± 0.6

To explore further, Figure 4.12 is reported to see the solutions against time and it is seen that there is an event around t^* after which the stability of the Huawei devices worsens. This coincides with the duty cycle effect seen in the raw measurements and the comparison of the raw measurements with the positions can be seen in Figure 4.13. From the figure, it can be established that this event is limited to the Huawei devices and not due to any instability of the signal coming in, as there is no effect seen on the C/N_0 or the Nexus 9 device. Table 4.3 details the error and precision before and after the event in the devices and it has to be noted that the North direction is affected the most, as seen from the figures above as well. The big changes in mean and standard deviation of the Huawei devices is evident when compared to the Nexus 9.

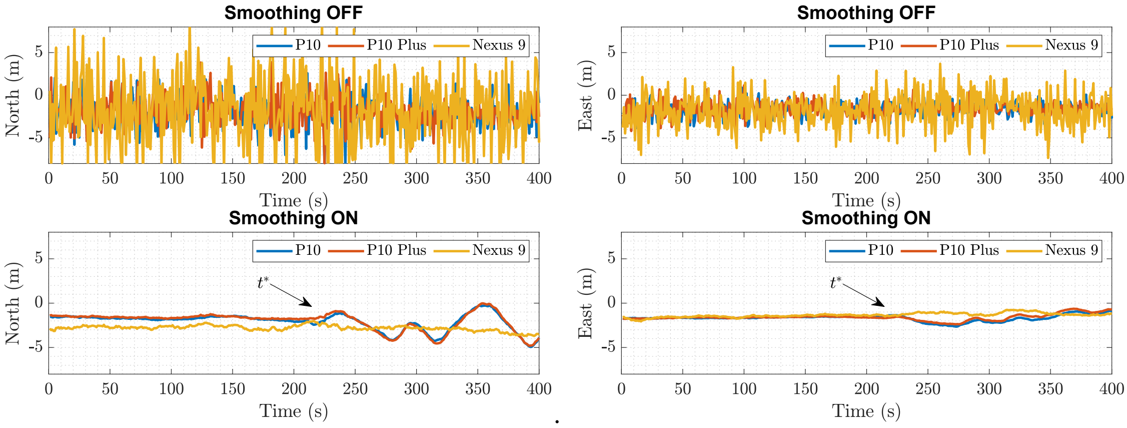

(a) North.

(b) East.

Figure 4.12: Position comparison between devices in a controlled environment.

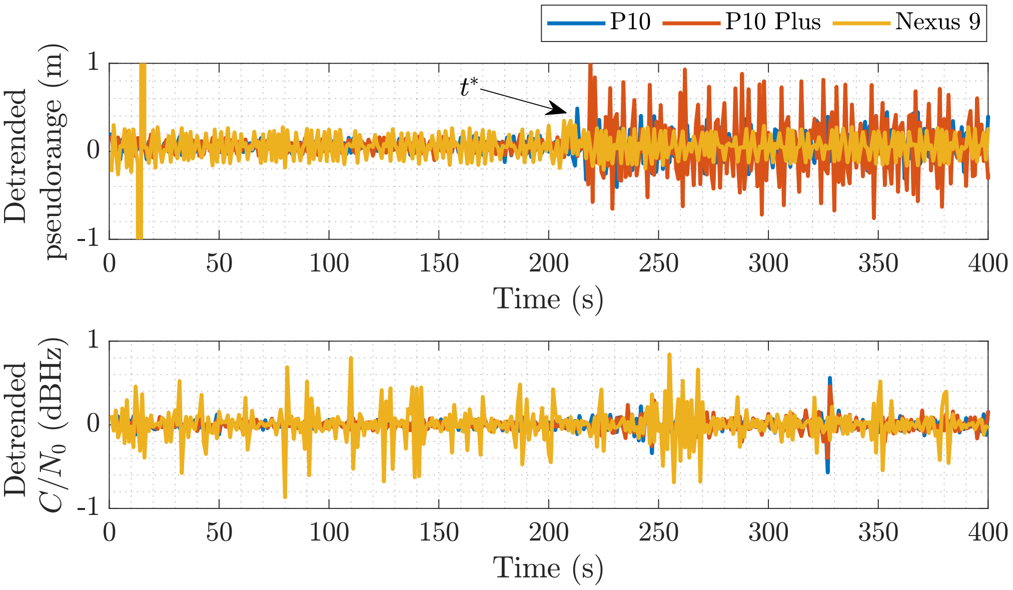

Figure 4.13: PRN 23 (closest) measurements in the controlled environment, highlighting the change around $t^* = 210$ s.

Table 4.3: Statistics of the smoothed positioning solutions obtained from smartphones inside the anechoic chamber, before and after the event.

	Before t^*			**After t^***		
Device	**North (m)** $\mu \pm \sigma$	**East (m)** $\mu \pm \sigma$	**Height (m)** $\mu \pm \sigma$	**North (m)** $\mu \pm \sigma$	**East (m)** $\mu \pm \sigma$	**Height (m)** $\mu \pm \sigma$
Huawei P10	-2.6 ± 0.2	-1.3 ± 0.1	-20.2 ± 0.2	-3.4 ± 0.6	-1.3 ± 0.7	-20.1 ± 1.1
Huawei P10 Plus	-2.5 ± 0.2	-1.3 ± 0.1	-20.1 ± 0.1	-3.6 ± 0.7	-1.1 ± 0.8	-20.1 ± 1.2
Nexus 9	-2.8 ± 0.4	-1.6 ± 0.3	-19.9 ± 0.5	-3.1 ± 0.4	$-1{,}1 \pm 0.2$	-20.7 ± 0.3

In the previous Tables 4.2 and 4.3, the bias in the height measurements is around 20 metres and although it is affected by the event and smoothing, it remains high. Applying ionospheric and tropospheric corrections, this reduces to around 6 metres, as a result of non-perfect correction models and generic uncompensated errors.

An important observation during the position measurement analysis was the effect of a low elevation satellite on the position solution. There was significant deviation seen when including PRN 15 which was visible only partly during the test and this was noticed in all three devices.

Figure 4.14 shows the effects of such a satellite on the positioning results. When compared to Figure 4.11a, in which PRN 15 has been excluded, it is clear that both accuracy and precision increase.

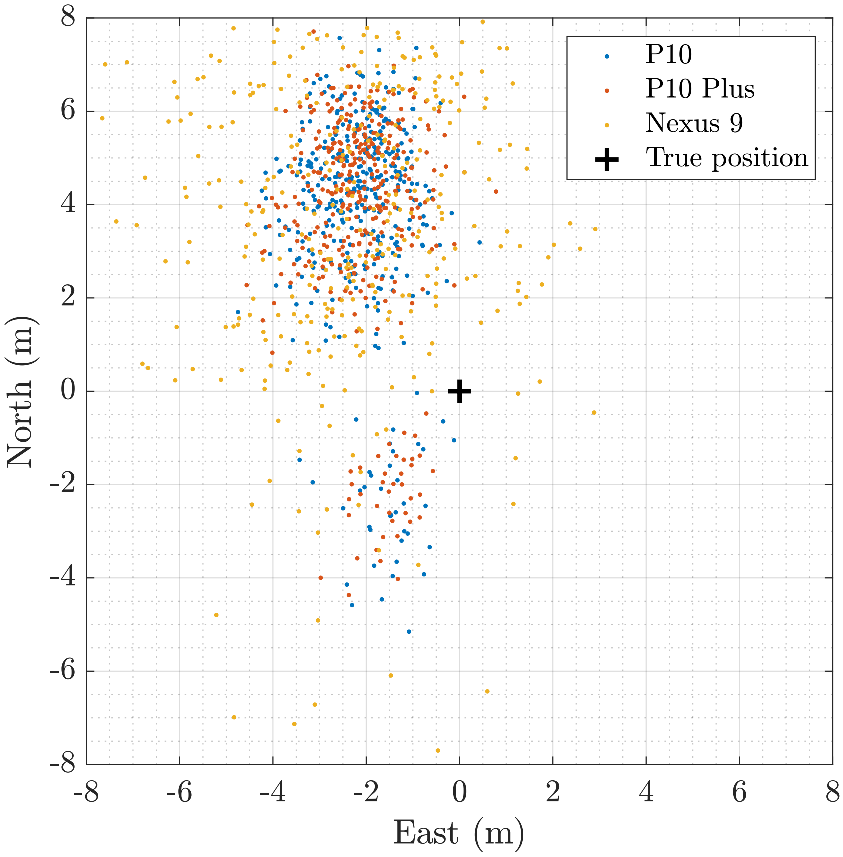

Figure 4.14: Clustering effect due to the presence of a low quality signal (PRN 15), in a controlled environment.

During the presence of this satellite, there is a shift in mainly the North component as seen in panel **(a)** of Figure 4.15. Panel **(b)** depicts a similar low elevation satellite scenario of real environment measurements of P10 and it can be seen that in general such a minor shift should drown out in the noise.

On exploring further it is seen that the problem lies with the use of WLS based PVT algorithm of the Google toolbox while processing the anechoic chamber measurements. In the toolbox, the quality of measurements is weighted based on the receiver clock uncertainty of an incoming satellite measurement [96]. In the anechoic setup of this work, this uncertainty is the same for all satellite measurements due to the replay paradigm through one antenna which makes the weight matrix W an identity matrix in the WLS algorithm, leading to a non-optimized handling of the appearance and disappearance of signals.

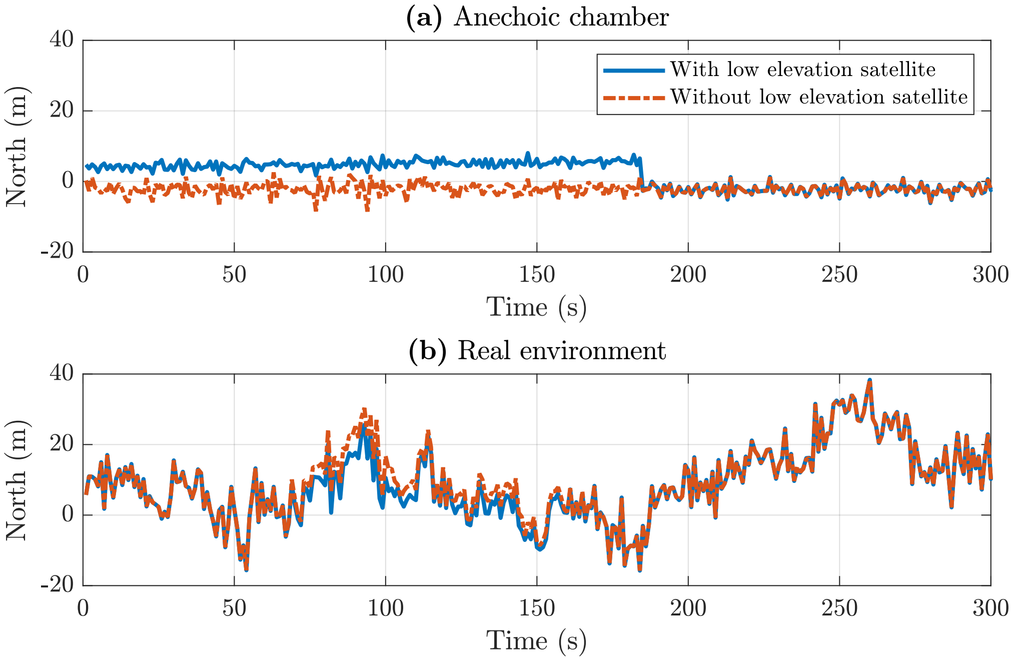

Figure 4.15: Comparison of the positioning results in the presence and in the absence of bad quality measurements.

Chapter 5

Collaborative GNSS Methodology and Application

The chapter presents the work carried out towards the thesis in the field of collaborative and cooperative GNSS. The first section briefly explains a study in deformation monitoring using two GNSS receivers in a master-rover scenario with deflections at the rover side analysed. Thereafter GNSS raw measurements based collaborative ranging between two android smartphones is presented. Finally, the proof of concept application of this collaborative ranging towards positioning is presented in the last section.

5.1 Fast Deformation Monitoring

The priliminary work on GNSS cooperative positioning started with an experimental study proposing the use of two GNSS receivers as master and rover respectively to detect fast structural deformations. Single differenced observations of C/A code and L1 GPS carrier phase are differenced in time to obtain positions and velocities of a rover receiver and the performance of these observations in deformation detection is seen.

A relative positioning approach through iterative Least Squares is explored, in order to detect fast changes in position and velocity of a GNSS receiver installed over a landslide. Both displacements and deformation phenomena are analyzed considering a single difference approach also differenced in time. The rover positions were determined using pseudorange and phase observables with respect to a master receiver and successive epochs whereas the velocity measurements were determined by only the carrier phase observables differenced similarly. One of the peculiarities of the work is to constrain the system considering the baseline between master and rover receivers and their relative velocities, in order to improve the precision and accuracy of the results. The performance of this approach is compared with the performance using a NRTK network; moreover, the performances regarding detection of displacement and deformation is seen. With mass market master-rover receivers, it can be seen that 100% of the deformations at the rover can be detected by monitoring the relative velocities of the receivers, however with a false alarm rate of 20%. Detailed results and methodology of the work are available at [34].

The goal of the work was to check the feasibility of this approach using a least squares post processed method. However the work also highlights the benefits of GNSS CP in applications as critical as landslide monitoring.

5.2 GNSS Collaborative Ranging

The opportunity of implementing collaborative solutions based on raw pseudorange processing for positioning and navigation is attractive in ready-to-network devices like smartphones also considering the computational power of the current hardware setups. Considering the smartphone as an agent in the context of cooperative positioning literature, a double difference inter agent-ranging approach [110, 111] has been implemented in this work which induces the cancellation of common satellite and receiver clock errors affecting the smartphone pseudorange measurements. For such an approach, the feasibility of a low latency communication channel between the devices, dealing with the quality of the raw measurements and real time synchronisation of the devices at an early processing stage are the main challenges to be addressed. This work firstly presents the operational framework for two Xiaomi® Mi8 smartphones equipped with the chipset Broadcom® BCM47755 within the context of collaborative exchange of measurements between them and then the results of an inter-agent cooperative ranging algorithm based on double differencing.

5.2.1 Methodology

The methodology details the procedure followed for implementation of the work using the Android raw GNSS measurements provided through the Android's Application Programming Interface (API) 24 for a set of devices equipped with Android 7 (Nougat) or later releases. The White Paper on using GNSS Raw Measurements on Android devices [94] released by the European Global Navigation Satellite Systems Agency (GSA) in early 2018 defined the raw measurements better for practical use and hence it has been referenced multiple times.

Considering the ubiquitous availability of wireless connections in smart cities (e.g. public Wi-Fi access points, cellular infrastructure), the addressed scenario considers the possibility to have a pair of Android devices sharing data connectivity for the exchange of data, as depicted in Figure 5.1.

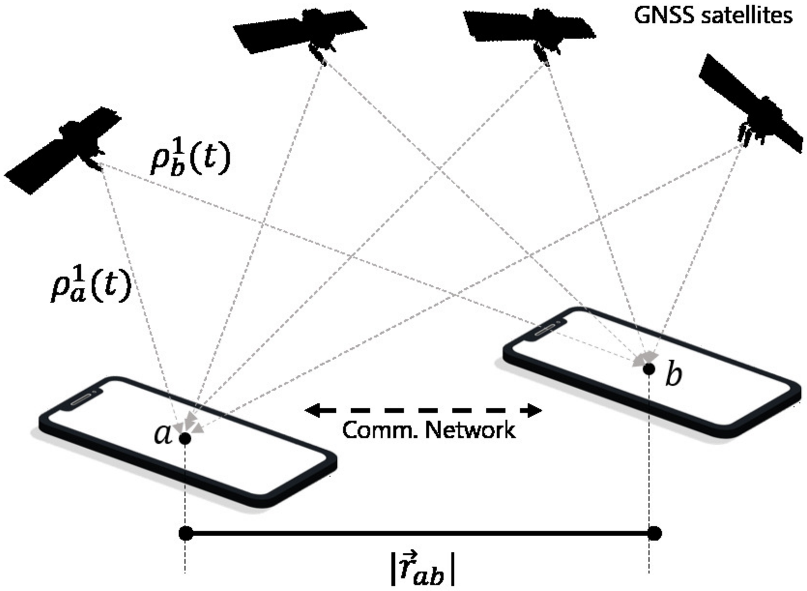

Figure 5.1: Scheme of GNSS-based smartphone inter-agent ranging.

Data exchange

A communication channel is provided through IEEE 802.11b Wi-Fi connection exploiting a client-server service to which two smartphones are connected and registered throughout a predefined access point. Once an update of the measurements is reached by one of the two smartphones, it is sent to the server where it can be forwarded to any listening user. A transmitted packet of raw measurements information is offered by each smartphone and it is structured as in Figure 5.2.

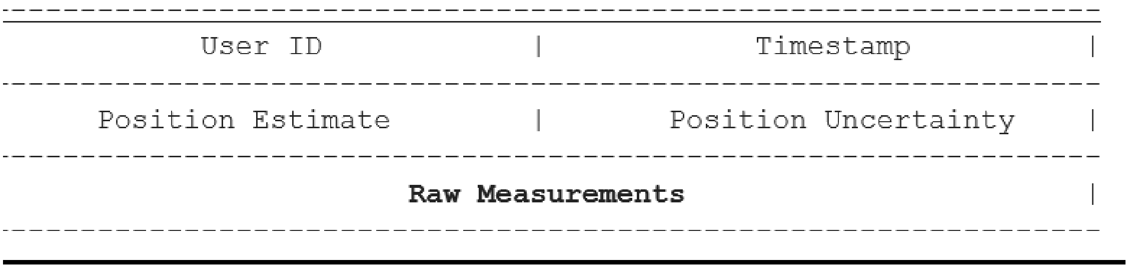

```
-----------------------------------------------------------------
           User ID             |            Timestamp           |
-----------------------------------------------------------------
      Position Estimate        |      Position Uncertainty      |
-----------------------------------------------------------------
                      Raw Measurements                          |
-----------------------------------------------------------------
```

Figure 5.2: High-level packet format for the exchange of raw measurements for cooperative positioning applications.

It is conceived as a multi-cast packet in which the user ID is a unique identifier for the sender. A position estimate and the associated uncertainty is also considered for potential integration algorithms including the collaborative measurement or the knowledge of neighbours locations themselves. The main payload field, named *raw measurements*, contains the satellite-to-agent estimated ranges and the Doppler measurements (provided by the GNSS unit of the smartphone) that can be used by neighbours for the steps described hereafter. Raw pseudorange measurements, identified by the letter ρ as shown in Figure 5.1, are computed by estimating the time of travel of transmitted signal, according to [94]. Such an information is provided as raw data by the Google® Android API. The Doppler measurements identified by the letter ϕ are instead typically provided by the Frequency-locked Loop at the acquisition stage of the receiver [86].

Synchronization of Measurements

Two separate measurements can be aligned with a satellite signal Time of Week (ToW) transmission information, however the actual pseudorange and subsequent raw measurements are not retrieved at a common GNSS or Global Positioning System (GPS) time of both the receivers. The time-consistency of the asynchronous measurements is hence achieved by exploiting a Doppler-based compensation technique [98] which facilitate the merger of asynchronous pseudorange measurements into double-difference based ranging measurements following

$$\rho(t + \Delta t) = \rho(t) + \Delta t \cdot \lambda \cdot \phi(t) \tag{5.1}$$

where λ is the carrier wavelength according to the investigated signals and constellations. The Doppler measurement of a given satellite observed at time t provides an estimate of the pseudorange change rate and can therefore be used to predict the pseudorange in $t + \Delta t$. The correction holds if the relative movement between receiver and satellite is constant and it can be assumed true dealing with static or moderate dynamic of the receiver. The choice of Δt is operated according to the pseudorange estimation method (common receiving time or common transmitting time) [112]. Several solutions for the computation of the range starting from Double Difference have been explored in literature. As an example of application, a plain double difference ranging has been used as reported in the following [99].

The pseudorange generation method used by the android chipset is the common reception time method where all pseudoranges in an epoch and in subsequent epochs are calculated relative to the very first satellite signal to arrive at the first epoch of observation. Theoretically using the raw smartphone clock measurements `BiasNanos` (receiver clock's sub-nanosecond bias), `DriftNanosPerSecond` (receiver clock drift) and `TimeOffsetNanos` (Time offset at which the measurement was taken in nanoseconds), the accurate GPS time of pseudorange measurement can be computed and hence synchronisation can be achieved. The definitions of these measurements are stated in [94]. However, all three measurements are currently unavailable with the BCM47755 chipset for the Xiaomi Mi 8 phone and the alternative was either the use of the clock bias output of a Position, Velocity and Time (PVT) solution for each phone or take use of the `FullBiasNanos` raw measurement provided by the phone. The latter is the direct bias measurement given at each epoch by the smartphone after it has estimated the GPS time through the cellular network and/or the internal PVT solution within the android software [94]. Using it negates the need for a PVT computation for the phones saving valuable processing time and computational power. Thus this allows for the formation of the Δt parameter (as in equation (1)) between the two receivers to be used in a Doppler based adjustion technique.

Relative Range measurements by Double Differencing

When a good synchronization of the measurements is provided, single differences among pseudorange measurements allow to remove the clock biases of the satellite constellation. As a further step, double differences cancel out the user clock bias thus leading to accurate range computation using GNSS observable data only. The use of differential GNSS can rely also on the availability of multi-constellation environments. A single difference can be defined between two GNSS users tracking a common satellite, as

$$s^j_{ab}(t) = \rho^j_a(t) - \rho^j_b(t) - \Delta\rho_{ab}(t) + \Delta b_{ab}(t) + \Delta\epsilon_{ab}(t) \tag{5.2}$$

where Δb_{ab} indicates the bias difference due the users clock offsets and $\Delta\epsilon_{ab}$ includes all the non-common noise related to each satellite-receiver pair.

When the same couple of satellite i and j is visible to both the receivers, a double difference measurement can be obtained as difference of two single differences

$$\begin{aligned} d^j_{ab}(t) &= s^j_{ab}(t) - s^i_{ab}(t) \\ &= \left[\vec{e}^{\,i} - \vec{e}^{\,j}\right] \cdot \vec{r}_{ab}(t) + \left[\Delta\epsilon^i_{ab} - \Delta\epsilon^j_{ab}\right]. \end{aligned} \tag{5.3}$$

On identifying a satellite as a reference, the computation of the range vector, $\vec{r}_{ab}$, can be obtained by solving

$$\mathbf{d}_{ab} = \mathbf{H}\vec{r}_{ab} + \epsilon \tag{5.4}$$

where $\mathbf{d}_{ab}$ is a column vector of double differences w.r.t. the shared satellites and $\mathbf{H}$ is defined with respect to the reference satellite by differentiation of the steering vectors $\vec{e}$, as follows

$$\mathbf{H} = \begin{bmatrix} \left[\vec{e}^{1}(t) - \vec{e}^{0}(t)\right]^{T} \\ \left[\vec{e}^{2}(t) - \vec{e}^{0}(t)\right]^{T} \\ \vdots \\ \left[\vec{e}^{S-1}(t) - \vec{e}^{0}(t)\right]^{T} \end{bmatrix}. \tag{5.5}$$

The range measurement is hence obtained in a Weighted Least Squares (WLS) solution as the norm of the displacement vector $\vec{r}_{ab}$, as

$$\vec{r}_{ab} = \left(\mathbf{H}^{T}\mathbf{R}_{d}\mathbf{H}\right)^{-1}\mathbf{H}^{T}\mathbf{R}_{d}\mathbf{d}_{ab} \tag{5.6}$$

where $\mathbf{R}_d$ is the error covariance matrix associated to the range measurements, whose terms can be retrieved directly through the Android API. Inter-agent ranges are expected to be sufficiently uncorrelated with the measurements used for the further PVT computation so that they can bring further information about the users positions, still according to geometry and quality of the initial estimated position [84].

The example in Figure 5.3 shows the comparison of range estimates obtained at each epoch by means of double differencing of simulated raw measurements according to the methodology in Section 5.2.1, computed between two static GNSS software receivers with a zero baseline. One is a non-weighted asynchronous Double Difference Range (DDR) and the other being the Doppler compensated Weighted Double Difference Range (DDR-W). The measurement noise variance for the simulations is the nominal standard deviation of 6.7 meters (m) as mentioned in [86].

It can be noticed that while the benefit induced by the weighting strategy is limited to a small standard deviation reduction, the compensation of the time misalignment through raw Doppler measurements is fundamental to mitigate the bias in the inter-agent range computation.

5.2.2 Experimental Setup and Results

This section presents a collection of relevant results about the quality of the inter-agent measurements. According to the nomenclature in GNSS literature, the two experiments are classified w.r.t. the length of the true displacement vector, also known as baseline.

Short Baseline Static Test

10-minute static datasets were collected in the campus of the Politecnico Di Torino (45.062099° N, 7.663334° E), Torino, Italy, with two Xiaomi Mi 8 devices 20 meters apart, on the 22nd of February 2019 in a sub-urban sky condition. Android raw measurements were collected through the communication network IEEE

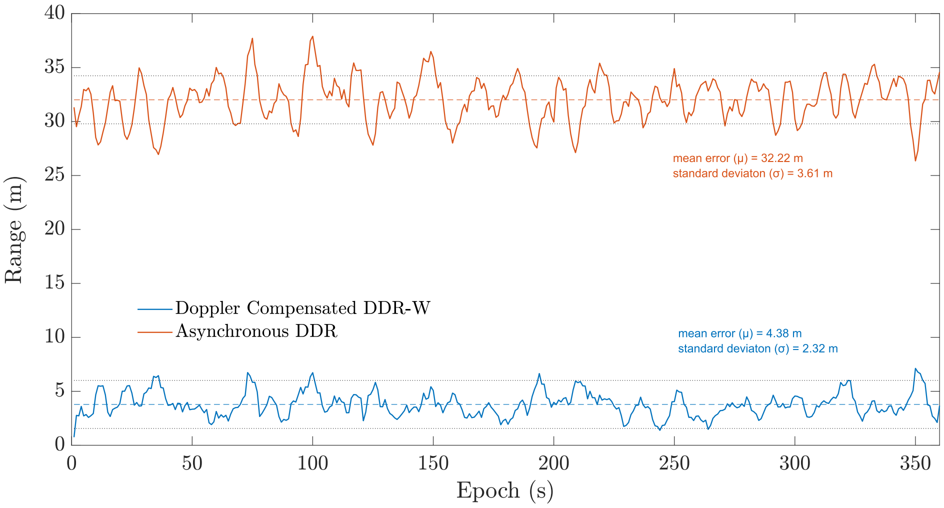

Figure 5.3: Range bias compensation in DDR between two static receivers by means of raw Doppler measurements with simulated GNSS signals (no multipath, 6 GPS satellites).

802.11b Wi-Fi connection and processed through an internal version of the open source MATLAB 'gps-measurement-tools' software [106]. The Xiaomi Mi 8 offers the option to turn off the 'duty cycle' of the device through its developer mode and that was an added consideration during the data collection. Duty cycle is a power saving function of most smart devices where commonly, the hardware clock is switched off for a fraction of every second resulting mainly in carrier phase tracking discontinuity [94]. Although multi-frequency, multi-constellation measurements were recorded, only GPS L1 (1575.42 MHz) signal measurements were processed for initial validation. The use of GPS only does not imply a lack of generality since the same procedure can be applied to the other constellations. Furthermore, multi-constellation implementation is also possible once the user clock bias with respect to each constellation has been removed (i.e. a solution has been obtained).

The unreliable quality of smartphone raw measurements is a hindrance due to poor antenna performance, hence a 'real-time' satellite filtering strategy as well as a weighted solution was adapted based on the parameter ReceivedSvTimeUncertaintyNanos [113]. Three different relative ranges between the phones were compared; DDR and DDR-W (both Doppler compensated) and the Euclidean Range (PVT-R) calculated after standalone-PVT solution computation of the receivers individually. For the standalone solution, some satellites were excluded for a fair comparison with the filtering strategy.

Figure 5.4 shows the basic comparison of the ranges without taking into consideration the quality of the pseudoranges and it is seen that both the ranges are noisy with the PVT-R being slightly better. On filtering out poor measurements,

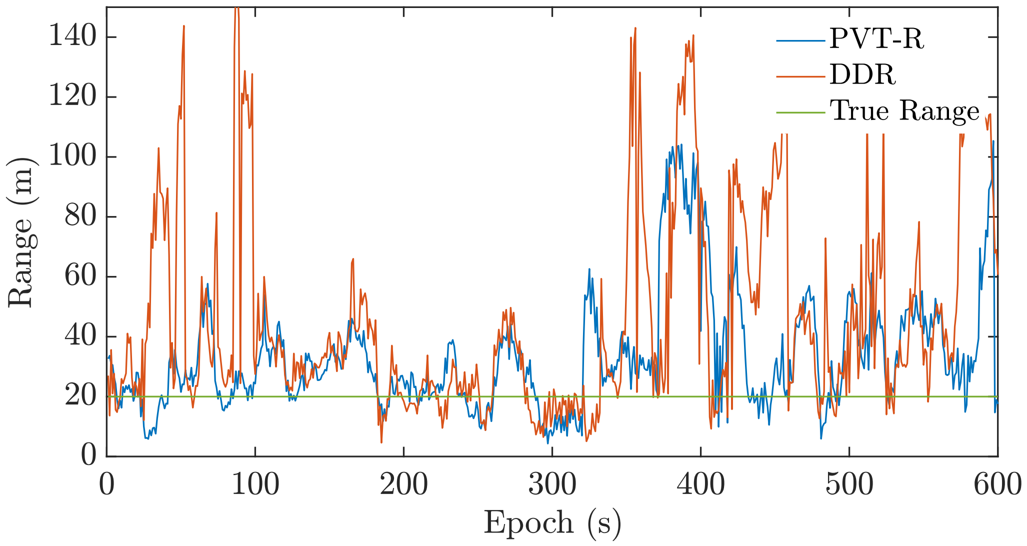

Figure 5.4: 20 m baseline test with DDR and PVT-R comparison.

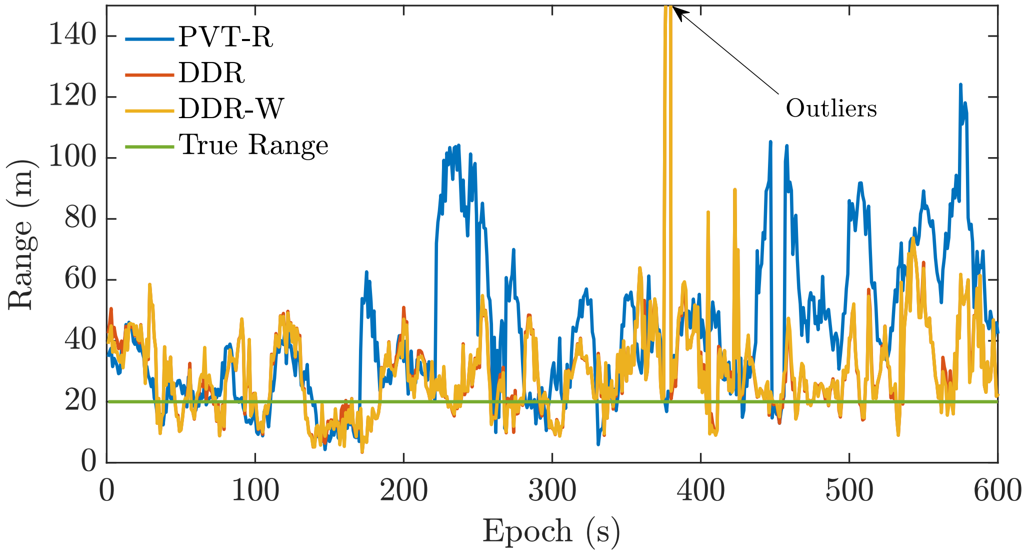

Figure 5.5: 20 m baseline test with DDR, DDR-W and PVT-R comparison.

significant improvement to the DDR and DDR-W ranges is seen in Figure 5.5 and it is in general better than the PVT-range, barring a few outliers which the weighted solution fails to take account of. The mean GDOP value was around 2 and 2.5 before and after filtering respectively. This observation is consistent with the other dataset measurements and in dataset 3 (5-minute observation), the improvement in the mean error is 4-5 times higher. Table I presents a comparison of the quality of the GNSS-based ranges in the different datasets with respect to the standard deviation (σ) and mean error (μ). There is still a significant bias and noise present in the measurements due to the uncorrelated noise being quadrupled after double differencing, as shown in [114], but this relatively superior range output produced taking advantage of Android raw measurements only without the PVT computational burden opens an interesting application of cooperation among Android smartphones.

Table 5.1: Comparison of the quality of GNSS-based ranges

Test with two Xiaomi Mi-8 devices		**600 s interval**		
		PVT-R	DDR	DDR-W
DATASET 1	σ (m)	19.4	12.2	12.1
	μ (m)	10.5	9.9	7.6
DATASET 2	σ (m)	9.5	8.7	8.6
	μ (m)	8.4	5.4	5.4
DATASET 3	σ (m)	18.2	10.4	10.2
	μ (m)	24.7	6.3	5.8

Zero Baseline Static Test

Following this, the presented strategy was also applied to a simple zero-baseline test performed on the rooftop (open sky condition) of the Politecnico Di Torino campus, Torino, Italy (45.063780° N, 7.662003° E) by placing two Xiaomi Mi 8 Pro phones next to each other on the 15th of March, 2019.

In addition to filtering of the satellites, the Doppler compensated pseudoranges for DDR and DDR-W were further smoothed based on their Doppler ranges [115] and there was a significant quality enhancement with the near complete removal of a bias seen in the PVT-R as seen in Figure 5.6. The mean error and standard deviation of the latter was 6.6 m and 3.1 m respectively. In comparison for the DDR and DDR-W, the mean errors were 1.5 m and 1.4 m respectively with the standard deviations being 1.2 meters for both. The mean GDOP value was around 2.5 during the test with an average of 5 satellites considered after filtering out the poor measurements. The smoothing strategy has not been implemented to be robust yet for urban or sub-urban sky conditions, hence further development has to be done.

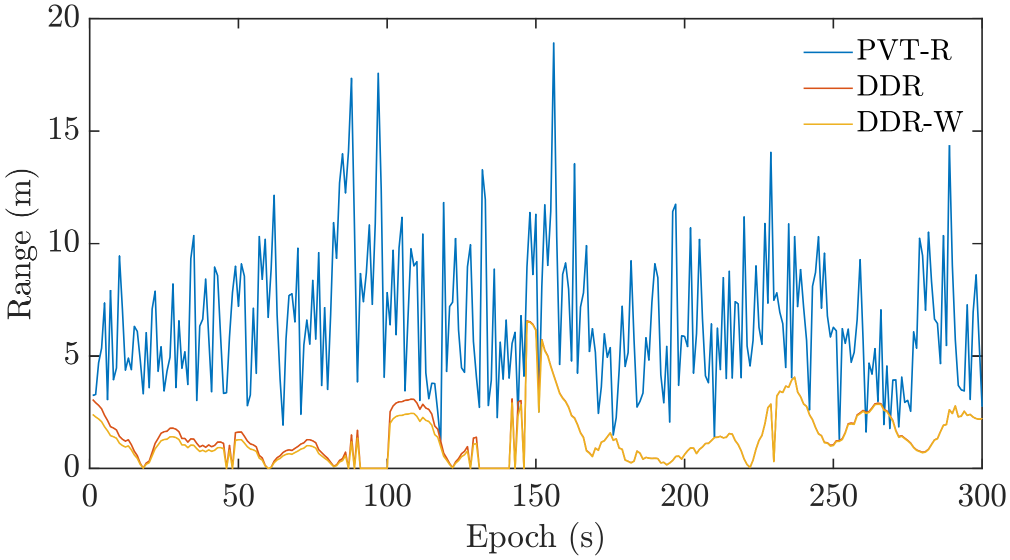

Figure 5.6: DDR and DDR-W applied on smoothed pseudorange measurements, compared to PVT-R.

5.3 Proof of Concept - Cooperative DGNSS

This work aims at defining a new UAV-UGV collaborative positioning paradigm by assessing the feasibility of a DGNSS-based cooperative strategy presented in [116] for connected GNSS receivers. A proof of concept of this technology has been developed on Google Android™ smartphones which natively support both GNSS navigation and data connectivity in 4G/LTE.

5.3.1 Proposed framework

The architecture of the proposed collaborative framework is designed to overcome the limitations of direct communication strategies such as Direct Short Range Communications (DSRC) and Wi-Fi direct. It is indeed designed to exploit commercial cellular networks to support the functional exchange of data among the agents. As shown in Figure 5.8, two smartphones were exploited to allow network communication and navigation capabilities to the UAV and UGV respectively exploiting on board Broadcom GNSS chipset and 4G network connectivity.

Furthermore, the network interface has been used by the UAV to transmit raw pseudorange measurements to the UGV to perform collaborative ranging, thus enabling the rover to perform collaborative positioning without the need of additional sensors to achieve the required accuracy for the application.

Section 5.2 opened the investigation to the DGNSS-CP based on the inter-device

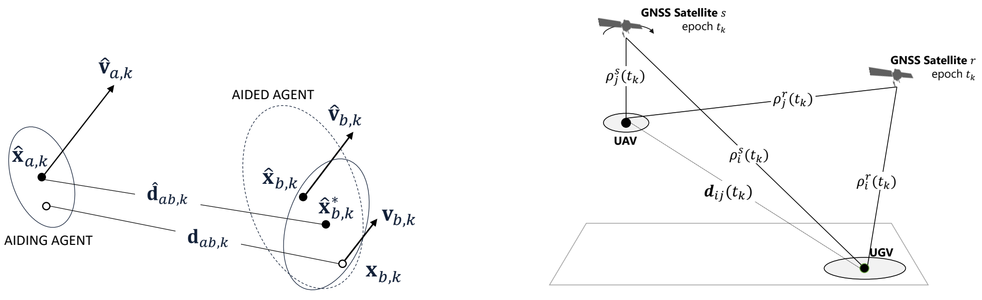

(a) (b)

Figure 5.7: Range-based CP concept and pictorial scheme representing its implementation through Double Differences applied to GNSS pseudorange measurements to determine the inter-receiver distance and support DGNSS cooperative positioning and navigation.

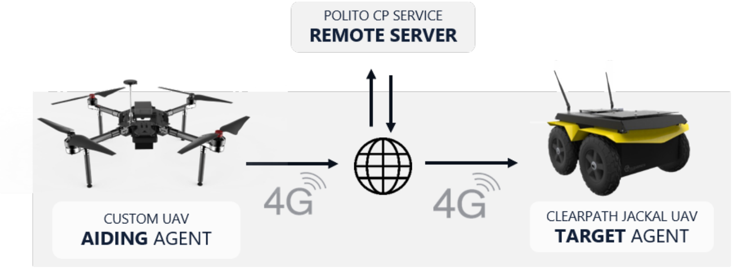

Figure 5.8: High-level block scheme of the experimental setup.

range from GNSS raw measurements between two Android devices within a communication framework [117]. The availability of cooperative algorithms applied to the GNSS pushed researchers to design new frameworks to cope with the limitations of traditional approaches. The DGNSS-CP framework investigated in this work supports the exchange of raw GNSS measurements among multiple receivers interconnected by 4G/LTE or Wi-Fi 802.11x connectivity executed through an Android application. The measurements are hence synchronized through a Doppler compensation technique [114] and the inter-agent distance is computed through a differential GNSS approach.

The DGNSS-CP framework exploited in this work acts according to the following steps for each PVT epoch, t_k

1. The UAV sends to the UGV its set of raw pseudorange measurements $\boldsymbol{\rho}_{\mathrm{UAV}}(t_k)$ and the estimated position $\hat{\mathbf{x}}_{\mathrm{UAV}}(t_k)$ with an associated timestamp t_k. This is achieved through the 4G/LTE connection of the two Android devices.

2. The UGV aligns the external set of measurements retrieved from the UAV $\boldsymbol{\rho}_{\mathrm{UAV}}(t_k)$, to the closest set of GNSS raw measurements locally dumped by

exploiting a raw measurement output for the timestamp and the Doppler compensation technique through the Android application.

3. The UGV combines the local and external pseudorange measurements to determine the inter-agent distance between the UAV and UGV through the GNSS double differencing methodology presented in [118].

4. The UGV integrates such inter-agent distance w.r.t. the position of the UAV (consistent) along with local pseudorange measurements within its navigation algorithm. This is done by first considering the inter-agent distance as an added measurement in the generic standalone measurement vector of satellite-to-receiver pseudoranges and then using the Extended Kalman Filter (EKF) algorithm [85] for the navigation solution.

In a harsh environment, the position estimation of UGV can be generally improved by the additional information carried by the set of pseudorange measurements shared by other receivers and it is not expected to show any particular drift [119]. These benefits are mostly due to an improved geometry (reduced dilution of precision) of the ranging information [119, 120] and multipath error cancellation when GNSS signals collected by collaborating agents experience similar reflected paths.

Technical details concerning the implementation of the framework can be found in [121, 82, 116] and in the technical documentation of the proof-of-concept realized in the framework of the ESA project HANSEL.

5.3.2 Experimental setup and performance metrics

In order to test the feasibility of the proposed approach, an UAV and an UGV were deployed in an open test field in Turin, Italy near to a reference location coordinates of 45.0430N, 7.5395E. The test field, shown in Figure 5.10, has been selected to verify the performance of the algorithm in open sky conditions. In such condition the accuracy improvement due to cooperation is expected to be limited and in parallel, the availability of a 4G/LTE satisfying signal coverage could be limited. Two Xiaomi Mi8 Pro smartphones equipped with Android 9, were chosen as a testbed hardware of the proposed technologies.

The devices were stably mounted on the rover and on the drone through specific supports, as shown in Figure 5.10a and Figure 5.10b. A proprietary Android™ application was run on the smartphones to collect GNSS raw data during the tests and compute both the standalone GNSS and the cooperative positioning solution according to the framework discussed in Section 5.3.1. The latter is achieved by receiving and integrating run-time UAV satellite pseudoranges and then computing the collaborative differential range according to the tight-integration approach presented in [82, 121].

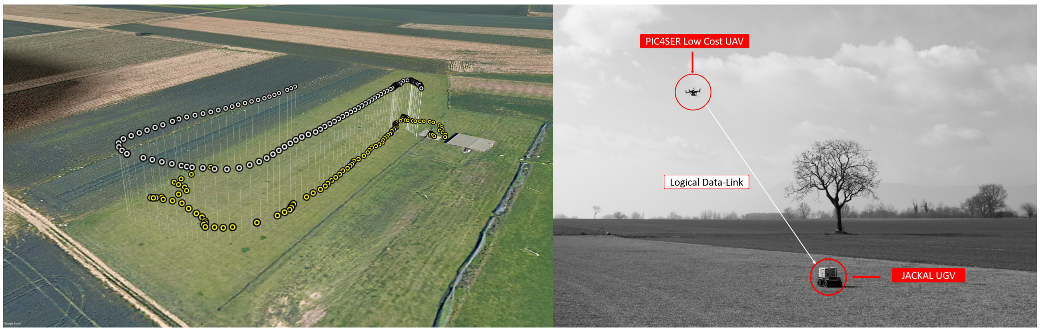

(a) (b)

Figure 5.9: GNSS fixes of UAV and UGV in follow-me configuration shown in Google Earth (5.9a) and in real scenario (5.9b).

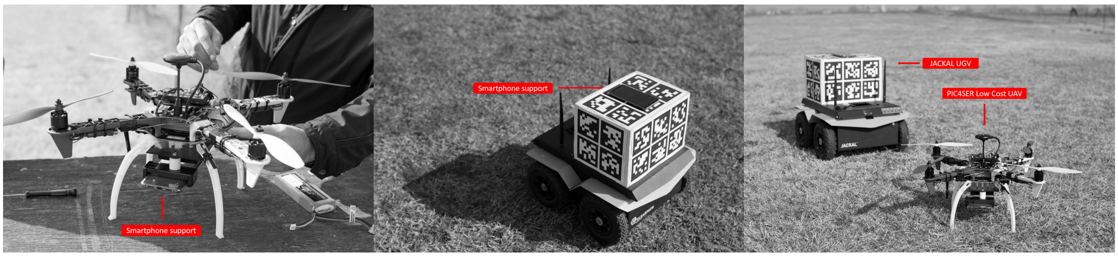

(a) (b) (c)

Figure 5.10: Hardware setup for UAV and UGV during on-field experiments.

It is worth remarking that the cooperation was allowed bidirectionally to ensure the availability of CP solutions to both the agents. This is off-course unnecessary in a real implementation but it is helpful to highlight the unidirectional effectiveness of the paradigm within this specific application, as it will be detailed in Section 5.3.3.

The reference position was provided by the Google Fused Location Provider considering that at the moment, it uses measurements of GPS (when it's available), cell-tower signal strength and Wi-Fi Received Signal Strength (RSS), and fuses them with the onboard proprioceptive sensors: inertial navigation from the accelerometer, gyro and compass [122].

Experiments

Three class of tests were performed to test the paradigm:

- **Follow-me mode**: The UAV was manually and remotely controlled to follow the UGV along its path/trajectory. The distance was kept roughly constant (about 10 m) between the agents. This test was conceived to exploit UAV specifically to improve navigation capabilities of the UGV and was inspired to the Martian helicopter support mission [123] .

- **Independent hovering**: Operators independently drove the UAV and the UGV on different paths/trajectories. This test emulates an occasional collaboration for positioning and navigation purposes when the agents are performing independent tasks.
- **Partially-obstructed LoS**: This specific scenario was intended to demonstrate a different CP profitability when obstacles occlude the LoS towards GNSS satellites for the ground vehicle. In this case, the UGV was driven underneath a shack where laptops and accessories were temporary stored, while the UAV was kept hovering the area at about 20 meters height.

Performance metrics

RMS error is typically used to evaluate the positioning error but in real experiments we deal with a single positioning solution per each time instant, t_k. Therefore, the positioning error can be simply evaluated as the Euclidean distance of the estimated position from the reference position provided by the Google Fused Location Provider in 3D (considering spatial accuracy)

$$\xi_{3\mathrm{D},k} = \sqrt{(\Delta E_k^2 + \Delta N_k^2 + \Delta U_k^2)} \tag{5.7}$$

and in 2D (considering horizontal accuracy)

$$\xi_{2\mathrm{D},k} = \sqrt{(\Delta E_k^2 + \Delta N_k^2)} \tag{5.8}$$

where the squared terms in (5.8) and (5.7) are the difference of each component in a ENU reference frame [85]. It is helpful to recall that ENU coordinates are obtained from linear transformation of ECEF coordinates so that (5.7) can be equivalently computed in ECEF.

A *Mean CP error* (2-D,3-D), defined as $\mathcal{E}_{\mathrm{CP}}$ (m) can be computes through the mean positioning errors of CP w.r.t. Google Fusion Location Provider over the time epochs in which CP is profitable.

$$\mathcal{E}_{\mathrm{CP}} = \frac{1}{W}\sum_{w=1}^{W} \xi_k \tag{5.9}$$

where $W = \sum p_k$ counts the overall amount of profitable epochs, formally $\forall k | p_k = 1$. In order to define a *profitable epoch* the flag, p_k, assumes values according to the following conditions

$$\begin{cases} p_k = 0 & \xi_{\mathrm{SA},k} - \xi_{\mathrm{CP},k} < -T_H \\ p_k = 1 & \xi_{\mathrm{SA},k} - \xi_{\mathrm{CP},k} > +T_H \end{cases}$$

where T_H is a threshold used to perform a conservative classification of profitable/unprofitable epochs. A further conditions defined according to T_H and named *hysteresis*, identifies a region of non-significant improvement/worsening in accuracy.

Regarding standalone GNSS positioning, $\mathcal{E}_{\text{SA}}$ (m) equivalent to $\mathcal{E}_{\text{CP}}$ is evaluated for the GNSS standalone solution.

5.3.3 Results

The tests showed that the network-based transmission of the data was suitable for a real time integration of the exchanged measurements. Auxiliary UAV→UGV range measurements computed by the UGV through the pseudorange and Doppler measurements provided by the UAV, were successfully integrated. Results are limited to the number of effective epochs during which the two systems were able to cooperate. Limiting conditions such as network latency and poor signal coverage of the 4G/LTE cellular network on the test field indeed reduced the cooperation between UAV and UGV.

The right barplot in Figure 5.11 highlights a higher accuracy improvement when satellite visibility, thus GDOP is reduced for the UGV which was travelling underneath a covered area of the field (in correspondence of the shack visible in the right side of Figure 5.9a.

Additional range measurements obtained along with the estimated position of the UAV allowed to reduce the positioning error of the GNSS-standalone solution up to the 48% in 3D and 58% in 2D, as shown in the right plot of Figure 5.11 for the Follow-me mode. It is to be noted that there was no improvement in the 2D positioning solution for the Independent hovering and Partially-pbstructed LoS modes. Looking at the Cumulative Density Functions (CDFs) of the first test (Follow-me mode) in Figure 5.12, we notice the sharp behaviour of the curves due to the low statistics collected. Despite this, it can be noticed that for the fixes computed by the UGV with an error in the range of 20-30 m (area highlighted in grey), the DGNSS-CP provided a visible improvement. As expected, cooperation was not beneficial for the UAV which experienced already satisfying GNSS performance.

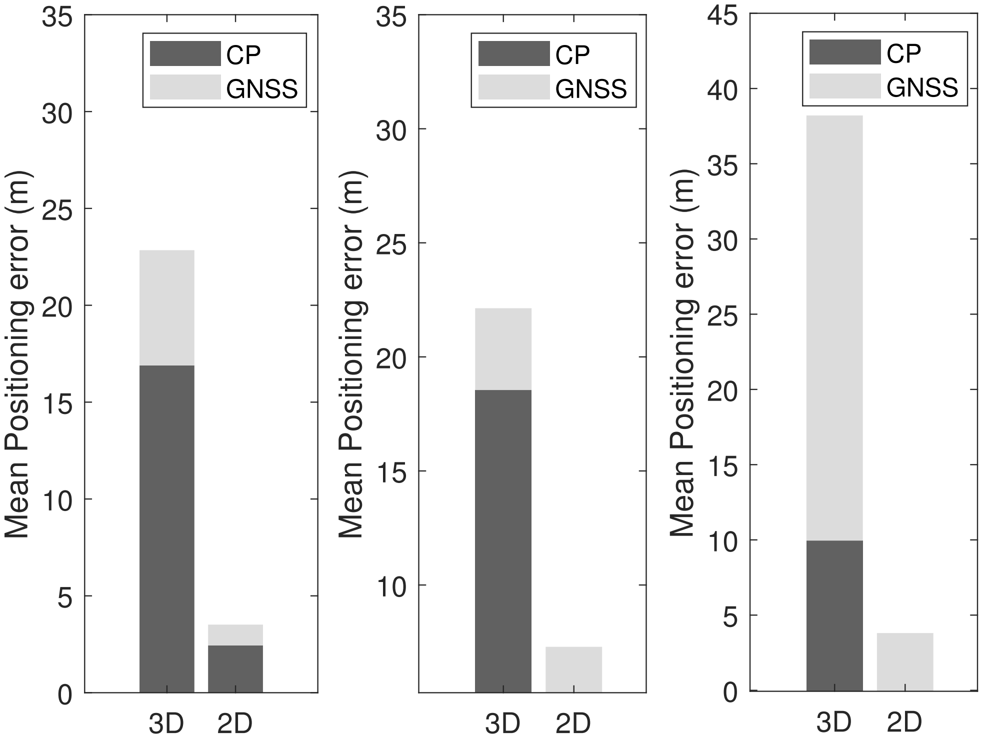

Figure 5.11: Barplots showing the reduction in the positioning error of the UGV provided by profitable Cooperative Positioning (CP) for each class of experiments, Follow-me mode (left), Independent hovering (center) and Partially-obstructed LoS(right).

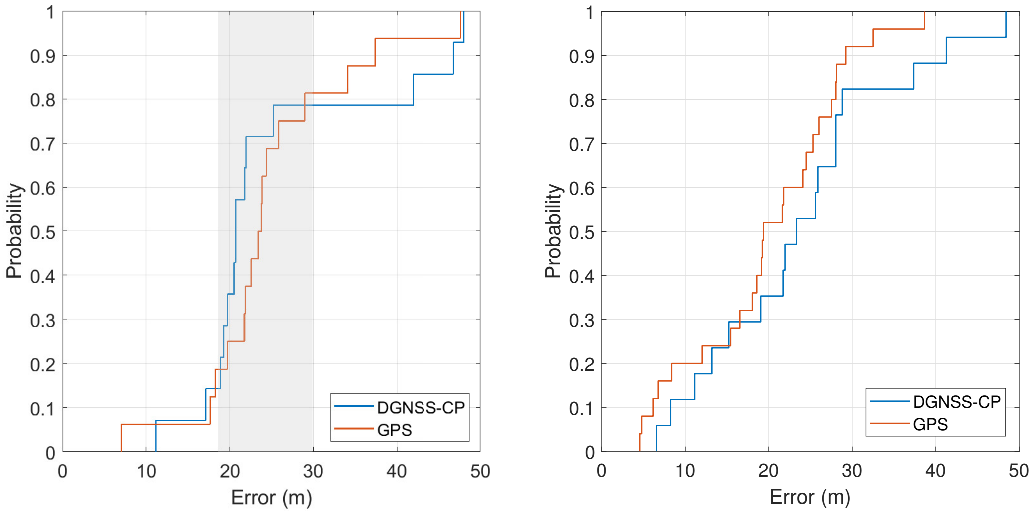

(a)

(b)

Figure 5.12: Example of comparison of the CDFs computed through the post-processing of GNSS-only positioning solutions for UGV (5.12a) and UAV (5.12b) for the Follow-me mode.

Chapter 6

Interference Threats to GNSS in Service Robotics

The chapter presents the work carried out towards the thesis to study interference threats to GNSS receivers. In the first section, an assesment of the vulnerability of different COTS GNSS receivers is carried out by tests in an anechoic chamber. A more detailed analysis is carried out in the next section, presenting the effects of spoofing in raw GNSS measurements of Android smartphones. The last section presents an arguement for cooperative positioning as a defence against interference.

6.1 Overview and Assessment of Vulnerability

In recent years, mass-market applications relying on user positioning has increased significantly increase and as a consequence, more precise and reliable services are demanded. However, due to the weakness of GNSS signals, the GNSS receiver performance could be easily disrupted by anthropogenic disturbances, i.e. jamming and spoofing. The swept-frequency jamming signal is a typical intentional Radio Frequency Interference (RFI) that can be broadcasted by the Personal Privacy Devices (PPDs) with carrier frequency varying over the GNSS bands. Whereas the spoofing refers to the transmission of counterfeit GNSS like signals, with the intention to generate false position at the victim receivers without disrupting the GNSS receiver operation.

The countermeasures for the threats of jamming and spoofing have been extensively discussed and proposed in the literatures [124, 125]. The new generation of the high-end GNSS receivers already start to integrate RFI detection and mitigation units based on advanced signal processing techniques to counteract jamming signals at Intermediate Frequency (IF) level before the correlation process performed. Some of the extensively investigated pre-mitigation techniques including Adaptive

Notch Filtering [127, 126] and Wavelet Packet Decomposition [128]. Compared to the jamming disturbance which could significantly influence parameters at the receiver level thus allowing easy detection, the spoofing disturbance challanges the detectors as the receiver operation is not interrupted.

Depending on the features of the spoofing characteristics and complexity, it is possible to classify the spoofing disturbance into three categories: simplistic, intermediate and sophisticated [124, 129]. The simplistic spoofing is the one chosen to test in the experimental scenarios which is technically possible to be counteracted since the time flag of the spoofing signal is not strictly synchronized with the real GNSS signals. However, being the design of most of the mass-market navigation unit driven by low-cost, low-power, small-size requirements, they hardly implement anti-jamming and anti-spoofing techniques that would increase the complexity of the system. As of today, the risks induced by jamming and spoofing are not yet perceived as a major, widespread, threat. Therefore, it is worth investigating the impairment of these anthropogenic disturbances on the low-cost positioning and navigation units integrated in the mass-market receivers and further to estimate their resilience to the attacks. In this regard, two classes of navigation unit designed for drones and a smartphone with integrated GNSS units are selected for the assessment. Previous assessment of drones in an anechoic chamber has been performed in [130] and [131].

Several experimental scenarios were designed in this work to estimate the effects of the jamming and spoofing. The tests are performed in an anechoic chamber with realistic jammer and spoofer employed to generate disturbances on the GNSS L1 signal transmitted by a signal generator. Performance of the different drones under the intentional disturbances are examined.

6.1.1 Experimental Setup

Jamming Scenario

Figure 6.1 presents a generic block diagram for the setup to carry out interference tests on GNSS receivers. GNSS inputs (top left of the figure) and interference inputs (bottom left of the figure) are combined to be fed to the front end of GNSS receivers or broadcasted directly through an antenna in a controlled scenario. An overall experimental setup in the anechoic chamber for the test scenarios carried out in this work is shown in Figure 6.2.

Dual GPS frequency signals, i.e. L1 and L5 are intentionally configured and broadcasted by a signal simulator through a transmitting antenna in the anechoic chamber. Three types of drones, including a popular commercial drone and a customized drones with PX4 autopilot [132] were tested under different jamming and spoofing scenarios for sake of comparison. Henceforth, these drones are referred as UAV1 and UAV2 respectively. The estimation is based on the output of the

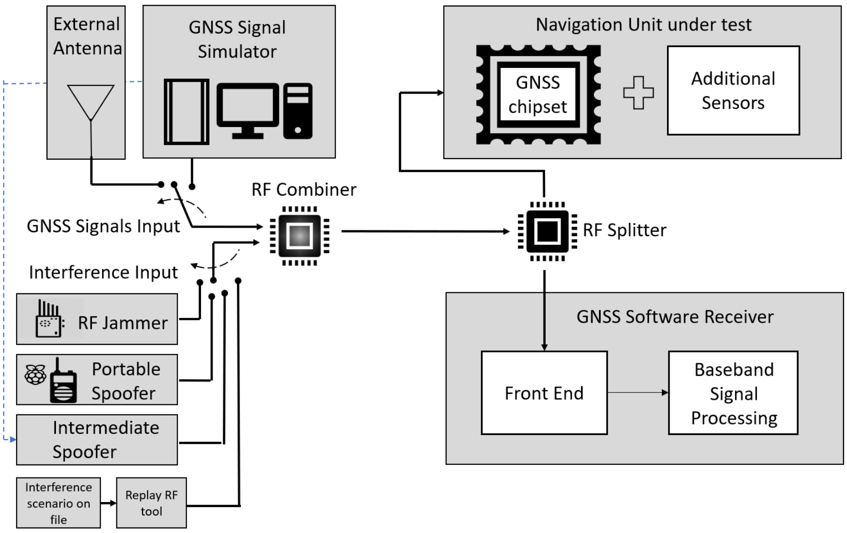

Figure 6.1: Generic block diagram of interference test setup

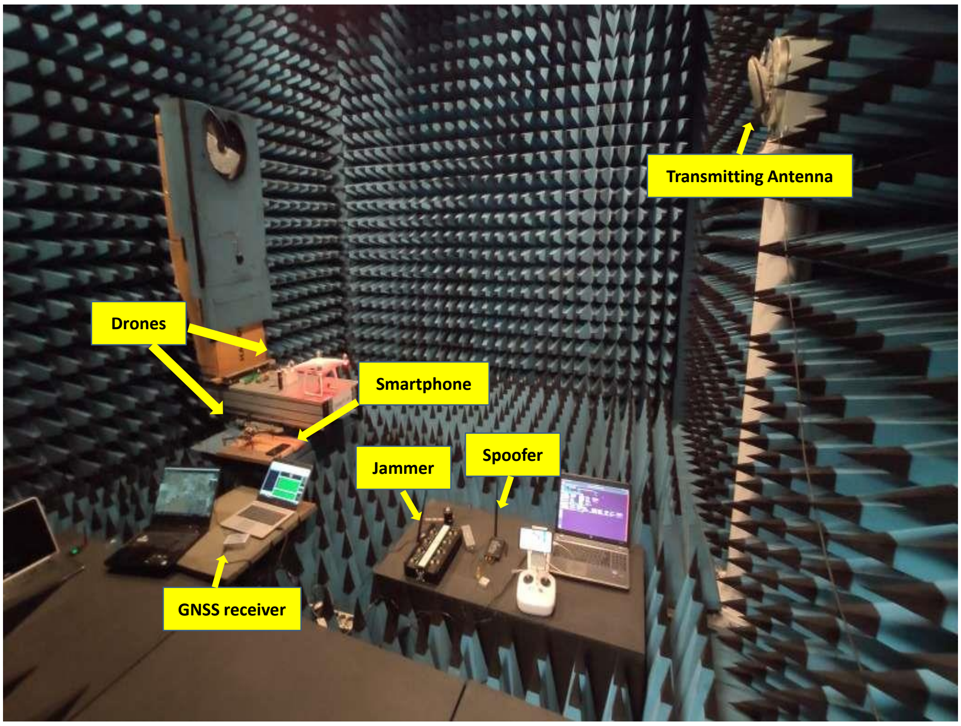

Figure 6.2: Experimental setup in the anechoic chamber.

devices under jamming and spoofing disturbances. Furthermore, a commercial GNSS receiver is used as a benchmark for data collection and PVT estimation for comparison purpose. The linear chirp signals varying over the GPS L1 band are generated by a "commercial" jammer with additional variable attenuation to control the output power level. A low-cost spoofer implemented by using a HackRF One front-end [133] with Software-Defined GPS signal simulator is employed to simulate the spoofing signals. The test scenario for the jamming investigation is defined decreasing the attenuation of the jammer along time.

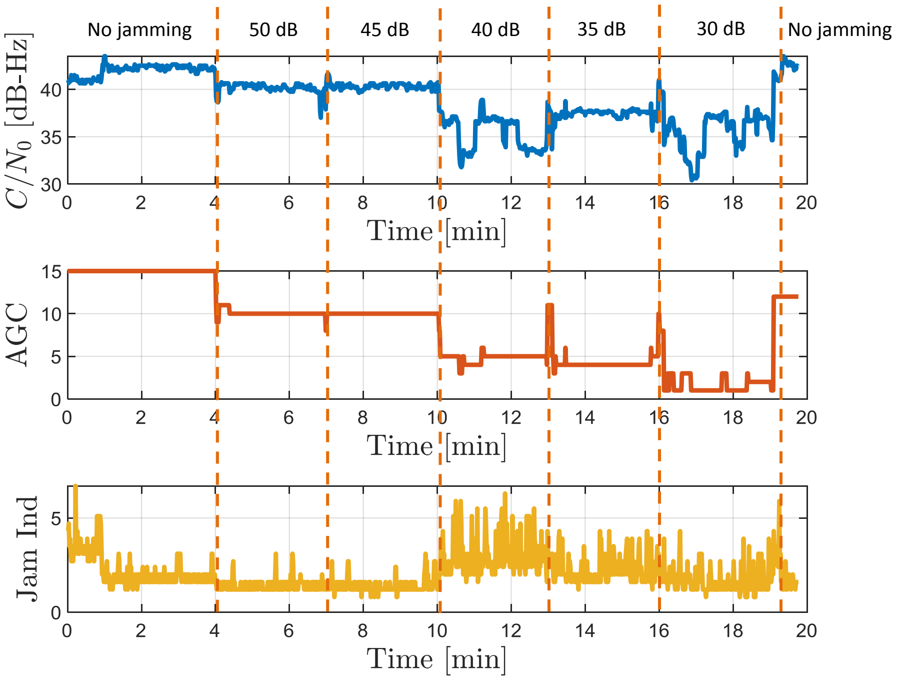

Figure 6.3: Parameters of the commercial receiver under jamming activities.

The first 4 minutes are under the clean simulated GNSS signals, in absence of any jamming signals. Starting from the 5th minute, the jammer is switched on to broadcast linear chirp signals over GPS L1 bands as disturbances. With the variable attenuator, the power level of the output chirp signals is increased at a step of 5 dB every 3 minutes during the test. The jamming activities of the test scenario can be easily noticed by checking the commercial receiver (benchmark) performance as depicted in Figure 6.3. The values on the top of the figure stands for the attenuation level in dBs. A smaller value of the attenuation refers to a stronger power level of the jamming signal. It can be seen in the figure how the jamming activity influence the receiver. The estimated position by the benchmark receiver is shown in Figure 6.4. A noticeable degradation of the performance appears around the 11th minute when the total attenuation of the jamming signal changed to 40 dB, reflecting the resistance of the benchmark receiver towards the jamming signals.

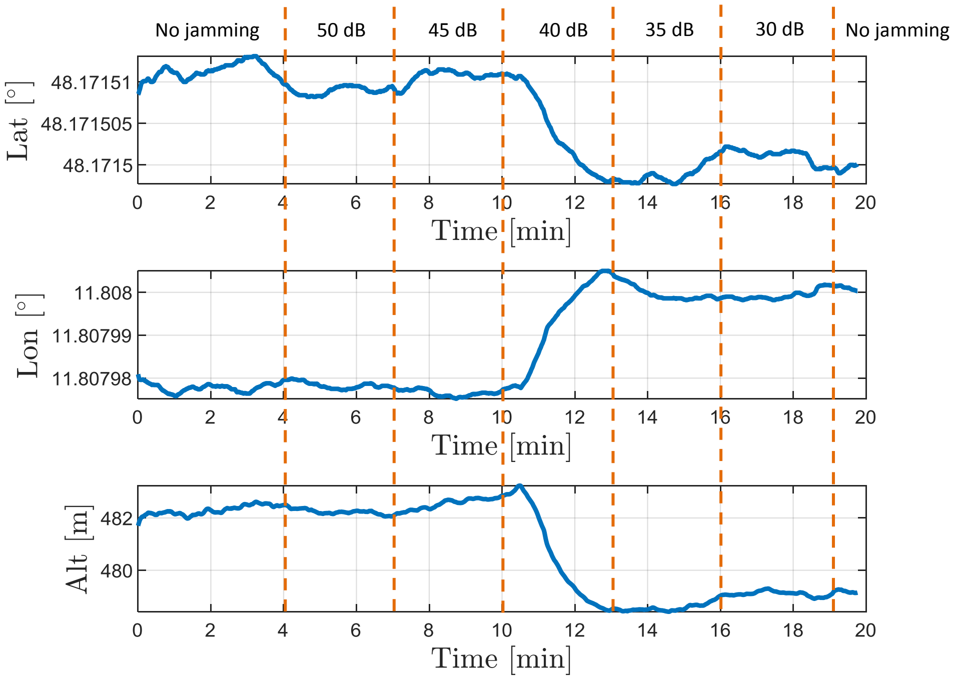

Figure 6.4: Estimated position of the commercial receiver as benchmark.

Spoofing Scenario

The spoofing investigation scenario is defined along 10 minutes of simulated signals. In the first 2.5 minutes, clean simulated GNSS signals with coordinates 48.1715N, 11.808E (Poing, Germany) are transmitted in absence of any spoofing signals. Following this first phase, the HackRF One frontend is switched on with running Software-Defined GPS signal simulator, thus to broadcast spoofing signals over GPS L1 band in order to force the receiver to compute the position with coordinates 48.17878N, 11.79368E, which is 1.3 km away from the initial location. The spoofing activities lasted for 5 minutes before stopped and followed by another 2.5-minutes with only clean simulated signals.

6.1.2 Analysis of the RFI Effects on the Navigation Performance

Under Jamming

For UAV 1, the position obtained from the GPS unit and the IMU unit are shown respectively in Figure 6.5 and Figure 6.6.

As it can be seen, the commercial drone shows very similar performance compared to the performance of the benchmark receiver in terms of the resistance to the

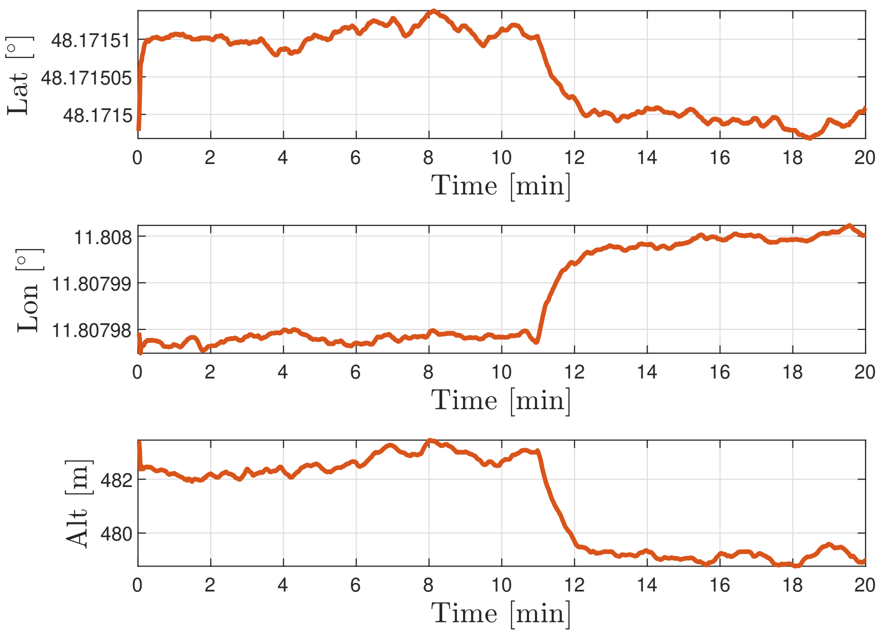

Figure 6.5: Estimated position by GPS unit from UAV 1 under jamming

jamming activities. Other parameters from the sensors have also been evaluated. However, no significant influence is monitored due to the presence of the jammer. This is expected due to the physical nature of the sensors and are not affetcted by RFI. However, compared to UAV 1, UAV 2 is more vulnerable to the jamming activities. UAV 2 is only capable to obtain the position in the first 7 minutes and when the attenuation is smaller than 45 dB, operations are interrupted and no data collection is available, as depicted in Figure 6.7.

Under Spoofing

The performance of UAV 1 and UAV 2 has been assessed in the spoofing scenario, and results are reported in Figure 6.8 and Figure 6.9 for the two UAVs respectively, for the entire experiment period.

It can be seen that starting from the 3rd minute, the spoofing signal started to affect the UAV 2 followed by a sudden change to the spoofed location. However, UAV 1 shows more resistance to the spoofing signals but still slightly drifting to the spoofed location in the end. Furthermore, after the 8th minute, even though the spoofer was switched off and only the clean simulated signal was transmitted, the coordinates of both UAV 1 and UAV 2 were still affected. This impact of the spoofed estimations continues because the previous erroneous estimation of the

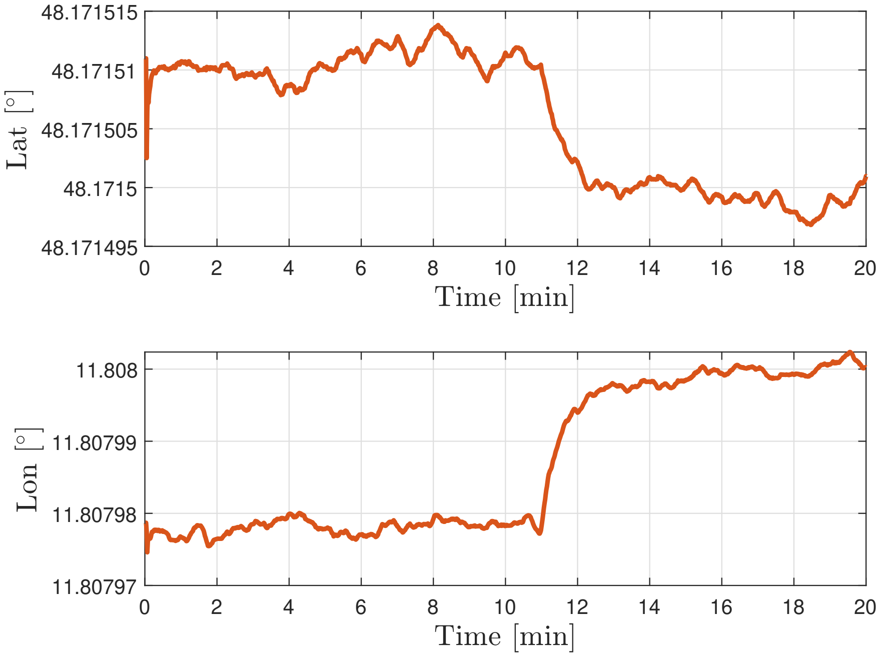

Figure 6.6: Estimated position by IMU unit from UAV 1 under jamming

UAV status propagates in the possible Kalman filter (KF) of the Autopilots. The test scenario indicates that although the two drones have different resistance to the spoofing signal, they can still be easily spoofed.

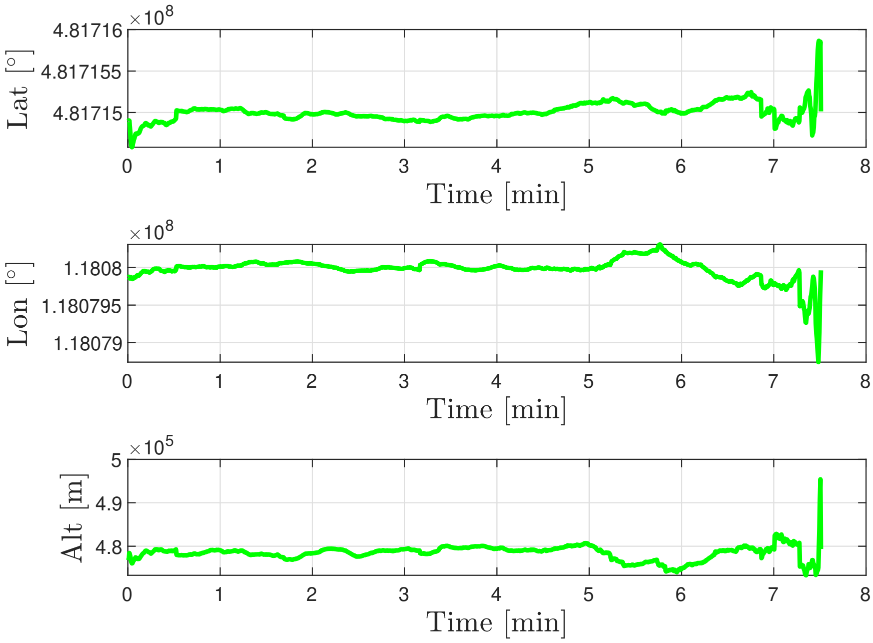

Figure 6.7: Estimated position by GPS unit from UAV 2, no data are avilable after 8th minute.

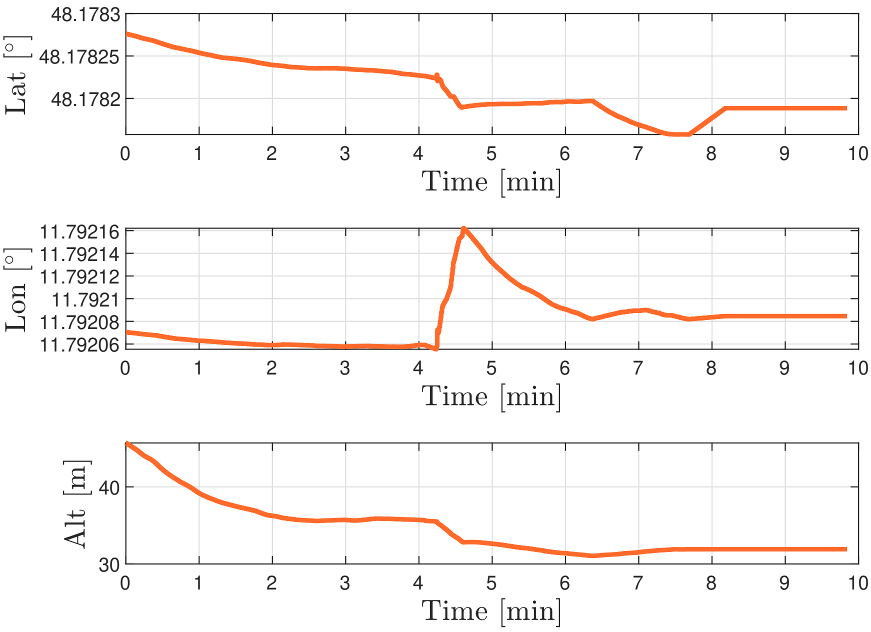

Figure 6.8: Estimated position by GPS unit from UAV 1 under spoofing

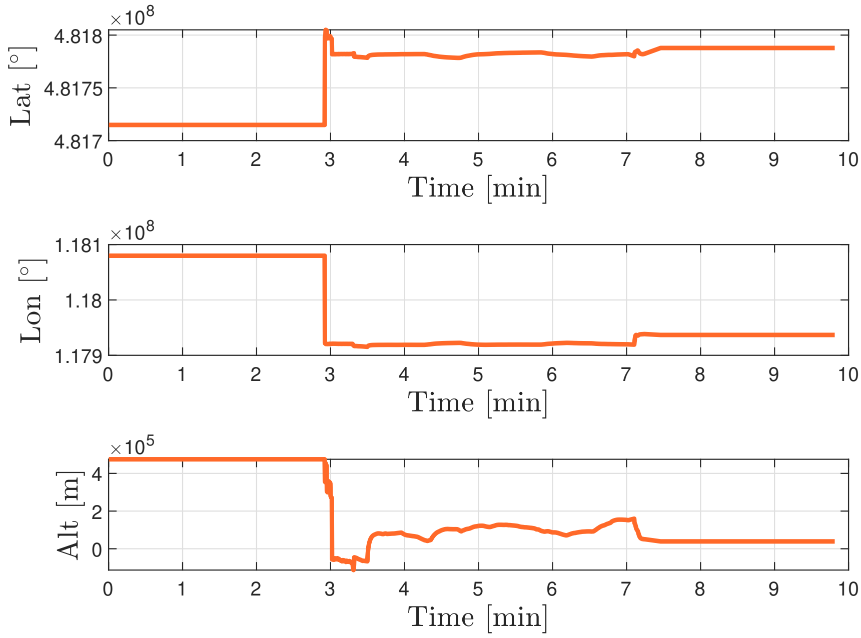

Figure 6.9: Estimated position by GPS unit from UAV 2 under spoofing.

6.2 Spoofing Effects on Raw GNSS measurements

A comparative analysis of the resilience of Android™ domain to intentional disturbances is performed in this section. The experimental work presented hereafter provides one of the first investigations on the use of a portable spoofer to threaten Android™ smartphones. The portable low-cost spoofer has been developed, based on open source signal generator and low-cost electronics and radio-frequency equipment and then used to carry out spoofing attacks on different Android™ smartphones [40].

Some demonstrations of spoofing against Google Android™ OS are presented in [134] with realistic spoofing and fake Google Maps™ integration. This work demonstrated that spoofing might impact the device's navigation unit affecting in turn a popular Location Based Service (LBS). Since the version 7 onwards of Android™ OS gives access to raw GNSS measurements, it can be exploited to study and detect the effect of spoofed signals in applicable smartphones. The raw GNSS measurements may include internal clock measurements like the time of signal reception, clock drift, clock discontinuities, etc. and the GNSS receiver measurements such as received GNSS satellite time, Doppler frequency, carrier phase measurements, constellation status, navigation messages, etc. [113] . More recently, the Google Service Framework™ also provides Automatic Gain Control (AGC) measurements in its Android™ location modules with the release of Android™ Android Application Program Interface (API) 9.0. However, not all the GNSS chipsets or software of the different Android™ devices are compatible with such measurements and the quality of the raw GNSS measurements vary between device to device [36, 135].

6.2.1 Test Devices

Following the direction of testing the chosen simplistic portable spoofing methodology on consumer GNSS devices, three different commercial smartphones were chosen among those equipped with Google Android™ 8 Operating System (OS). These are detailed in Table 6.1 and are referred to as S1, S2 and S3 respectively in the following analysis. In order to identify and procure GNSS raw measurements, the GNSS Logger Android application provided by Google™ was installed in the android devices. The devices PVT solutions were logged through the Android application NMEA tools, which provides the GNSS raw position of the smartphone in standard NMEA format. Figure 6.10 shows the set-up of different Android™ devices and the transmitting antenna of the developed spoofer. Additionally, a commercial GNSS receiver was also used as a benchmark for data collection and PVT estimation.

The raw GNSS measurements of the smartphones were processed on the MATLAB®®

Table 6.1: Devices under test.

ID	Model	System on cheap (SOC)	GNSS chipset
S1	S 8	Qualcomm Exynos 8890	BCM 4774
S2	MI 8	Qualcomm Snapdragon 845	BCM 47755
S3	MI 8 PRO	Qualcomm Snapdragon 845	BCM 47755

GPS measurement-tools software[1] [106]. For the purpose of this paper, the following raw measurements are mainly analysed to test the effects of spoofing:

Carrier-to-Noise Density Ratio (C/N_0) : It is a basic indicator of received satellite signal quality. Abrupt variations to it can indicate the presence of interference while an unnaturally high value could also indicate presence of a fake satellite signal.

Automatic Gain Control (AGC) : The AGC implementation in a smartphone acts as a variable gain amplifier adjusting the power of the incoming signal. Changes in the value are typically indicative of power fluctuations of the input signal in the frequency band foreseen this measurement [113]. AGC is extremely useful in detecting spoofing attacks and has been used in the past to detect defective signals [92].

Time of Signal Transmission and Reception : The GPS Time of signal Transmission, t_{TX}, is demodulated from the received signal and used to compute the pseudorange from the particular satellite along with The Time of signal Reception, t_{RX}, which is taken either from the cellular or Wi-Fi network in the smartphone. A remarkable difference in the two timestamps could indicate an altered t_{TX} data coming from a spoofed signal or a faulty satellite. Generally, it is in the range of $60 - 100$ ms.

6.2.2 Spoofing Scenario

A 15-minutes spoofing scenario was tested in a controlled outdoor environment with open sky conditions. By acting on the HackRF One transmitting power, the range of the spoofer antenna was kept to within 1-3 m to not provide any disturbance beyond the range of the controlled environment. The smartphones were positioned at a location with coordinates 45.064406 N, 7.661922 E (Turin, Italy) starting UTC time of February 11, 2020, 14.21.41 and for the first 5 minutes,

[1] Apache Licence 2.0 (http://www.apache.org/licenses/LICENSE-2.0)

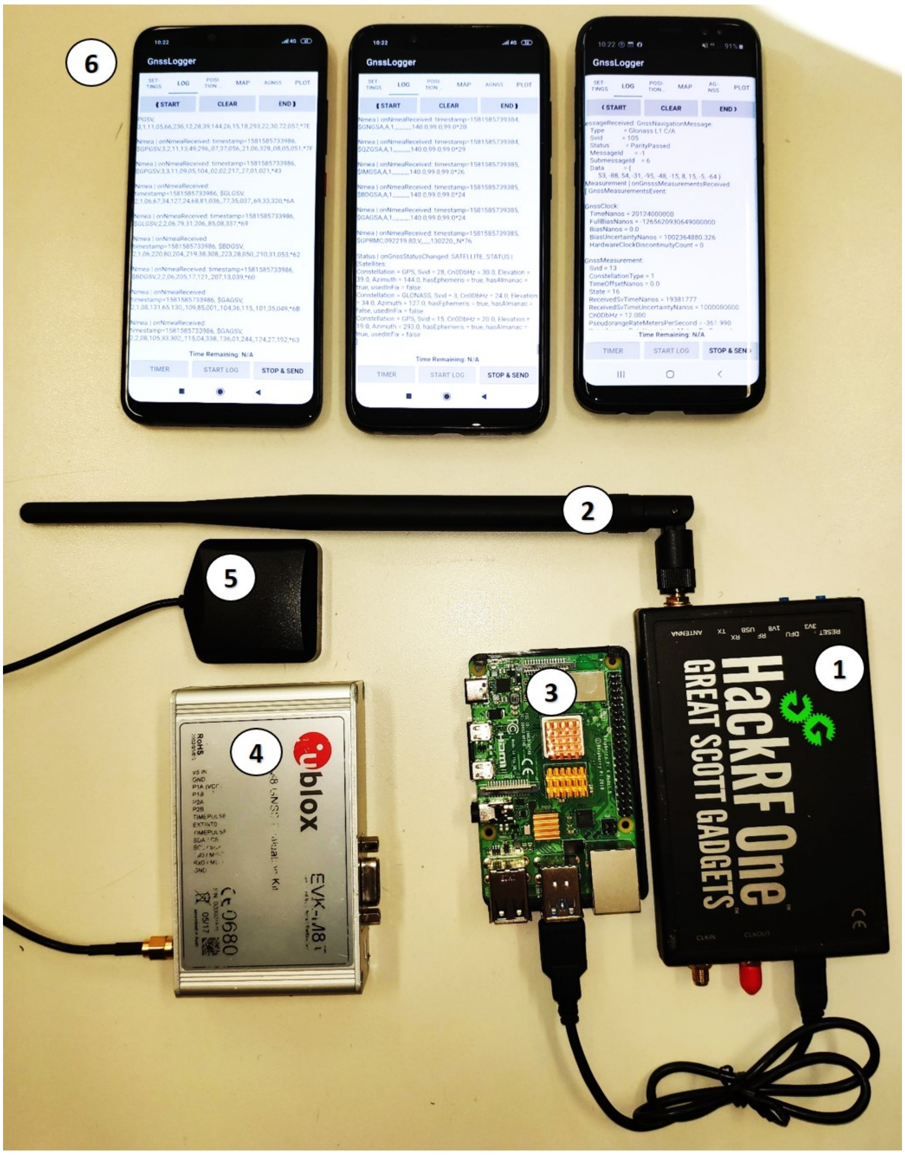

Figure 6.10: Experimental setup consisting of a HackRF One, (1) equipped with an L1 stick antenna, (2), a Raspberry PI 4B, (3) a u-blox™ Neo-M8N GNSS, (4) with an active GNSS antenna, (5) and a set of smartphones, (6) listed in Table 6.1.

they received live GNSS signals without any other interference. Then the portable spoofer was switched on, broadcasting spoofing signals over GPS L1 band with coordinates 45.470111 N, 9.179874 E (Milan, Italy) and UTC time February 10, 2020, 12.00.00 which was 144 km away from the test location. The spoofing signals were broadcasted for 5 minutes after which the spoofer was switched off. For the remaining duration, the smartphones received only live GNSS signals. The u-blox™ Neo-M8N GNSS receiver was used for cross validation of the test measurements.

Table 6.2: Satellite Subsets

Subset	SV ID Number
Real	24,25,28,19,17,15,13,12
Fake	8,16,27
Common	10,20,32

14 GPS satellites were considered in the overall scenario. As seen in Table 6.2, the satellites could be divided into three different subsets. The first subset (Real) consists of the real in-view Satellite Vehicle Identifiers (SV IDs) which were received by each device and not part of the satellites transmitted by the spoofer. The second subset (Fake) consists of the SV IDs which were transmitted by the spoofer and visible to all the smartphones, but their real counterparts were not in view during the test period [8, 16, 27]. The third subset (Common) consists of the overlapping Satellite Vehicle (SV) IDs which were both in-view real time and transmitted by the spoofer as well [10, 20, 32]. The overall satellite skyplot during the test is shown in Figure 6.11.

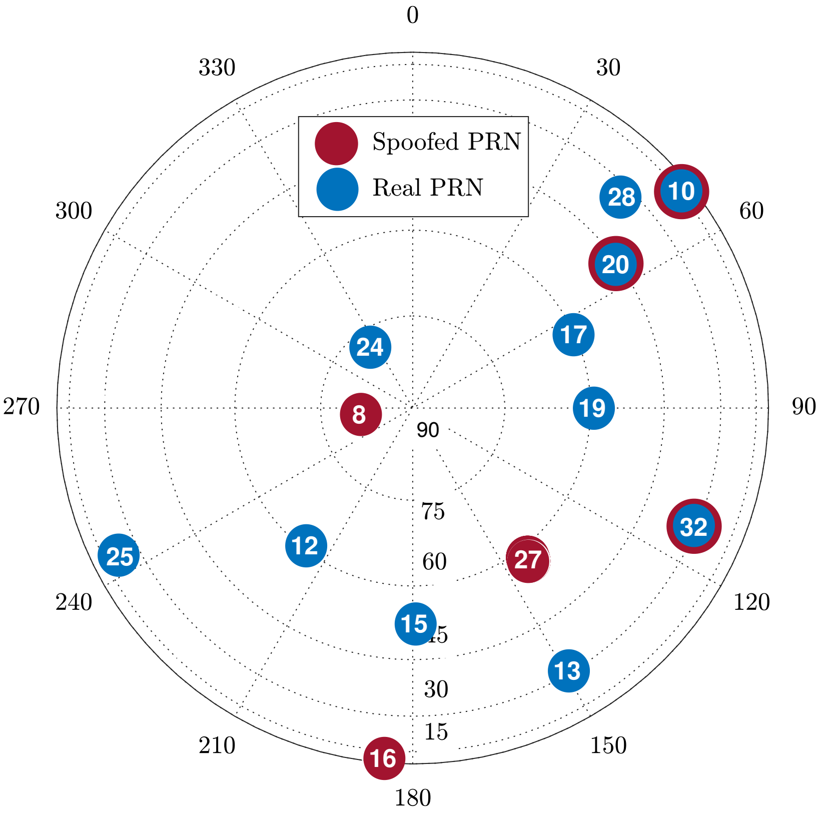

Figure 6.11: Sky-plot showing real and spoofed satellite signals.

6.2.3 Results and Analysis

The subsection is roughly divided based on the effect of the spoofing described in Section 6.2.2 on GPS L1 GNSS raw measurements of the three different subset of satellites. The data analysed is from smartphone S3 but similar results were also achieved with S2. GNSS raw measurement could not be retrieved from S1 after the spoofer was turned on. The effect on position computation of the smartphone as retrieved from the Android location API was also analyzed, as reported in the following. The u-blox™ Neo-M8N receiver position shifted to the coordinates provided by the spoofer within 1 minute from the start of the spoofing action, thus, validating the effectiveness of the attack.

Effect on Real satellites

Figure 6.12 compares the C/N_0 and pseudoranges of two real SV IDs during the entire test period with SV ID 24 and 25 being at high and low elevations respectively. Naturally this will affect their signal strength and pseudorange distance as seen in the Figure 6.11. It is clear that the spoofer acts as a source of interference over the L1 frequency band disturbing the healthy satellites during the spoofing timespan and tracking of low elevation satellites being lost. This effect is seen for the L1 signals of constellations as well.

Fake and Real satellites comparison

Figure 6.13 plots the AGC dB values of the S3 GNSS receiver during the test period. It is observed that the effect of turning on the spoofer is similar to what in-band jamming or interference would do. Due to the presence of powerful spoofing signals, the receiver reduces the amplification of the incoming sign which, while disturbing real signals, allows fake signals to be easily acquired. This is clear when comparing the C/N_0 of a fake (SV ID 16) and real signal (SV ID 24) in Figure 6.14. An important difference captured between the two satellite signals is the t_{TX}, whose values in a real signal was within the standard 100 ms of the t_{RX} throughout the test, while fake signals had t_{TX} and t_{RX} difference values over 10^5 seconds. This naturally gives a hugely and unrealistic pseudorange value for the fake satellite. Nevertheless, it has to be remarked that no effect is experienced on the time provided, since the connected device is kept synchronised to the communication network infrastructure (cellular or Wi-FI).

Effect on Common satellites

Figure 6.15 plots the effect of spoofing on the C/N_0, Pseudorange and Carrier phase measurements of a Common satellite (SV ID 10) present among the live satellites and in the set of spoofed signals. It can be seen that the receiver does not

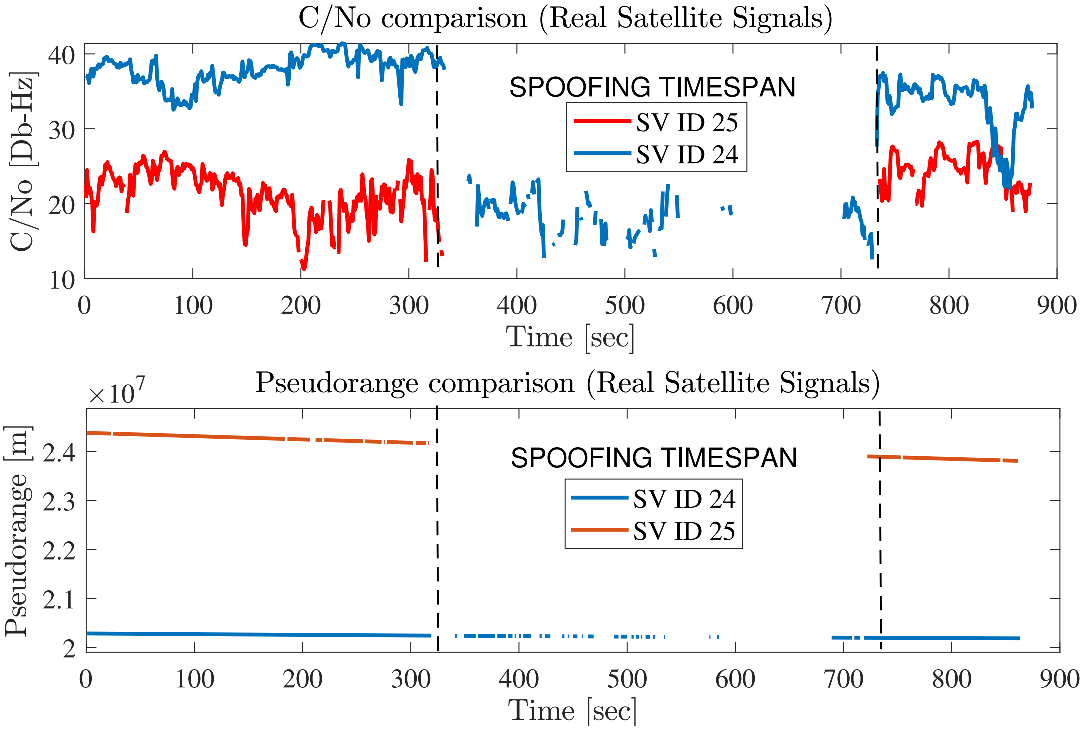

Figure 6.12: Effect on real satellites (SV ID 24 and 25) during the test duration.

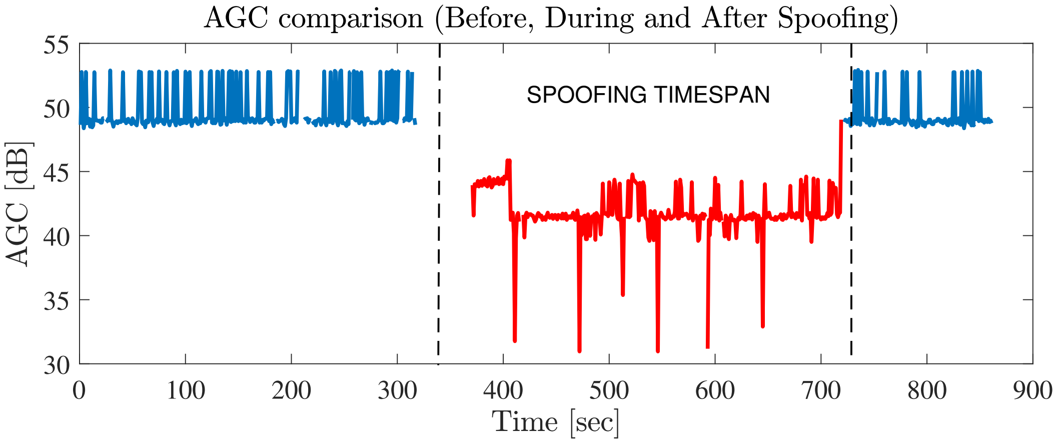

Figure 6.13: Effect of Spoofing on AGC.

acquire the fake satellite signal with the same SV ID during the spoofing timespan and only looses acquisition of the real signal. It reacquires the real satellite after spoofing stops as also seen by the carrier phase measurement.

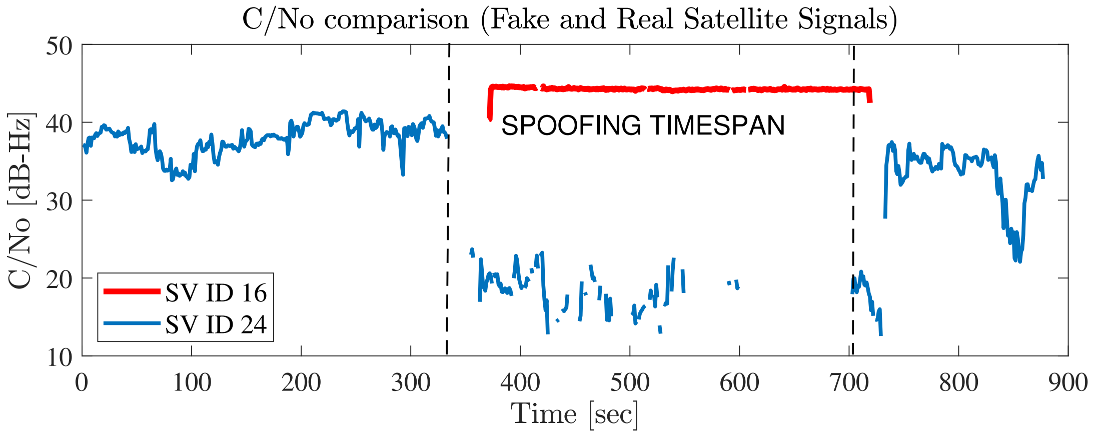

Figure 6.14: Comparison of Fake (SV ID 16) and Real (SV ID 24) satellite's C/N_0
.

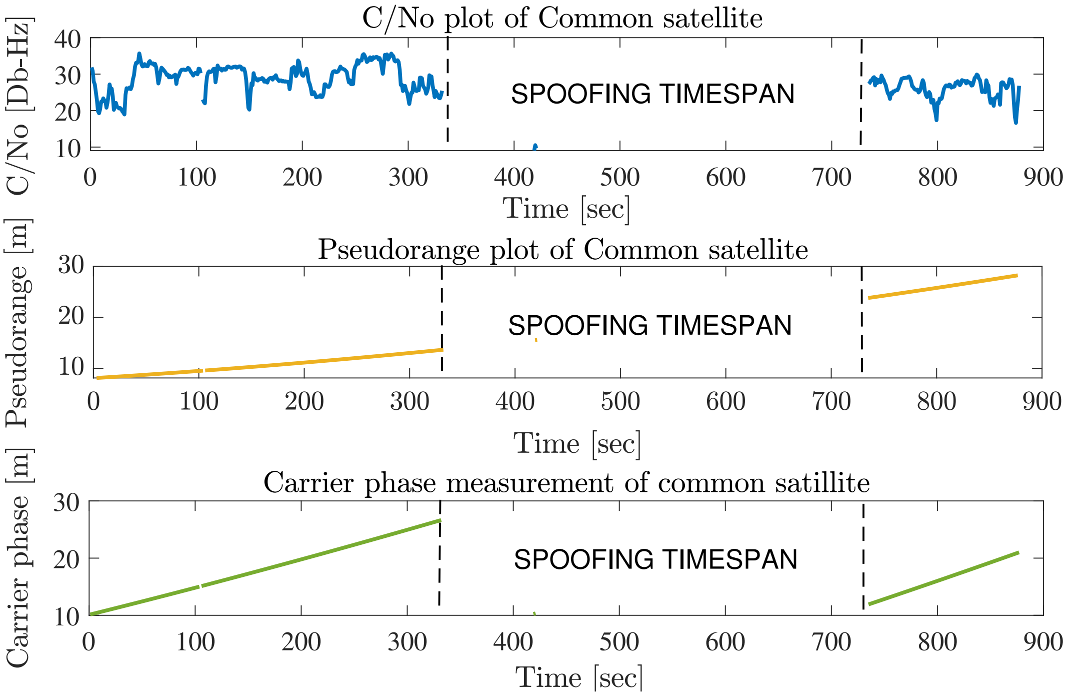

Figure 6.15: Common Satellite (SV ID 10) analysis.

Effect on Smartphone GNSS Position Estimation

Figure 6.16 shows the error in position of the ECEF coordinates of the three different smartphones during the test. The spoofing time span is delayed compared to the previous plots as NMEA Tools app was initialised before GNSS Logger app. It can be seen that spoofing achieves only a few metres of deviation in the position output of the GNSS receiver which can be attributed to the loss of some satellites due to interference. It can be speculated that the smartphones maintain their true position with the help of multi-constellation, multi-frequency GNSS capabilities along with network positioning and other sensors. It is interesting to notice that S1 carries the Broadcom™ BCM 4774 chipset without dual frequency GNSS capabilities and it is affected the most, comparatively.

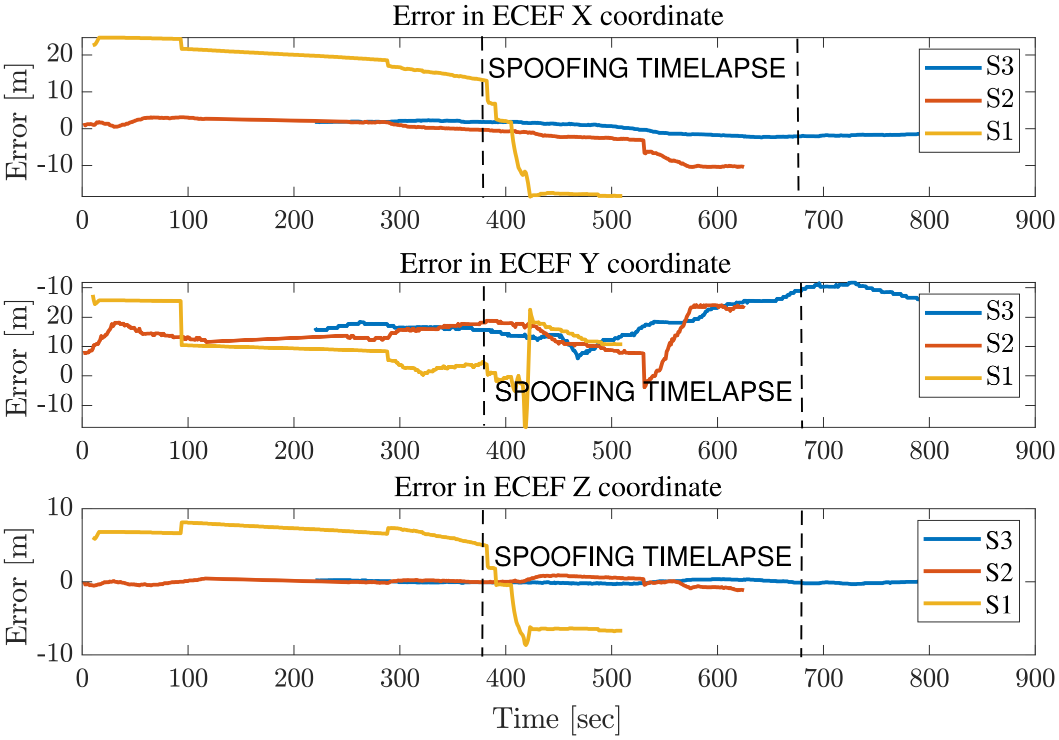

Figure 6.16: Effect on Smartphone GNSS Position.

6.3 Cooperative Positioning as an Interference Defence

6.3.1 Background and Scenarios

CP framework can encapsulate additional monitoring to avoid current and next-gen-type attacks to the positioning and navigation units. The work presented in [38] opened the investigation to the DGNSS-CP based on the inter-device range from GNSS raw measurements between two Android devices within a communication framework. The availability of cooperative algorithms applied to the GNSS pushed researchers to design new framework to cope for the limitations of traditional PNT approaches. The DGNSS-CP framework investigated in this work ideally supports the exchange of raw GNSS measurements among multiple receivers interconnected by 4G LTE or Wi-Fi connectivity executed through an Android application. The measurements are hence synchronized through a Doppler compensation technique [98] and the inter-agent distance is computed through a differential GNSS approach [136].

The DGNSS-CP framework presented by the authors acts according to the following steps for each PVT epoch, t_k

1. Agent **A** sends to **T** its set of raw pseudorange measurements $\boldsymbol{\rho}_A(t_k)$ and the estimated position $\hat{\mathbf{x}}_A(t_k)$ with an associated timestamp t_k

2. Agent **A** aligns the external set of measurements retrived from **T** $\boldsymbol{\rho}_A(t_k)$, to the closest set of measurements locally dumped.

3. Agent **A** combines the local and external pseudorange measurements through differential method to determine the inter-agent distance between **A** and **T**

4. Agent **A** integrates such **A**-**T** inter-agent distance w.r.t. the position of **T** (consistent) along with local pseudorange measurements within its navigation algorithm (i.e. Extended Kalman Filter (EKF))

5. The position estimation of **A** is generally improved by the additional information carried by the set of pseudorange measurements shared by other receivers and it is not expected to show any particular drift [119].

Technical details concerning the implementation of the framework can be found in [121, 82, 116] and a proof-of-concept applied to Android smartphones was developed within the ESA project HANSEL.

The aforementioned DGNSS-CP framework is prone to be fooled by malicious attacks at different stages of the GNSS processing chain

- **Signal domain**: performed through the transmission of RF signals. This approach induces the tracking of the fake signals to an aiding receivers, thus the computation of fake pseudorange measurements, and in turn, of a fooled PVT estimation of both aiding and aided receivers. A scheme of the attack is provided in Figure 6.17.

- **Measurements domain** This approach acts by replacing the measurements transferred to the server of a CP client-server architecture, as in Figure 6.17, or performing a man-in-the-middle attack, to ideally perform a "virtual" spoofing/meaconing attack as shown in Figure 6.17.

An attack pursued in any of this domains induces similar effects on the final positioning estimation but a proper distinction is worth to distinguish the typology of attack between *classical spoofing/meaconing* and *cyber-attack*. The latter are indeed less related to the receiver architecture and mostly focused on the system/network. With the control over sharing of specific information between the devices and availability of synchronization strategy, some strategies will be proposed to detect the presence of spoofing in one or multiple networked GNSS receivers devices. Therefore, the possibility to imprint such an algorithm to COTS GNSS receivers on other networked operating platforms can open several possibilities oriented to spoofing attacks such as in networked Unmanned Aerial Vehicles (UAVs) and Unmanned Ground Vehicles (UGVs).

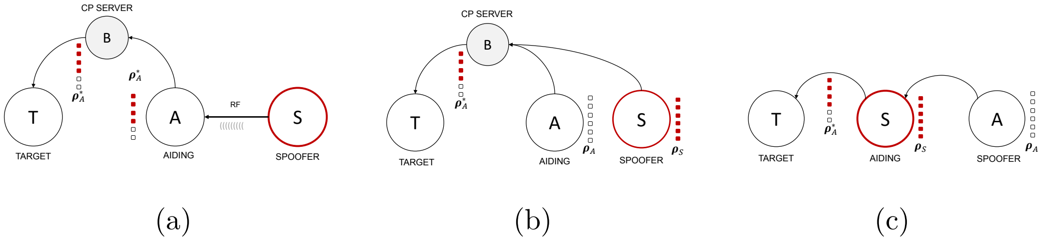

(a) (b) (c)

Figure 6.17: Schemes of possible attacks performed through a GNSS-based CP framework. Filled squares represent fake measurements provided by S while white squares are nominal measurements provided by A.

6.3.2 Experimental Tests

The following scenarios were defined to investigate potential countermeasures to the malicious attacks against GNSS.

Scenarios 1: Test on static Android Smartphones

For the primary test, two different commercial smartphones (with Broadcom® BCM47755 GNSS chipsets) were chosen for testing the effect of a simplistic spoofing attack performed through the portable spoofer on consumer GNSS receivers. Both of the devices, denoted as S1 and S2 respectively further in this work are equipped with Google Android™ 9 Operating System (OS) and the GNSS Logger Android application provided by Google™ was installed in them for identification and procurement of GNSS raw measurements. A 800 seconds spoofing scenario was tested in a controlled outdoor environment with open sky conditions. During the test, the devices were located at a distance of 10 meters apart, where S1 was places next to the spoofer to explore the effect of interference and S2 was kept 10 meters away to avoid the risk of spoofing under open sky conditions. The range of the spoofer was kept to around 2 meters and in order to prevent any radio-frequency interference (RFI) disturbances beyond the range of the controlled environment a 10 dB attenuator was used and inserted to the coaxial cable to reduce transmitting signal power levels. Both smartphones actual locations were around the coordinates 45.06 N, 7.66 E (Turin, Italy). During the first 120 seconds of the test, both devices received live GNSS signals without any other interference. Then the portable spoofer was switched on, broadcasting spoofing signals over GPS L1 band with coordinates 45.755664 N, 4.831035 E (Lione, France) with S1 in its range. The spoofing signals were broadcasted for 500 seconds after which the spoofer was switched off. For the remaining duration, both devices received only live GNSS signals.

In general, 16 GPS satellites were considered during the test. The satellites could be divided into three different group. The first subgroup (Real) consists of real-time Satellite Vehicle Identifiers (SV IDs) received by each device and not part of the satellites transmitted by the spoofer. The second subgroup (Fake) consists of SV IDs that were broadcasted by the spoofer and available to all smartphones, but their real equivalents were not displayed during the test [15, 19, 24]. The third subgroup (Common) consists of concurrent Satellite Vehicle (SV) IDs which were both in-view in real time and transmitted by the spoofer [10, 14, 32].

Scenarios 2: Simulated meaconing attack in multi-agent vehicular scenario

This section presents a preliminary investigation of a simulated meaconing attack affecting one agent being part of a multi-agent network. The meaconing aims at forcing the computation of the inter-agent distance (a.k.a. baseline length) by using fake pseudorange measurements provided by a spoofer chosen among the available agents. The simplistic scenario is composed of 3 agents within a multi-agent network:

- The target (**T**) (the kinematic agent which is expected to benefit from cooperation)
- The aiding agent **A** (a further kinematic agent providing pseudorange measurements)
- The spoofer (**S**) (an agent generating pseudorange measurements related to its own position but to be used to fake the contribution of **A** to **T**).

According to the nominal steps recalled about the cooperative framework in Section 6.3.1, the following considerations about this specific attack hold if **S** overwrites the pseudorange measurements transmitted by **T** but not its reference position. Formally

- Agent **A** simply receives a packet composed by the position of **T** and the measurements of **S**
- Agent **A** aligns the external set of measurements of **S** to the closest (in time) set of measurements dumped locally
- Agent **A** combines the local and external pseudorange measurements through some differential method (i.e. DD) to determine the inter-agent distance between **A** and **S**
- Agent **A** integrates this inter-agent distance A-**S** w.r.t. the position of **T** (inconsistent) along with local pseudorange measurements within its navigation algorithm
- The position estimation of **A** is "generally degraded" by the additional information and it diverges from the standalone GNSS solution

6.3.3 Results and Analysis

After presenting a validation of the spoofing scenario at Section 6.3.2, the results and analysis section is roughly split into following parts. The first part, Sections 6.3.3 and 6.3.4 deals with the comparison of GNSS raw measurements between the two connected and synchronized devices in order to build up an effective anti-spoofing strategy. The second part, Section 6.3.4 firstly presents the results of a meaconing test on the CP framework chosen for this work and then the advances to the framework which could be made to identify spoofing attacks.

Validation of Spoofing Attack

The u-blox™ Neo-M8N GNSS receiver was used for cross validation of the test measurements during the primary test. Figure 6.18 shows the change in geodetic coordinates of the u-blox GNSS receiver during the test . It can be seen that the receiver has no defence against the simplistic spoofing attack with the latitude, longitude and altitude changing to that of the spoofed coordinates hence validating the spoofing mechanism employed on a regular COTS device.

In another tertiary test replicating the same spoofing attack methodology on S1, S2 and an added smartphone S3, it was seen that the positions of the smartphones were not spoofed by the spoofer broadcasted signals. It has to be noted that the equipment and RF spoofing signal is identical in this test and could not be carried out along with the main tests due to logging problems of NMEA and GNSS raw measurements data simultaneously.There was a slight meter of deviation in the positions during the spoofing period, displayed on the left of Figure 6.19 which shows the variation in the Earth-Centered Earth-Fixed (ECEF) Z coordinate from the reference chosen, as an example. These few metres of deviation in the position

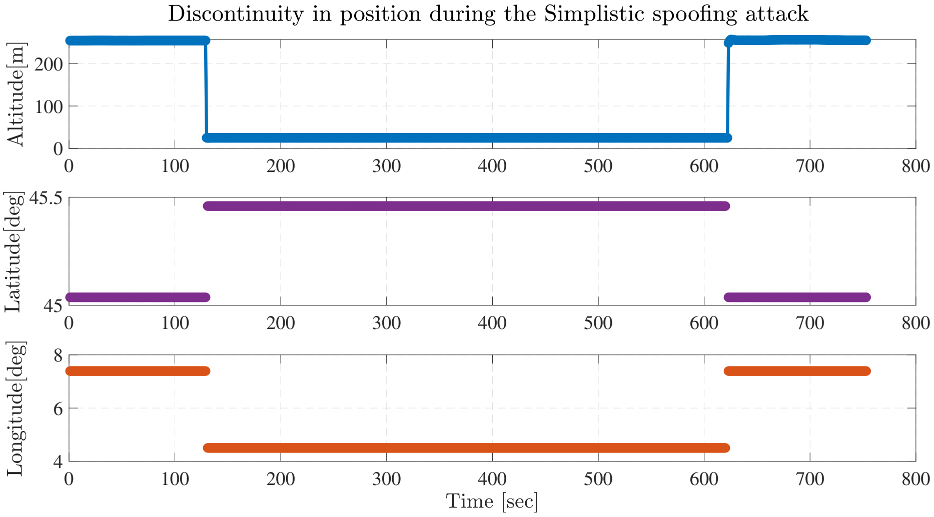

Figure 6.18: Effect of spoofing interference on u-blox™ Neo-M8N receiver.

output of the Android devices can be attributed to the loss of some satellites due to interference as will be seen later and it can be roughly visualized on the right of the Figure 6.19 which shows number of satellites acquired during the time period. The vertical doted line in the figure corresponds to the start of the spoofing period. It can be speculated that the smartphones maintain their true position with the help of multi-constellation, multi-frequency GNSS capabilities along with network positioning and other sensors. It is also interesting to notice that S3 carries the Broadcom™ BCM 4774 chipset without dual frequency GNSS capabilities and it is affected the most, comparatively. This is seen to be due to the spoofing signals acting as an interference on the L1 band, hence hampering reception of low-quality signals. The smartphones hence inherently have a robustness to such simplistic spoofing attacks due to it being an accumulation of multiple sensors, connected networks and complicated positioning algorithms. This however does not mean that the spoofed signals aren't acquired, but only that the PVT computation of Android location API ignores the spoofed signal measurements. With a multitude of Android applications being developed in recent times utilizing GNSS raw measurements directly, the simplistically spoofed signals being acquired and tracked in Android devices pose a significant threat. Therefore, an analysis of the acquired Android Raw GNSS Measurements of smartphones under and without a spoofing attack simultaneously follows.

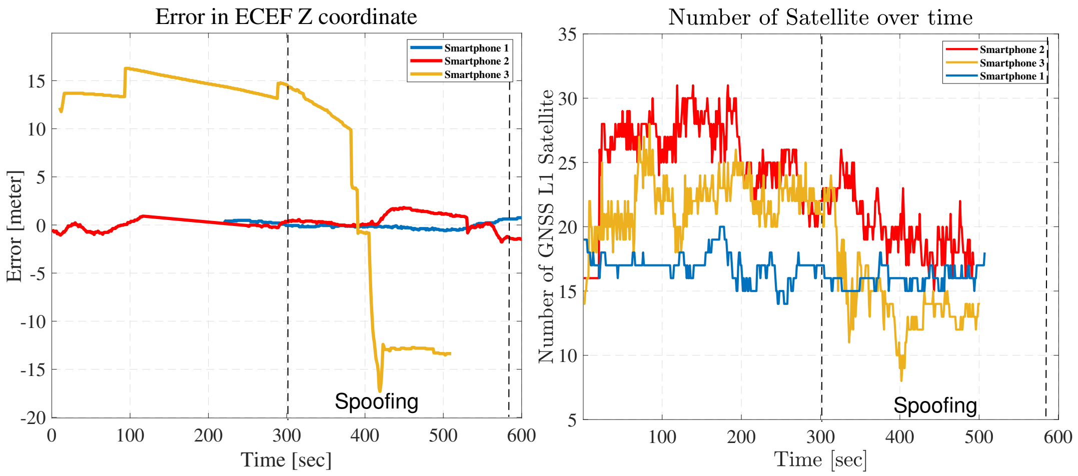

Figure 6.19: Effect of spoofing on: a) Earth-Centered Earth-Fixed (ECEF) Z coordinate (left) and b) GNSS L1 satellite availability in Android smartphones (right).

6.3.4 Analysis of Android Raw GNSS Measurements of the two devices

Time and Ephemeris considerations: In Android Smartphones, the GNSS time of signal transmission of each satellite is demodulated from the received signal and presented as a raw measurement used to compute the pseudorange for that particular satellite along with the time of signal reception. However, the latter is taken either from the cellular or Wi-Fi network in the smartphone and hence it has not been possible to affect the reception time with GNSS spoofed signals. Considering the clock biases, since the general difference between the two time stamps falls in the range of 60 - 100 ms, a remarkable difference in the two timestamps could directly indicate the possibility of a spoofed signal. To generate real time spoofed signals consistent with GNSS time, the scope of the work goes beyond simplistic spoofing. A few of the current Android GNSS devices also support demodulation of the GPS navigation message and present them as a string of numbers to be converted into a binary form. Processing this message for the two different phones showed a clear distinction between satellites of the different subgroups in terms of GPS Time of Week (TOW) and this can be an alternate check to time inconsistency between two devices to detect a simplistic spoofing attack. The resistance of the spoofed device to not acquire the Common subgroup of spoofed satellites as presented in [40] meant however that the same satellite ID could not be compared between two devices at the same time where one device tracks the spoofed satellite and the other tracks the real one. Further, the limitation of most commercial Android phones to not provide the navigation message and the inability to provide navigation messages of other constellations makes this approach very narrow and situational.

C/N_0 and AGC comparisons: Figure 6.20 compares the S1 (under spoofing attack) and S2 (without spoofing attack) GNSS receiver C/N_0 values of various SV IDs during the spoofing test duration. The SV IDs are represented by their PRN numbers on the plot. On the left side of the figure, looking at the C/N_0 time trend of the Real and Common subset of satellites over time (SV ID), it can be seen that it is affected drastically during the spoofing period between 120-620 seconds. It is clear that the spoofer acts as a source of interference over the L1 frequency band disturbing healthy satellites during the spoofing time span with tracking of low elevation satellites being lost at times (PRN 27). This effect is seen for the L1 signals of other constellations as well. The Fake subgroup of satellites appear as expected when the spoofing starts and has a consistent high C/N_0 value corresponding to the static nature of both the spoofer and the Android device. In contrast, the right side of the figure presents the normal behavior of C/N_0 values in the Android device under no spoofing attack. This introduction of noise by the spoofer results in the disturbance of the PVT solution of the GNSS receiver in the device, as seen in the test of Figure 6.19 regardless of the spoofed satellites not being included in the solution computation. Figure 6.21 plots the AGC amplification/attenuation value (in dB) of the S1 (left) and S2 (right) devices during the test period. It is observed that the effect of turning on the spoofer is similar to what in-band jamming or interference would do. Due to the presence of powerful spoofing signals, the receiver reduces the amplification of the incoming sign which, while disturbing real signals, allows fake signals to be easily acquired. This is clear when comparing the S1 and S2 of a fake and real signal.

AGC to C/N_0 Ratio: In [137] [138] analyzed correlation between various metrics such as power monitoring, multiple-correlation tap, maximum-likelihood multipath estimator for distinguishing GNSS spoofing, jamming or multipath effects. To build towards a simpler anti-spoofing strategy an attempt is made to narrow the dimension of GNSS raw observations. For AGC, depending on the front-end quantization of a receiver it affects the C/N_0 with different sensitivities [92] and COTS receivers generally have lower bit quantizations. Hence building on the correlation, a parameter equating to the AGC to C/N_0 ratio of its absolute values is observed. Across different Android smartphones, slightly different levels of AGC and C/N_0 are observed depending on the front-end and digital signal processing blocks on similar test conditions. Hence this parameter standardizes the power of a signal at the receiver to an extent taking into account the only variable available in Android devices currently to consider the front-end stage. Identifying the AGC to C/N_0 response of the receiver's front-end to RFI events, we could be able to draw a threshold that will allow us to discriminate between jamming events

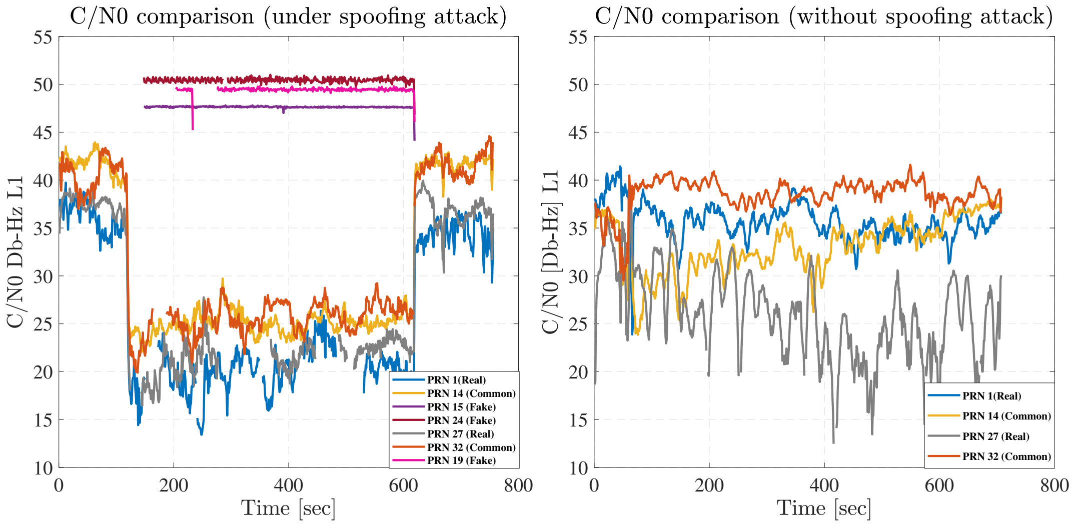

Figure 6.20: Effect spoofing on Signal-to-noise ratios with (left) and without (right) spoofing during the test duration.

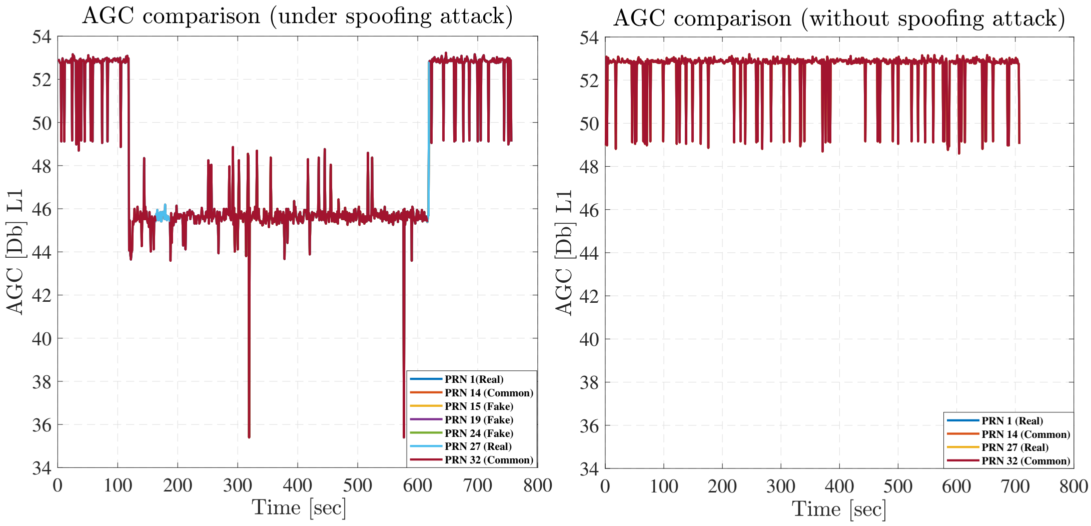

Figure 6.21: Effect spoofing on *AGC* with (left) and without (right) spoofing during the test duration.

and spoofing attacks. While spoofing attack lead to a drop of the *AGC* when they appear within the band, the way they are generated are different because of their respective nature. For a non-intentional RFI attack, the signal is not consistent with the satellite and noise is added to the targeted GPS band, which leads to a drop of the C/N_0 of the tracked signal. Conversely, during a spoofing attack the signal is generated to look like a GPS signal. Thus, it increases the power of the carrier signal and so, it leads to a raise of the C/N_0 value. Figure 6.22 displays this ratio parameter in the phones S1 and S2 on the left and right respectively. The nature of this parameter can be seen to be similar during periods of non interference in both devices and upon the spoofing period, there is a stark contrast between spoofed and non spoofed PRNs. The parameter is put to test for different test datasets as well considering jamming and multipath conditions (on the left and right respectively) in Figure 6.23. A threshold considering either the direct value or its change with respect to time between different PRNs is to be presented as future work. Considerations will have to be made for utlizing a wider range of Android devices as well as interference power levels.

There are further metrics to be explored as well which will be presented in future works. For example, GNSS signal authenticity verification technique using carrier phase double differences as presented in [139] was considered but due to poor quality of results and limitation to experiment datasets, it could not be presented in this paper.

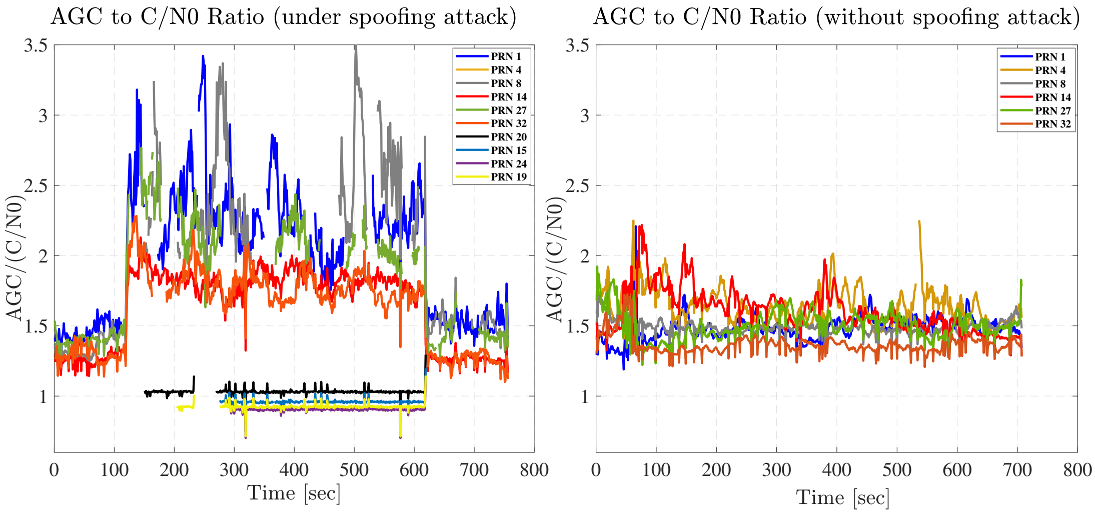

Figure 6.22: *AGC* to C/N_0 ratio values with (left) and without (right) spoofing during the test.

Spoofing Attacks in a Cooperative Positioning Framework

Meaconing attack in multi-agent vehicular scenario: Spoofing Attacks in a CP Framework are referred to the spoofing scenario of Figures 6.17b and 6.17c discussed in Section 6.3.1. This test is presented to highlight the potential effects of a meaconing attack and to propose potential countermeasures against this novel threats to positioning and navigation for next-gen networked receivers. A realistic simulation over a Bernoullian trajectory was performed through a MATLAB Software receiver named NavSAS SWRx on top of IFEN-generated signals. We

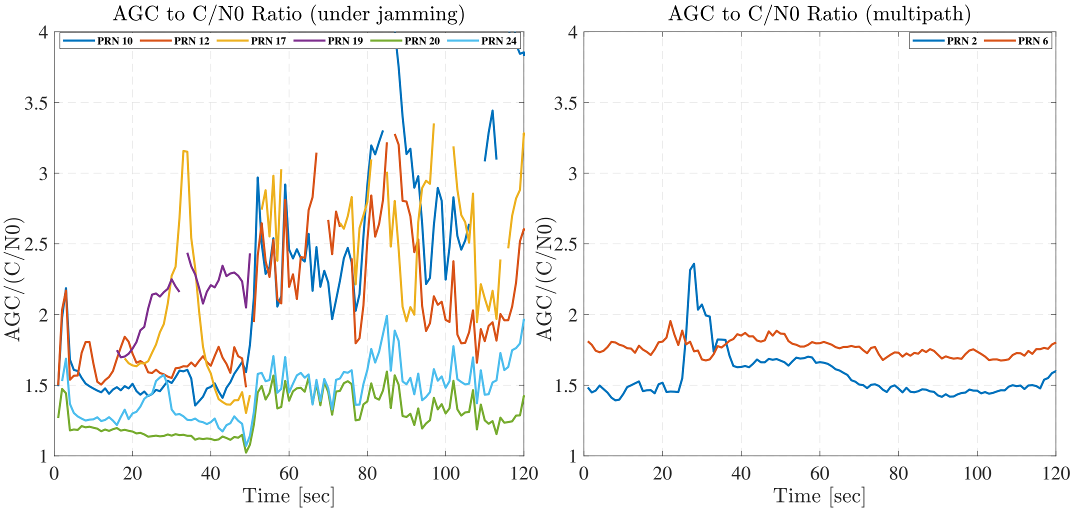

Figure 6.23: Effect of different RFIs: a) jamming effect (left) and b) multipath (right) in Android smartphones.

can see that cooperative positioning of the meaconed solution, in Figure 6.24b is remarkably altered w.r.t. the GNSS standalone estimation, in Figure 6.24a. It is worth noticing that the trajectory shape is roughly preserved when measurements are faked and additional measurements from exteroceptive or proprioceptive sensors are required to inform the user that a different trajectory is followed. By comparing GNSS standalone and cooperative solutions, the receiver of agent **A** can detect an anomaly in the navigation solution because the the collaborative PVT diverges w.r.t. to the GNSS standalone estimation, still preserving a considerable precision. The navigation system cannot trust the cooperative submodules and it can inhibit the use of auxiliary measurements.

In order to design robust CP algorithm using ranging measurements the target **T** (or the server, if a client-server architecture is considered) has first to assess the consistency of reference position and pseudorange measurements to exclude the contribution of Agent T (which is faked by S) and inhibit the **A**-**T** cooperation which could limit the reliability of the solution.

Attack and detection through collaborative measurements combination: An advanced detection method can be designed by looking through the processing chain of the collaborative measurements to look at the effect of combining a set of locally-estimated pseudorange with a set of "spoofed" measurements retrieved from a further receiver. In this case only inter-agent distances between the two receivers are computed by relying on their pseudorange measurements, thus the effects of attack on the positioning solution are not discussed. It is worth stressing that in the current CP framework, receivers cooperate at measurements

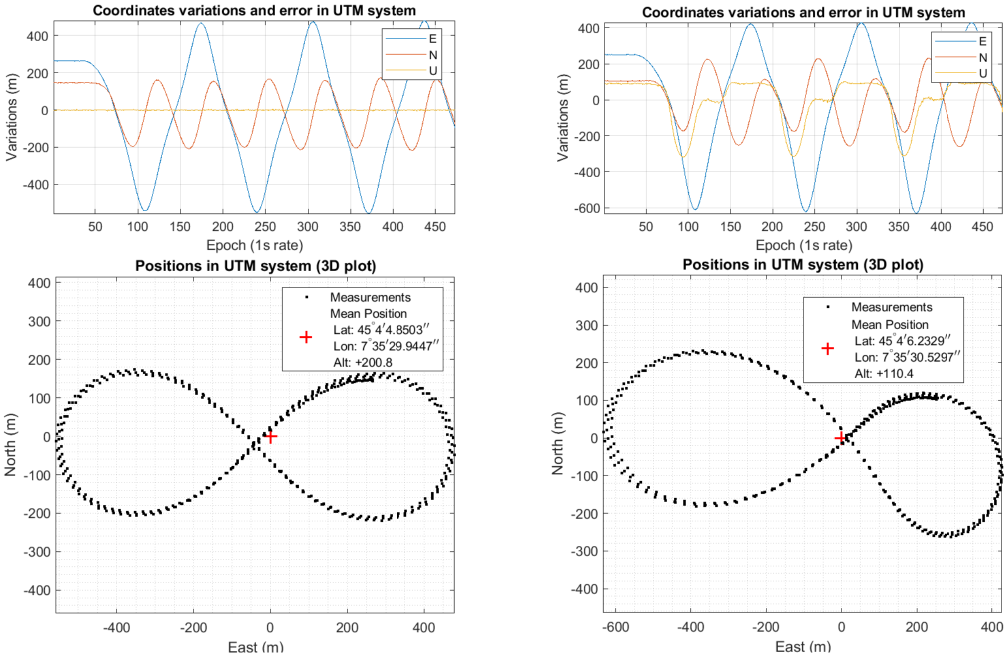

(a) (b)

Figure 6.24: Nominal cooperative PVT estimation 6.24a and the distortion effect of a *promiscuous cyber-attack* performed by inducing the overwriting the measurements of a generic aiding agent A, 6.24b

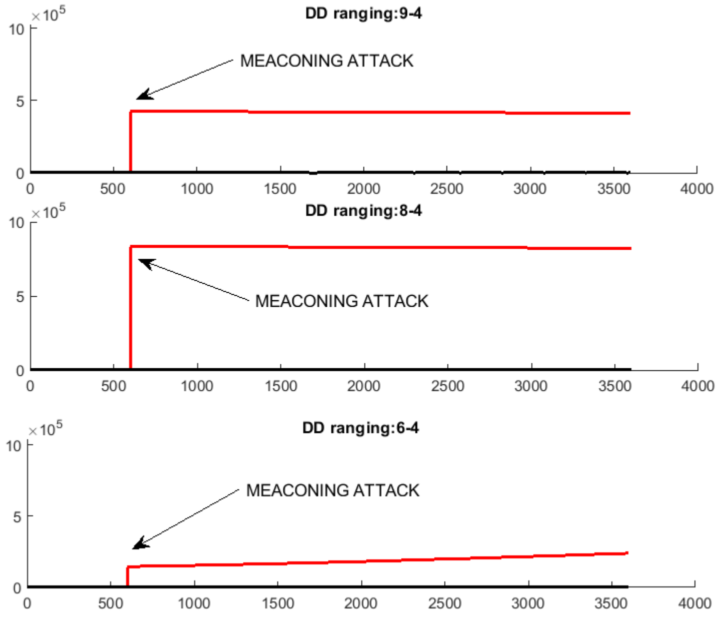

Figure 6.25: Meaconing detection By raw measurements

level, Therefore, there is no control on earlier signal processing stages. $\mathcal{N}$ is the set of cardinality N including the satellites being simulated by the IFEN NavX RFCS to be acquired, tracked and exploited for the PVT of all the receivers. $\mathcal{S}$ is instead the set of cardinality S including faked measurements provided by the agent **S** to replace the measurements of agent **A**.

The test was conducted according to the following steps:

- A set of receivers locally retrieves a set of $N = 10$ pseudoranges and Doppler independently, in nominal conditions.
- Receiver **A** got $N - S$ nominal pseudorange and Doppler measurements and S “spoofed” measurements (injected by an agent which is moving hundred meter ahead on the same path).
- A set of receivers **T** uses the full measurements set provided by **A** to build inter-agent distances via WLS-DD.

Three different combinations of possible attacks can be identified according to the cardinality of the satellite sets:

- a) $S \subseteq N$, and only agent **A** is under attack. All the other agents interacting with **A** are expected to be indirectly affected.

- b) $S \subset N$ and also measurements of receivers **A** are spoofed such that $S_A \cup S_B = S_A$.
- c) $S \subset N$ and also measurements of receivers **T** are spoofed $S_A \cap S_B = \emptyset$ (different subsets of satellites).

In the case a, the attack is performed against a single receiver, while in b and c, the attack aims at damaging the whole cooperative network by acting on "cooperating pairs". A full-set attack (all the visible satellites are actually spoofed) was covered in the previous section.

The aforemention list is provided for the sake of completeness and the following results are referred to the preliminary investigation of mode a. Considering a scenario including kinematic car platooning composed of 9 vehicles moving on a round trajectory, a discontinuity in the range measurement is shown for all the agents collaborating with agent **A**. In Figure 6.25 a relevant discontinuity in the computation of the inter-agent distance via DD is shown under a spoofing attack starting after a given amount of epochs using $S = 7$ such that the amount of visible satellites is high enough to find a non-empty set of common satellites to solve for DD). In this case, spoofing lasts up to the end of the simulation. Such a discontinuity is quite easy to be detected through any threshold-based edge-detection algorithms [108]. The identification of the most effective technique to identify the discontinuity is out of the scope of this paper and it will be addressed in future contributions. A further test was performed by limiting the meaconing attack to 400 epochs, by approaching an ON/OFF attack to check whether anomalies in the measurements can be properly detected through differential measurements. In Figure 6.26b and Figure 6.26a two independent examples are provided. In the first case, agent 4 (agent **A**) was meaconed by agent 5 (through the transmission of its own GNSS measurements) and this induced a sever discontinuity in the range measurements computed by agent 6 (agent **T**). Similarly the computation of the inter-agent distance is altered in the pair 4-9. All the agents collaborating with agent 4 showed similar discontinuity.

These findings provide an indirect strategy to detect measurement anomalies in a network of cooperating agents. Collaborating agents can rise alarms in the network to identify possible outliers due to malicious attacks. Potentials countermeasures to such a kind of cyber-attacks are strategical to make CP frameworks more reliable and robust.

A set of further points must be considered as guidelines for future works:

- The observed behaviour in the DGNSS-CP framework is not related to a an actual RF spoofing, it discloses indeed potential weaknesses to the cooperative frameworks relying on the exchange of raw GNSS measurements.

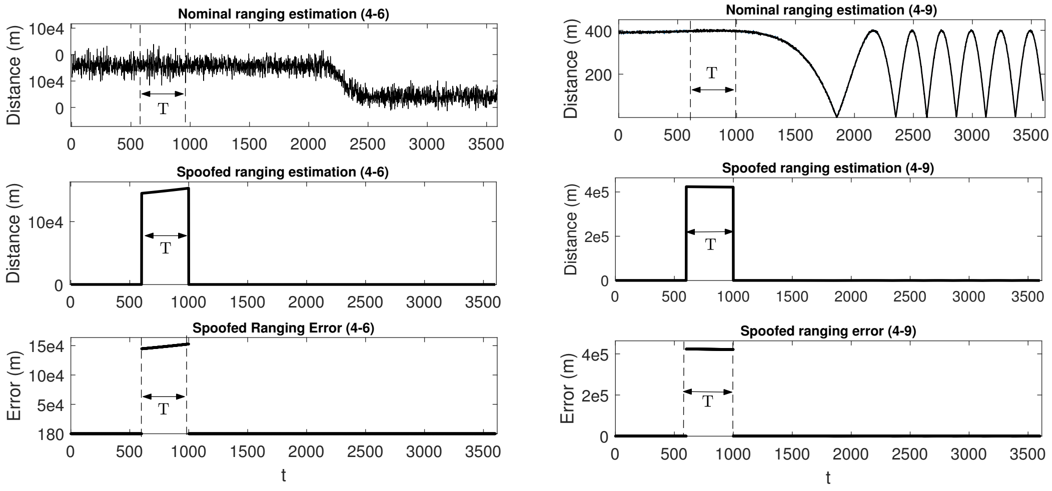

(a) (b)

Figure 6.26: Time-limited meaconing attack to a cooperative network: effects of measurements inconsistency on the differential ranging. The upper plots show the behaviour expected in nominal conditions.

- The measure of the divergency in the nominal and affected positioning solutions must be provided to properly rise a potential flag when dangerous values are observed.

- A check of the consistency of the measurements and reference position of the aiding agent, agent A has to perform a PVT using the retrieved measurements when attack detection is implemented at PVT level. Alternatively, a strategy can be performed at measurements level at which the PVT of the aiding agent is not necessary.

Chapter 7

Conclusions

The thesis deals with analysis of COTS GNSS chipsets and developing algorithms to implement in service robotics, specifically unmanned arial and ground vehicle scenarios. Focus has also been made into defense mechanisms to RF interference threats in such chipsets.

Chapter 3 gives an overview of the fundamentals of GNSS technology and defines the design of GNSS signals, receivers and raw measurements which enable positioning solutions. A discussion on the performances of different grade GNSS receivers follows and the positioning performances of high-end GNSS receivers is seen to set the benchmark for COTS GNSS chipsets.

Chapter 2.2 introduces service robotics and outlines its importance to the modern world. With focus on outdoor unmanned vehicles, the navigational technologies widely used are explained. The current challenges to robust and low cost GNSS based navigation in UAVs and UGVs are explained thereafter. The approach taken in the thesis towards collaborative positioning solutions and the use of Android smartphones to represent COTS GNSS receivers is justified.

The analysis of Android GNSS raw measurements under a completely controlled environment has been documented in Chapter 4. Based on its comparison to real environment-based peer research, the high stability of the C/N_0 in Android devices and significantly reduced pseudorange noises display the vital need for solving the propagation nuisances troubling Android measurements. Comparisons of position measurements between anechoic chamber and a real environment reveal the nuances behind the large errors seen in GNSS only Android positioning solutions, such as the duty cycle occurrence. It is noted that understanding and mitigating them is vital towards the push to achieve higher performance through such devices. The low quality of the GNSS hardware on commercial Android devices also factor in these errors. The limitation of the record and replay paradigm with one transmitting antenna is seen along with the unsuitability of the Google Toolbox PVT algorithm in such a scenario.

Chapter 5 details the different collaborative GNSS approaches applicable to a service robotics scenario with low cost GNSS receivers and the results are seen. In Section 5.1, analysis of displacements and deformation phenomena through the single difference, time differenced approach shows promise through observation of the relative velocities of the two low cost master-rover GNSS receivers. 100% of induced deflections were identified and the false alarm rates were brought down to close to a basic Geodetic GNSS master-rover receiver setup. Section 5.2 demonstrated the successful data exchange of raw GNSS measurements through the IEEE802.11b Wi-Fi connection in Android smartphones. The superior performance of such raw GNSS measurements for relative ranging when compared to stand alone positioning based solutions has been validated. This not only provides a platform for localised exchange of data between Android smartphones, but also a useful computationally efficient ranging methodology in a network of smartphones. The methodology can be transferrable to connected unmanned vehicles with GNSS based autopilots. Section 5.3 confirmed that the paradigm can be exploited to collaboratively improve the accuracy in the position estimation of the UGV but the DGNSS solution requires further optimization to be properly effective in open-sky context. The findings motivate the use of low-cost hardware and software implemented in smartphones, thus reducing the overall cost of the next generation of service robots.

Chapter 6 looks at the interference threats to GNSS in service robotics. The effects of anthropogenic disturbances on the GNSS units integrated in a high end commercial and a low cost customized drone is seen in Section 6.1. The resistance of the drones towards jamming disturbance is found to be is different, where the commercial drone show much better positioning performance compared to the low cost one due to the presence of higher quality IMU unit. However, although the two drones have different resistance to simplistic spoofing, they are successfully spoofed by the HackRF One platform. Analysis on the performance of modern commercial smartphones under simplistic spoofing is done in Section 6.2 and it is seen that the spoofing attack is not fully successful in open-sky conditions. Spoofer transmitted satellites though acquired, are not used by the smartphone GNSS receivers except in the case of overlapping satellites where they are not present in the set of already acquired signals. The spoofer acted more as an interference agent to the smartphones in the L1 band and their GNSS receiver clocks are not affected by it. In Section 6.3, possible approaches of an attack to the proposed cooperative framework presented in this thesis are laid down and the anomalies to be considered to detect an attack in a network of cooperating devices are presented.

7.1 Scope of Future Activities

Future activities should include implementing the GNSS collaborative algorithms proposed in the thesis in the autopilot of UAVs and UGVs. Building effective defense and mitigation algorithms based on the findings of the thesis also carry importance.

Bibliography

[1] Paul Lee et al. *Technology Media and Telecommunications Predictions 2020*. 2020. URL: https://www2.deloitte.com/content/dam/Deloitte/at/Documents/technology-media-telecommunications/at-tmt-predictions-2020.pdf.

[2] Loup Ventures. *Industrial: Robotics Outlook 2025*. 2017. URL: https://loupfunds.com/industrial-robotics-outlook-2025/.

[3] James Manyika et al. “A future that works AI, automation, employment, and productivity”. In: *McKinsey Global Institute Research, Tech. Rep* 60 (2017), pp. 1–135.

[4] Grand View Research. *Precision Farming Market Size Worth 16.35 Billion US Dollars By 2028*. 2021. URL: https://www.tmcnet.com/usubmit/2021/04/22/9351979.htm/.

[5] Josse De Baerdemaeker. “Precision agriculture technology and robotics for good agricultural practices”. In: *IFAC proceedings volumes* 46.4 (2013), pp. 1–4.

[6] Francisco Rovira-Más, Ishani Chatterjee, and Verónica Sáiz-Rubio. “The role of GNSS in the navigation strategies of cost-effective agricultural robots”. In: *Computers and electronics in Agriculture* 112 (2015), pp. 172–183.

[7] International Organization for Standardization. *ISO 12188-1:2010*. 2010. URL: https://www.iso.org/standard/51271.html.

[8] Andres Milioto, Philipp Lottes, and Cyrill Stachniss. “Real-time semantic segmentation of crop and weed for precision agriculture robots leveraging background knowledge in CNNs”. In: *2018 IEEE international conference on robotics and automation (ICRA)*. IEEE. 2018, pp. 2229–2235.

[9] S. Von Bueren and I. Yule. “Multispectral aerial imaging of pasture quality and biomass using unmanned aerial vehicles (UAV)”. In: *Accurate and Efficient Use of Nutrients on Farms, Occasional Report* 26 (2013), pp. 1–5.

[10] C. Zhang and J.M. Kovacs. “The application of small unmanned aerial systems for precision agriculture: a review”. In: *Precision agriculture* 13.6 (2012), pp. 693–712.

[11] P. Biber et al. “Navigation system of the autonomous agricultural robot Bonirob”. In: *Workshop on Agricultural Robotics: Enabling Safe, Efficient, and Affordable Robots for Food Production (Collocated with IROS 2012), Vilamoura, Portugal.* 2012.

[12] P. Pradeep, S.G. Park, and P.Wei. “Trajectory optimization of multirotor agricultural uavs”. In: *2018 IEEE Aerospace Conference.* IEEE. 2018, pp. 1–7.

[13] P. D’Antonio et al. “Satellite guidance systems in agriculture: experimental comparison between EZ-Steer/RTK and AUTOPILOT/EGNOS”. In: *Journal of Agricultural Engineering* (2013).

[14] J.C. del Rey et al. “Comparison of Positional Accuracy betweenRTK and RTX GNSS Based on the Autonomous Agricultural Vehicles under Field Conditions”. In: *Applied Engineering in Agriculture* 30.3 (2014), pp. 361–366.

[15] B.J. Yoon, J.H. Na, and J.H. Kim. “Navigation method using multi-sensor for UGV (Unmanned Ground Vehicle)”. In: *2007 International Conference on Control, Automation and Systems.* IEEE. 2007, pp. 853–856.

[16] M.M. Kurdi et al. “Proposed system of artificial Neural Network for positioning and navigation of UAV-UGV”. In: *2018 Electric Electronics, Computer Science, Biomedical Engineerings’ Meeting (EBBT).* IEEE. 2018, pp. 1–6.

[17] A. Saleem et al. “An integration framework for UGV outdoor navigation system based on LiDAR and vision data”. In: *2015 16th International Conference on Research and Education in Mechatronics (REM).* IEEE. 2015, pp. 16–21.

[18] M.L. Cherif, J. Leclère, et al. “Loosely coupled GPS/INS integration with snap to road for low-cost land vehicle navigation: EKF-STR for low-cost applications”. In: *2018 IEEE/ION Position, Location and Navigation Symposium (PLANS).* IEEE. 2018, pp. 275–282.

[19] B.W. Remondi. “Using the global positioning system(GPS) phase observable for relative geodesy: Modeling, processing, and results[Ph. D. Thesis]”. In: (1984).

[20] J. Tabarracci and P. Currier. “A blueprint for a fixed-wing autopilot on an android smartphone”. In: *2013 Proceedings of IEEE Southeastcon.* IEEE. 2013, pp. 1–6.

[21] P. Bryant, G. Gradwell, and D. Claveau. “Autonomous UAS controlled by onboard smartphone”. In: *2015 International Conference on Unmanned Aircraft Systems (ICUAS).* IEEE. 2015, pp. 451–454.

[22] G.N. Solidakis et al. “An Arduino-based subsystem for controlling UAVs through GSM”. In: *2017 6th International Conference on Modern Circuits and Systems Technologies (MOCAST)*. IEEE. 2017, pp. 1–4.

[23] L. Zhu et al. “Research of remote measurement and control technology of UAV based on mobile communication networks”. In: *2015 IEEE International Conference on Information and Automation*. IEEE. 2015, pp. 2517–2522.

[24] A. AbdElHamid and P. Zong. “Development of UAV teleoperation virtual environment based-on GSM networks and real weather effects”. In: *International Journal of Aeronautical and Space Sciences* 16.3 (2015), pp. 463–474.

[25] L. Aldrovandi et al. “A smartphone based quadrotor: Attitude and position estimation”. In: *2015 International Conference on Unmanned Aircraft Systems (ICUAS)*. IEEE. 2015, pp. 1251–1259.

[26] S. I. Roumeliotis and G. A. Bekey. “Distributed multirobot localization”. In: *IEEE Transactions on Robotics and Automation* 18.5 (Oct. 2002), pp. 781–795. ISSN: 1042-296X. DOI: 10.1109/TRA.2002.803461.

[27] A. I. Mourikis and S. I. Roumeliotis. “Performance analysis of multirobot Cooperative localization”. In: *IEEE Transactions on Robotics* 22.4 (Aug. 2006), pp. 666–681. ISSN: 1552-3098. DOI: 10.1109/TRO.2006.878957.

[28] GPS Directorate Systems Engineering and Integration. *IS-GPS-705D Navstar GPS Space Segment/User Segment L5 Interfaces Document*. Sept. 2013. URL: https://www.gps.gov/technical/icwg/IS-GPS-705D.pdf.

[29] European Space Agency (ESA). *Galileo open service, Signal-In-Space Interface Control Document (OS SIS ICD)*. 2008.

[30] Coordination Scientific Information Center. *Global Navigation Satellite System GLONASS Interface Control Document (ICD)*. 2002.

[31] Jon M Anderson et al. “Chips-message robust authentication (Chimera) for GPS civilian signals”. In: *Proceedings of the 30th International Technical Meeting of The Satellite Division of the Institute of Navigation (ION GNSS+ 2017)*. 2017, pp. 2388–2416.

[32] I Fernandez-Hernandez, G Vecchione, and F Dıaz-Pulido. “Galileo authentication: a programme and policy perspective”. In: *69th International Astronautical Congress*. 2018.

[33] Alan Cameron. “AFRL tests Chimera to battle spoofers and hackers”. In: *GPS World Website* (2019).

[34] Neil Gogoi et al. "Fast Deformation Detection with mass market GNSS time differential observations and use of baseline constraints". In: *GEAM-GEOINGEGNERIA AMBIENTALE E MINERARIA-GEAM-GEOENGINEERING ENVIRONMENT AND MINING* 153 (2018), pp. 32–39.

[35] Ambrogio Maria Manzino, Paolo Dabove, and Neil Gogoi. "Assessment of positioning performances in Italy from GPS, BDS and GLONASS constellations". In: *Geodesy and Geodynamics* 9.6 (2018), pp. 439–448.

[36] Neil Gogoi et al. "A Controlled-Environment Quality Assessment of Android GNSS Raw Measurements". In: *Electronics* 8.1 (Dec. 2018), p. 5. ISSN: 2079-9292. DOI: 10.3390/electronics8010005. URL: http://dx.doi.org/10.3390/electronics8010005.

[37] Neil Gogoi, Alex Minetto, and Fabio Dovis. "A Proof-of-concept of Cooperative DGNSS for UAV/UGV Navigation". In: *Proceedings of the 33rd International Technical Meeting of the Satellite Division of The Institute of Navigation (ION GNSS+ 2020)*. 2020, pp. 2229–2236.

[38] Neil Gogoi, Alex Minetto, and Fabio Dovis. "On the Cooperative Ranging between Android Smartphones Sharing Raw GNSS Measurements". In: *2019 IEEE 90th Vehicular Technology Conference (VTC2019-Fall)* (Sept. 2019), pp. 1–5. DOI: 10.1109/VTCFall.2019.8891320.

[39] Akmal Rustamov et al. "GNSS Anti-Spoofing Defense Based on Cooperative Positioning". In: *Proceedings of the 33rd International Technical Meeting of the Satellite Division of The Institute of Navigation (ION GNSS+ 2020)*. 2020, pp. 3326–3337.

[40] Akmal Rustamov et al. "Assessment of the Vulnerability to Spoofing Attacks of GNSS Receivers Integrated in Consumer Devices". In: *2020 International Conference on Localization and GNSS (ICL-GNSS)*. IEEE. 2020, pp. 1–6.

[41] Michael Decker, Martin Fischer, and Ingrid Ott. "Service Robotics and Human Labor: A first technology assessment of substitution and cooperation". In: *Robotics and Autonomous Systems* 87 (2017), pp. 348–354.

[42] Peter Singer. "Wired for War: The Robotics Revolution and Conflict in the 21st Century". In: 2009.

[43] Pieter Simoens, Mauro Dragone, and Alessandro Saffiotti. "The Internet of Robotic Things: A review of concept, added value and applications". In: *International Journal of Advanced Robotic Systems* 15.1 (2018), p. 1729881418759424.

[44] Ugo Pagallo. "Robots in the cloud with privacy: A new threat to data protection?" In: *Computer Law & Security Review* 29.5 (2013), pp. 501–508.

[45] In Lee. "Service Robots: A Systematic Literature Review". In: *Electronics* 10.21 (2021), p. 2658.

[46] BS Shivaprasad, MN Ravishankara, and BN Shoba. “Design and implementation of seeding and fertilizing agriculture robot”. In: *International Journal of Application or Innovation in Engineering & Management (IJAIEM)* 3.6 (2014), pp. 251–255.

[47] Bing L Luk et al. “Intelligent legged climbing service robot for remote maintenance applications in hazardous environments”. In: *Robotics and Autonomous Systems* 53.2 (2005), pp. 142–152.

[48] Ming-Yuan Shieh, JC Hsieh, and CP Cheng. “Design of an intelligent hospital service robot and its applications”. In: *2004 IEEE International Conference on Systems, Man and Cybernetics (IEEE Cat. No. 04CH37583)*. Vol. 5. IEEE. 2004, pp. 4377–4382.

[49] K-U Scholl et al. “An articulated service robot for autonomous sewer inspection tasks”. In: *Proceedings 1999 IEEE/RSJ International Conference on Intelligent Robots and Systems. Human and Environment Friendly Robots with High Intelligence and Emotional Quotients (Cat. No. 99CH36289)*. Vol. 2. IEEE. 1999, pp. 1075–1080.

[50] Roberto Pinillos et al. “Long-term assessment of a service robot in a hotel environment”. In: *Robotics and Autonomous Systems* 79 (2016), pp. 40–57.

[51] Rudolph Triebel et al. “Spencer: A socially aware service robot for passenger guidance and help in busy airports”. In: *Field and service robotics*. Springer. 2016, pp. 607–622.

[52] Guri B Verne. “Adapting to a Robot: Adapting Gardening and the Garden to fit a Robot Lawn Mower”. In: *Companion of the 2020 ACM/IEEE International Conference on Human-Robot Interaction*. 2020, pp. 34–42.

[53] Julia Fink et al. “Living with a vacuum cleaning robot”. In: *International Journal of Social Robotics* 5.3 (2013), pp. 389–408.

[54] Norman Hendrich, Hannes Bistry, and Jianwei Zhang. “Architecture and software design for a service robot in an elderly-care scenario”. In: *Engineering* 1.1 (2015), pp. 027–035.

[55] Z Zenn Bien et al. “Intelligent interaction for human-friendly service robot in smart house environment”. In: *International Journal of Computational Intelligence Systems* 1.1 (2008), pp. 77–93.

[56] Juan Angel Gonzalez-Aguirre et al. “Service Robots: Trends and Technology”. In: *Applied Sciences* 11.22 (2021), p. 10702.

[57] Jochen Wirtz et al. “Brave new world: service robots in the frontline”. In: *Journal of Service Management* (2018).

[58] Andres Iborra et al. “Design of service robots”. In: *IEEE Robotics Automation Magazine* 16.1 (2009), pp. 24–33. DOI: 10.1109/MRA.2008.931635.

[59] Ifr. *International Federation of Robotics*. URL: https://ifr.org/service-robots.

[60] Robin Gebbers and Viacheslav I Adamchuk. "Precision agriculture and food security". In: *Science* 327.5967 (2010), pp. 828–831.

[61] Simon Blackmore et al. "New concepts in agricultural automation." In: *R&D Conference" Precision in arable farming: current practice and future potential", Grantham, Lincolnshire, UK, 28th-29th October 2009*. HGCA. 2009, pp. 127–137.

[62] Tom Duckett et al. "Agricultural robotics: the future of robotic agriculture". In: *arXiv preprint arXiv:1806.06762* (2018).

[63] Peng Li et al. "Summary on sensors in agricultural robots". In: *2019 International Conference on Image and Video Processing, and Artificial Intelligence*. Vol. 11321. International Society for Optics and Photonics. 2019, 113212Y.

[64] Avital Bechar and Clement Vigneault. "Agricultural robots for field operations: Concepts and components". In: *Biosystems Engineering* 149 (2016), pp. 94–111.

[65] K Morgan. "A step towards an automatic tractor". In: *Farm mech* 10.13 (1958), pp. 440–441.

[66] S Pattinson, S Tiwari, et al. "GNSS precise point positioning for autonomous robot navigation in greenhouse environment for integrated pest monitoring". In: *12th Annual BaÅ¡ ka GNSS Conference*. 2019.

[67] JN Wilson. "Guidance of agricultural vehicles—a historical perspective". In: *Computers and electronics in agriculture* 25.1-2 (2000), pp. 3–9.

[68] Hossein Mousazadeh. "A technical review on navigation systems of agricultural autonomous off-road vehicles". In: *Journal of Terramechanics* 50.3 (2013), pp. 211–232.

[69] Rainer Keicher and H Seufert. "Automatic guidance for agricultural vehicles in Europe". In: *Computers and electronics in agriculture* 25.1-2 (2000), pp. 169–194.

[70] ShuFeng Han, Yong HE, and Hui Fang. "Recent development in automatic guidance and autonomous vehicle for agriculture: A Review". In: *Journal of Zhejiang University (Agriculture and Life Sciences)* 44.4 (2018), pp. 381–391.

[71] PI Coyne, SJ Casey, and GA Milliken. "Comparison of differentially corrected GPS sources for support of site-specific management in agriculture". In: (2003).

[72] Marco Pini et al. “Experimental testbed and methodology for the assessment of RTK GNSS receivers used in precision agriculture”. In: *IEEE Access* 8 (2020), pp. 14690–14703.

[73] M Kise, Q Zhang, and F Rovira Más. “A stereovision-based crop row detection method for tractor-automated guidance”. In: *Biosystems engineering* 90.4 (2005), pp. 357–367.

[74] Corrado Costa et al. “Stereovision system for estimating tractors and agricultural machines transit area under orchards canopy”. In: *International Journal of Agricultural and Biological Engineering* 12.1 (2019), pp. 1–5.

[75] Shu-Li Sun and Zi-Li Deng. “Multi-sensor optimal information fusion Kalman filter”. In: *Automatica* 40.6 (2004), pp. 1017–1023.

[76] Alex Minetto. “GNSS-only Collaborative Positioning Methods for Networked Receivers”. In: *Ph. D. thesis* (2020).

[77] Stergios I Roumeliotis and George A Bekey. “Distributed multirobot localization”. In: *IEEE transactions on robotics and automation* 18.5 (2002), pp. 781–795.

[78] Anastasios I Mourikis and Stergios I Roumeliotis. “Performance analysis of multirobot cooperative localization”. In: *IEEE Transactions on robotics* 22.4 (2006), pp. 666–681.

[79] Iman Shames et al. “Cooperative self-localization of mobile agents”. In: *IEEE Transactions on Aerospace and Electronic Systems* 47.3 (2011), pp. 1926–1947.

[80] Solmaz S Kia, Stephen Rounds, and Sonia Martinez. “Cooperative localization for mobile agents: A recursive decentralized algorithm based on Kalman-filter decoupling”. In: *IEEE Control Systems Magazine* 36.2 (2016), pp. 86–101.

[81] Seçkin Uluskan, Tansu Filik, and Ömer Nezih Gerek. “Circular Uncertainty method for range-only localization with imprecise sensor positions”. In: *Multidimensional Systems and Signal Processing* 29.4 (2018), pp. 1757–1780.

[82] A. Minetto, A. Nardin, and F. Dovis. “Tight Integration of GNSS Measurements and GNSS-based Collaborative Virtual Ranging”. In: *31st International Technical Meeting of the Satellite Division of The Institute of Navigation (ION GNSS+ 2018)*. Sept. 2018, pp. 2399–2413. DOI: 10.33012/2018.15955.

[83] Alex Minetto, Andrea Nardin, and Fabio Dovis. “GNSS-only collaborative positioning among connected vehicles”. In: *Proceedings of the 1st ACM MobiHoc Workshop on Technologies, mOdels, and Protocols for Cooperative Connected Cars*. 2019, pp. 37–42.

[84] A. Minetto and F. Dovis. “A theoretical framework for collaborative estimation of distances among GNSS users”. In: *2018 IEEE/ION Position, Location and Navigation Symposium (PLANS)*. Apr. 2018, pp. 1492–1501. DOI: 10.1109/PLANS.2018.8373543.

[85] Pratap Misra and Per Enge. “Global Positioning System: signals, measurements and performance second edition”. In: *Massachusetts: Ganga-Jamuna Press* (2006).

[86] Elliott D Kaplan and Christopher Hegarty. *Understanding GPS/GNSS: principles and applications*. Artech House, 2017.

[87] B. Hofmann-Wellenhof, H. Lichtenegger, and J. Collins. *Global Positioning System Theory and Practice*. 1st Ed. Wien, Austria: Springer-Verlag, 1992.

[88] P. D. Groves. *Principles of GNSS, Inertial, and Multisensor Integrated Navigation Systems*. 2nd Ed. 16 Sussex Street London SW1V 4RW, UK: Artech House, 2013.

[89] M. S. Grewal, L. R. Weill, and A. P. Andrews. *Global Positioning Systems, Inertial Navigaion, and Integration*. New York, NY, USA: John Wiley and Sons, Inc., 2001.

[90] A. Ucar. “A Subsampling Delta-sigma Modulator for Global Navigation Satellite Systems”. PhD thesis. London, UK: University of Westminster School of Electronics and Computer Science, Nov. 2010.

[91] B. Eissfeller and J.-H. Won. “Receiver Architecture”. In: *Springer Handbook of Global Navigation Satellite Systems*. Ed. by Peter J. G. Teunissen and O. Montenbruck. Gewerbestrasse 11, 6330 Cham, Switzerland: Springer International Publishing AG, 2017. Chap. 13, pp. 365–400.

[92] Frederic Bastide et al. “Automatic gain control (AGC) as an interference assessment tool”. In: 2003.

[93] J.-H. Won and T. Pany. “Signal Processing”. In: *Springer Handbook of Global Navigation Satellite Systems*. Ed. by Peter J. G. Teunissen and O. Montenbruck. Gewerbestrasse 11, 6330 Cham, Switzerland: Springer International Publishing AG, 2017. Chap. 14, pp. 401–442.

[94] GSA working group. *Using GNSS Raw Measurements on Android Devices*. https://www.gsa.europa.eu/system/files/reports/gnss_raw_measurement_web_0.pdf. 2018.

[95] Yuheng He and Attila Bilgic. “Iterative least squares method for global positioning system”. In: *Advances in Radio Science* 9.C. 5-2 (2011), pp. 203–208.

[96] Frank Van Diggelen and Mohammed Khider. “GNSS Analysis Tools from Google”. In: *Inside GNSS* 13.2 (2018), p. 51.

[97] Xiaohong Zhang et al. “Quality assessment of GNSS observations from an Android N smartphone and positioning performance analysis using time-differenced filtering approach”. In: *GPS Solutions* 22.3 (2018), p. 70.

[98] Boyuan Wang et al. “Pedestrian Dead Reckoning Based on Motion Mode Recognition Using a Smartphone”. In: *Sensors* 18.6 (2018), p. 1811.

[99] Aude Privat, Matthieu Pascaud, and Denis Laurichesse. “Innovative smartphone applications for Precise Point Positioning”. In: *2018 SpaceOps Conference*. 2018, p. 2324.

[100] Eugenio Realini et al. “Precise gnss positioning using smart devices”. In: *Sensors* 17.10 (2017), p. 2434.

[101] S Riley et al. “Positioning with Android GNSS observables”. In: *GPS World* 29.1 (2018), pp. 18–34.

[102] Nicola Linty et al. “Performance analysis of duty-cycle power saving techniques in GNSS mass-market receivers”. In: *Position, Location and Navigation Symposium-PLANS 2014, 2014 IEEE/ION*. IEEE. 2014, pp. 1096–1104.

[103] Todd E Humphreys et al. “On the feasibility of cm-accurate positioning via a smartphone’s antenna and GNSS chip”. In: *Radionavigation Laboratory Conference Proceedings*. 2016.

[104] Paolo Dabove, Vincenzo Di Pietra, and Andrea Maria Lingua. “Positioning Techniques with Smartphone Technology: Performances and Methodologies in Outdoor and Indoor Scenarios”. In: *Smartphones from an Applied Research Perspective*. InTech, 2017.

[105] Calogero Cristodaro, Laura Ruotsalainen, and Fabio Dovis. “Benefits and Limitations of the Record and Replay Approach for GNSS Receiver Performance Assessment in Harsh Scenarios”. In: *Sensors* 18.7 (2018), p. 2189.

[106] Mohammed Khider. URL: https://github.com/google/gps-measurement-tools/releases/tag/2.0.0.1. (accessed: 05.03.2021).

[107] Daniele Borio, Haoqing Li, and Pau Closas. “Huber’s Non-Linearity for GNSS Interference Mitigation”. In: *Sensors* 18.7 (2018), p. 2217.

[108] Nicola Linty et al. “Effects of Phase Scintillation on the GNSS Positioning Error During the September 2017 Storm at Svalbard”. In: *Space Weather* 16.9 (), pp. 1317–1329. DOI: 10.1029/2018SW001940. URL: https://agupubs.onlinelibrary.wiley.com/doi/abs/10.1029/2018SW001940.

[109] M Petovello, L Lo Presti, and M Visintin. “Can you list all the properties of the carrier-smoothing filter”. In: *Inside GNSS* (2015).

[110] D. Yang et al. "A GPS Pseudorange Based Cooperative Vehicular Distance Measurement Technique". In: *2012 IEEE 75th Vehicular Technology Conference (VTC Spring)*. May 2012, pp. 1–5. DOI: 10.1109/VETECS.2012.6240332.

[111] K. Liu et al. "Improving Positioning Accuracy Using GPS Pseudorange Measurements for Cooperative Vehicular Localization". In: *IEEE Transactions on Vehicular Technology* 63.6 (July 2014), pp. 2544–2556. ISSN: 0018-9545. DOI: 10.1109/TVT.2013.2296071.

[112] Marco Pini, Gianluca Falco, and Letizia Lo Presti. "Estimation of Satellite-User Ranges Through GNSS Code Phase Measurements". In: *Global Navigation Satellite Systems: Signal, Theory and Applications* (2012), pp. 107–126.

[113] Google Developers. *GNSSMeasurement*. URL: https://developer.android.com/reference/android/location/GnssMeasurement. (accessed: 05.07.2019).

[114] Fabian de Ponte Müller, Alexander Steingass, and Thomas Strang. "Zero-Baseline Measurements for Relative Positioning in Vehicular Environments". In: *Sixth European Workshop on GNSS Signals and Signal Processing*. 2013.

[115] M. Bahrami and M. Ziebart. "Instantaneous Doppler-aided RTK positioning with single frequency receivers". In: *IEEE/ION Position, Location and Navigation Symposium*. May 2010, pp. 70–78. DOI: 10.1109/PLANS.2010.5507202.

[116] A. Minetto, A. Nardin, and F. Dovis. "GNSS-only Collaborative Positioning Among Connected Vehicles". In: *Proceedings of the 1st ACM MobiHoc Workshop on Technologies, mOdels, and Protocols for Cooperative Connected Cars*. TOP-Cars '19. Catania, Italy: ACM, 2019, pp. 37–42. ISBN: 978-1-4503-6807-0. DOI: 10.1145/3331054.3331552. URL: http://doi.acm.org/10.1145/3331054.3331552.

[117] Neil Gogoi, Alex Minetto, and Fabio Dovis. "On the Cooperative Ranging between Android Smartphones Sharing Raw GNSS Measurements". In: *Proceedings of VTC2019-Fall Honolulu Intelligent Connection and Transportation)*. Sept. 2019.

[118] Alex Minetto and Fabio Dovis. "A theoretical framework for collaborative estimation of distances among GNSS users". In: *2018 IEEE/ION Position, Location and Navigation Symposium (PLANS)*. IEEE. 2018, pp. 1492–1501.

[119] A. Minetto and F. Dovis. "On the Information Carried by Correlated Collaborative Ranging Measurements for Hybrid Positioning". In: *IEEE Transactions on Vehicular Technology* (2019), pp. 1–1. ISSN: 1939-9359. DOI: 10.1109/TVT.2019.2957015.

[120] B. Huang et al. “Dilution of Precision Analysis for GNSS Collaborative Positioning”. In: *IEEE Transactions on Vehicular Technology* 65.5 (May 2016), pp. 3401–3415. ISSN: 0018-9545. DOI: 10.1109/TVT.2015.2436700.

[121] A. Minetto, G. Falco, and F. Dovis. “On the Trade-Off between Computational Complexity and Collaborative GNSS Hybridization”. In: *2019 IEEE 90th Vehicular Technology Conference (VTC2019-Fall)*. Sept. 2019, pp. 1–5. DOI: 10.1109/VTCFall.2019.8891571.

[122] F van Diggelen, R Want, and W Wang. “How to achieve 1-meter accuracy in Android”. In: *Website http://gpswo rld. com/how-to-achie ve-1-meter-accu r acy-in-andro id/[accessed 8 October 2018]* (2018).

[123] Bob Balaram et al. “Mars helicopter technology demonstrator”. In: *2018 AIAA Atmospheric Flight Mechanics Conference*. 2018, p. 0023.

[124] Fabio Dovis. *GNSS interference threats and countermeasures*. Artech House, 2015.

[125] Daniele Borio et al. “Impact and detection of GNSS jammers on consumer grade satellite navigation receivers”. In: *Proceedings of the IEEE* 104.6 (2016), pp. 1233–1245.

[126] Wenjian Qin et al. “A comparison of optimized mitigation techniques for swept-frequency jammers”. In: *Proceedings of the 2019 International Technical Meeting of The Institute of Navigation*. 2019, pp. 233–247.

[127] Daniele Borio, Laura Camoriano, and Letizia Lo Presti. “Two-pole and multi-pole notch filters: a computationally effective solution for GNSS interference detection and mitigation”. In: *IEEE Systems Journal* 2.1 (2008), pp. 38–47.

[128] Luciano Musumeci and Fabio Dovis. “Use of the wavelet transform for interference detection and mitigation in global navigation satellite systems”. In: *International Journal of Navigation and Observation* 2014 (2014).

[129] Esteban Garbin Manfredini, Fabio Dovis, and Beatrice Motella. “Validation of a signal quality monitoring technique over a set of spoofed scenarios”. In: *2014 7th ESA Workshop on Satellite Navigation Technologies and European Workshop on GNSS Signals and Signal Processing (NAVITEC)*. IEEE. 2014, pp. 1–7.

[130] Jan Farlik, Miroslav Kratky, and Josef Casar. “Detectability and jamming of small UAVs by commercially available low-cost means”. In: *2016 International Conference on Communications (COMM)*. IEEE. 2016, pp. 327–330.

[131] Jan Farlik et al. “Multispectral detection of commercial unmanned aerial vehicles”. In: *Sensors* 19.7 (2019), p. 1517.

[132] Lorenz Meier, Dominik Honegger, and Marc Pollefeys. "PX4: A node-based multithreaded open source robotics framework for deeply embedded platforms". In: *2015 IEEE international conference on robotics and automation (ICRA)*. IEEE. 2015, pp. 6235–6240.

[133] G. S. Gadgets. *HackRF One*. URL: https://greatscottgadgets.com/hackrf/one/.

[134] Kexiong Curtis Zeng et al. "A practical GPS location spoofing attack in road navigation scenario". In: *Proceedings of the 18th International Workshop on Mobile Computing Systems and Applications*. 2017, pp. 85–90.

[135] G. Galluzzo, M Navarro-Gallardo, and M Sunkevic. *Using GNSS Raw Measurements on Android Devices-Tutorial part I*. 2017.

[136] Daiqin Yang et al. "A GPS Pseudorange Based Cooperative Vehicular Distance Measurement Technique". In: July 2012. DOI: 10.1109/VETECS.2012.6240332.

[137] Jason Gross and Todd Humphreys. "GNSS Spoofing, Jamming, and Multipath Interference Classification using a Maximum-Likelihood Multi-Tap Multipath Estimator". In: Mar. 2017, pp. 662–670. DOI: 10.33012/2017.14919.

[138] Esteban Manfredini et al. "Effective GPS Spoofing Detection Utilizing Metrics from Commercial Receivers". In: Feb. 2018, pp. 672–689. DOI: 10.33012/2018.15595.

[139] Ali Jafarnia Jahromi, Ali Broumandan, and Geard Lachapelle. "GNSS signal authenticity verification using carrier phase measurements with multiple receivers". In: *2016 8th ESA Workshop on Satellite Navigation Technologies and European Workshop on GNSS Signals and Signal Processing (NAVITEC)*. IEEE. 2016, pp. 1–11.

[140] John David Jackson. *Classical electrodynamics*. 1999.

[141] Andres Milioto, Philipp Lottes, and Cyrill Stachniss. "Real-Time Semantic Segmentation of Crop and Weed for Precision Agriculture Robots Leveraging Background Knowledge in CNNs". In: *2018 IEEE International Conference on Robotics and Automation (ICRA)*. 2018, pp. 2229–2235. DOI: 10.1109/ICRA.2018.8460962.

[142] D. Plets et al. "An assessment of different optimization strategies for location tracking with an Android application on a smartphone". In: *11th European Conference on Antennas and Propagation (EUCAP 2017)*. Mar. 2017, pp. 2096–2100. DOI: 10.23919/EuCAP.2017.7928182.

[143] Justyna Redelkiewicz et al. *Opportunities and practical use of Android GNSS Raw Measurements*. https://mycoordinates.org/opportunities-and-practical-use-of-android-gnss-raw-measurements/. Aug. 2018.

[144] Reza Zekavat and R Michael Buehrer. *Handbook of position location: Theory, practice and advances*. Vol. 27. John Wiley & Sons, 2011.

[145] Axel Küpper. *Location-based services: fundamentals and operation*. John Wiley & Sons, 2005.

[146] F. F. Lastname and T. Author. “The title of the cited contribution”. In: *The Book Title*. Ed. by F. Editor and A. Meditor. City, Country: Publishing House, 2007, pp. 32–58.

[147] Kenneth M Pesyna Jr, Robert W Heath Jr, and Todd E Humphreys. “Centimeter positioning with a smartphone-quality GNSS antenna”. In: *Radionavigation Laboratory Conference Proceedings*. 2014.

[148] Fabio Dovis et al. “A run-time method based on observable data for the quality assessment of gnss positioning solutions”. In: *IEEE Journal on Selected Areas in Communications* 33.11 (2015), pp. 2357–2365.

[149] S Banville and FV Diggelen. “Precise GNSS for everyone: precise positioning using raw GPS measurements from android smartphones”. In: *GPS World* 27.11 (2016), pp. 43–48.

[150] F Tobe. *Views and forecasts about robotics for the ag industry*. 2016.

[151] Ming Li et al. “Review of research on agricultural vehicle autonomous guidance”. In: *International Journal of Agricultural and Biological Engineering* 2.3 (2009), pp. 1–16.

This Ph.D. thesis has been typeset by means of the TEX-system facilities. The typesetting engine was pdfLATEX. The document class was `toptesi`, by Claudio Beccari, with option `tipotesi=scudo`. This class is available in every up-to-date and complete TEX-system installation.